SYNTHESIS, CHARACTERIZATION AND INVESTIGATION OF CYTOTOXIC EFFECTS OF DRUG LOADED ZIF-8 METAL-ORGANIC FRAMEWORKS

A Thesis Submitted to
the Graduate School of Engineering and Sciences of
İzmir Institute of Technology
in Partial Fulfillment of the Requirements for the Degree of

DOCTOR OF PHILOSOPHY

in Chemistry

by
Derya METE

December 2021
İZMİR

ACKNOWLEDGMENTS

Firstly, I would like to First, I would like to express my deep gratitude to my supervisor, Prof. Dr. Gülşah ŞANLI MOHAMED for the opportunity she gave to me, endless support, encourage and patience for helping me to trust myself and to smile all the time. She always motivated me to strive hard, even when I was tempted to give up. All the things that I have learnt from her, and her guidance were invaluable.

I would also like to express my appreciations to my thesis committee, Prof. Dr. Ali ÇAĞIR and Assoc. Dr. Yaşar AKDOĞAN for their kindly help and advice. Besides this, I would also like to thank to my examining committee members, Prof. Dr. Şenay ŞANLIER and Prof. Dr. Kemal Sami KORKMAZ for accepting to evaluate my thesis and their valuable suggestions.

I would like to thank all the staff and facility managers at İYTE MAM and BİYOMER for their help and suggestions.

I am grateful to Egehan YEMEZTAŞLICA YETİŞKİN, the best labmate ever, without her support and help, this thesis would have been very difficult to complete. I want to thank Şanlı Research Group members Sinem ŞAHİNOĞLU, Dorukhan ÖZEN, Nagihan AYDIN and İbrahim Hanif NAZLI for their support. I also want to thank KK Lab Group members

I am grateful to my sister in IYTE, Tuğçe AKBAŞ my biggest chance in life, and C301 family for their good friendship, encouragements, and constructive comments.

My special thanks go to my mother Ayşe BOSTANBAŞ, my father Fikri BOSTANBAŞ, my sister Deniz ŞENTÜRK, my brother Gürkay ŞENTÜRK, and my husband Rasih METE. They provided the greatest support in my education life, who never spared their love and support and always encouraged me. It would not have happened without them.

Finally, I would like to thank my little daughter, Kumsal METE for being my motivation source. I love her more than anything in my life. This thesis is for you baby

This study was supported by the Scientific and Technological Research Council of Turkey (TÜBİTAK, 118Z860, 119Z023)

ABSTRACT

SYNTHESIS, CHARACTERIZATION AND INVESTIGATION OF CYTOTOXIC EFFECTS OF DRUG LOADED ZIF-8 METAL-ORGANIC FRAMEWORKS

The biocompatible ZIF-8 intelligent material, a member of the metal-organic framework family, has a biodegradable property in an acidic environment due to its poor coordination bonds. Because cancerous cells are more acidic than healthy cells, our studies aim to ensure that doxorubicin, sorafenib, and apalutamide, encapsulated in ZIF-8, target cancer cells responsive to pH, thereby reducing damage to healthy cells.

In addition, ZIF-8 was selected not only as a carrier system but also as a therapeutic effect. Because ZIF-8 material is biodegradable, it is divided into zinc and 2-methylimidazole components in cancer cells. Research shows that the decrease in the amount of zinc is essential in the formation of cancer cells. Zinc is reported to be in lower intracellular concentrations in HCC and prostate cell lines instead of healthy variants. It aims to create dual cytotoxic effects on cancer cells by combining the effects of zinc-drug on a single platform.

ÖZET

İLAÇ YÜKLÜ ZIF-8 METAL-ORGANİK ÇERÇEVELERİN SENTEZİ, KARAKTERİZASYONU VE SİTOTOKSİK ETKİLERİNİN İNCELENMESİ

Metal-organik çerçeve ailesinin bir üyesi olan biyouyumlu ZIF-8 akıllı malzemesi, zayıf koordinasyon bağları nedeniyle asidik bir ortamda biyolojik olarak parçalanabilir bir özelliğe sahiptir. Kanserli hücreler sağlıklı hücrelerden daha asidik olduğundan, çalışmalarımız ZIF-8 içinde kapsüllenen doksorubisin, sorafenib ve apalutamidin pH'a duyarlı kanser hücrelerini hedef almasını ve böylece sağlıklı hücrelere verilen zararı azaltmayı amaçlamaktadır.

Ayrıca ZIF-8 sadece taşıyıcı sistem olarak değil aynı zamanda terapötik bir etki olarak da seçilmiştir. ZIF-8 materyali biyolojik olarak parçalanabilir olduğundan kanser hücrelerinde çinko ve 2-metilimidazol bileşenlerine ayrılır. Araştırmalar çinko miktarının azalmasının kanser hücrelerinin oluşumunda önemli olduğunu göstermektedir. Çinkonun, sağlıklı varyantlar yerine HCC ve prostat hücre dizilerinde daha düşük hücre içi konsantrasyonlarda olduğu bildirilmektedir. Çinko-ilaç etkilerini tek bir platformda birleştirerek kanser hücreleri üzerinde ikili sitotoksik etkiler oluşturmayı amaçlamaktadır.

TABLE OF CONTENTS

LIST OF FIGURES

Figure **Page**

Figure **Page**

Figure **Page**

LIST OF TABLES

Table **Page**

CHAPTER 1

INTRODUCTION

1.1. Cancer

Cancer is a complex series of disease conditions to the health of humans that progress step by step to create an area of cells capable of uncontrolled (abnormal) growth and escape from the body's natural cell death mechanism. Therefore, how to overcome it is still a significant challenge worldwide(Pavlova & Thompson, 2016). Repeated exposure to carcinogens such as tobacco smoke, ultraviolet light, persistent tissue damage, and some viral infections, genetic and epigenetic changes lead to the initiation, progression, and metastasis of this disease (McCance & Huether, 2018; Sounni & Noel, 2013; Thanki, Gangwal, Sangamwar, & Jain, 2013). Recent cancer statistics have shown that cancer-related mortality rates have increased significantly, and these rates are estimated to increase by 50% by 2020(Roy & Li, 2016). Statistical data reported by the World Health Organization (WHO) indicate an urgent need for improved cancer effective treatment strategies, including chemotherapy (CT), photodynamic therapy (PDT), and photothermal therapy (PTT) with improved efficacy and reduced side effects(Gai et al., 2018; Phillips et al., 2006). Among these treatments, CT is the most widely used treatment method, mainly based on the drug-delivery systems to prevent cancer cell proliferation, invasion, and metastasis, and finally, kill them(Pavlova & Thompson, 2016). As cancer cells develop from normal cells of the body, it is challenging to treat them selectively with traditional chemotherapeutic agents(Hanahan & Weinberg, 2011).

These agents act through various cellular mechanisms, i.e., by stopping the cell cycle at various stages(Velma, Dasari, & Tchounwou, 2016), inducing apoptosis and preventing the proliferation of cancer cells(Valter et al., 2017), and interfering with metabolic reprogramming of active anticancer drugs. They enable the body to be effective on cancerous cells such as the skin, spleen, liver, and many other organs(Pavlova & Thompson, 2016).

However, anticancer drugs cause toxicity on non-cancerous cells of the body such as the skin, spleen, liver, and many other organs(Thakkar, Sharma, Kalia, & Tekade,

2020). However, traditional drug-delivery systems suffer from non-responsive, non-targeted, and low effective drug release, limiting clinical applications(Senapati, Mahanta, Kumar, & Maiti, 2018). Compared with the normal tissue environment, the tumor microenvironment has noticeable differences, such as the decrease of pH value, the enhancement of hypoxia, the increase of reactive oxygen species, the change of ATP concentration, etc. These innate biological signals or pathological abnormalities are biological triggers that can indicate the occurrence of disease. In turn, it renders them attractive targets when designing a bioresponsive drug-delivery system for cancer(Mo & Gu, 2016). Recently, based on tumor microenvironments such as H_2O_2, glutathione (GSH), pH, and adenosine triphosphate (ATP), the drug delivery nanosystem has been widely developed in cancer therapy(Mo & Gu, 2016). One of the main problems in pharmaceutical and biotechnological fields is the transport of the drug to its effect. Therefore, drug delivery systems have always been the focus of researchers' attention (Vasir, Reddy, & Labhasetwar, 2005). Today, new technologies are used to minimize the problems arising in drug use(Vasir & Labhasetwar, 2005). For this purpose, researchers working in different disciplines are brought together, and the developments obtained are transformed into clinical effectiveness. Thanks to these studies, specific targeted drug delivery systems are developed (CANEFE & DUMAN, 1994).

1.2. Drug Delivery Systems/ Nanocarriers

Targeted drug delivery systems enable drugs to be delivered to the target more effectively and practically than today's drugs. Most of the drugs in use do not show their effects in the hydrophobic areas at the stage of reaching target cells. In addition, it is an undesirable event that the drugs cannot show their effects within the specified time and affect the whole body except the target tissue. Another problem is the active substance cannot reach the target area by crossing the barriers in the body. Nanotechnology offers several methods in solving these problems arising in the use of active ingredients. Thanks to the development of nanocarriers, drugs are delivered to the target tissue by crossing various anatomical and biological structures such as the blood-brain barrier, bronchioles in the respiratory system, and tight junctions in the skin (Wickham, 2003).

The nanocarriers that show the better distribution in narrow areas in the body facilitate the dissolution of low solubility drugs. Nanocarrier systems with new features reduce drug toxicity and provide more efficient drug distribution. Drugs obtained by using natural or synthetic polymers must be immobilized on the surface of the nanocarrier system. Thus, the immune system recognizes the surface properties of the nanocarrier in the body, preventing it from being perceived as a foreign body in the targeted area (Singh & Lillard Jr, 2009). Thanks to all these adjustment processes, the effect of the drug on the diseased area only, the drug's staying in the blood effectively for a long time in a single application, and the release of the drug at a specific rate and insufficient amount. However, the use of nanocarriers in drug release brings some problems with it. For example, nanocarrier systems are challenging to obtain and store. They are not suitable for low potency drug releases. In some applications, they can cause damage bypassing undesirable areas. It can cross the membrane surrounding the cell nucleus, causing genetic damage and mutation. Drug delivery systems have become the most critical research area, thanks to techniques that can selectively deliver drugs to pathological cells, tissues, or organs (Vasir et al., 2005). As a result of the developments achieved in nanotechnological research, nanoparticles, which have many applications in the clinic, have had a significant impact on the pharmaceutical industry. The practical use of nanoparticles in the pharmaceutical industry in applications such as direct binding to the active substance, confinement, and targeting has made nanoparticles a preferred position (Swarbrick, 2013). In addition, studies are carried out to prevent harmful side effects, increase bioavailability and effect rate. As a result of these studies, various active substance release systems and targeting systems have been developed. Nanotechnology develops new methods by addressing the behavior of therapeutic agents in nanocarriers (nanoparticles, nanocapsules, micelles, dendrimers) and spherical structures created artificially by bilayer lipids used in the study of biological membranes (Parveen, Misra, & Sahoo, 2012; L. Zhang et al., 2008). The nanocarriers obtained from the research enable the targeted drugs to be transported to the diseased structure. Thanks to nanoparticle research, it is possible to diagnose and treat many diseases today. In addition, it shows rapid development in health due to its application potential in drug delivery systems. It is more and more involved in drug delivery system technology with each passing day (Tüylek, 2017). The effects of other disciplines on the field of health and nanotechnological applications have accelerated the process of new drugs to replace traditional drugs.

1.3. Metal Organic Frameworks

Especially in the last decade, with the success of the nanoscale production of this type of crystalline material, it has been increasingly used both as a theranostic agent and in platforms such as drug delivery systems. The primary benefit of studying this type of material at the nanoscale was the observation that the accumulation of these nanoparticles in tumor tissue increased, increasing the improved permeability and retention effect of their metal-organic skeletons (Fang, Nakamura, & Maeda, 2011). These systems emerge from the release of bioactive agents in a chemical reaction at a certain speed to be specific to a certain structure (CANEFE & DUMAN, 1994). Metal-Organic Frameworks (MOFs) offer multiple versatilities for the accommodation of active ingredients (AIs): flexible structure based on organic ligands and inorganic clusters as building units (BUs), that can be AIs themselves; accessible porosity and large surface areas; availability of functionalization sites; and biodegradability, among others. It is essential that MOFs selected as platforms are biocompatible and do not exhibit toxicity.

1.3.1. History of MOF

Porous coordination polymers present a new class of compounds called metal-organic frameworks, which are more specific than coordination polymers for 2D or 3D crystalline networks with porous structures (Arora et al., 2019). Because of this reason, they have adjustable physical and chemical properties. Although MOFs face several challenges such as cost and stability, before finding industrial applications in fundamental materials science, they have become a dominant subject compared to other well-known porous materials such as activated carbons, silica, or zeolites (Bieniek et al., 2021). Many scientists worked on the discovery of MOFs, and different structures were discovered in separate years. In addition, the term "metal-organic framework" first appeared in the 1995 publication of Yaghi and Li. This publication was related to two materials: (Cu-4, 4-'bpy) 1.5 ·NO3 (H2O)1.25 network (Bieniek et al., 2021; Kondo et al., 2009; A. M. Schejn, 2015).

Moreover, the story of these two materials in the early 1960s began with coordination polymer chemistry, and many years later, many studies have been done, and

different structures have been found. The year 1999 was a turning point because, in 1999, Williams and colleagues reported the metal-organic framework HKUST-1, and the Yaghi group brought up the structure and properties of the MOF-5(Chui, Lo, Charmant, Orpen, & Williams, 1999; H. Li, Eddaoudi, O'Keeffe, & Yaghi, 1999). After that, Férey and Coworkers discovered Materials of Institute Lavoisier (MILs) nearly starting from 2002. These materials are MIL-53(Cr), MIL-53(Al) (Serre et al., 2002). Férey's work with MIL-101 was also an important point. Working with this material showed that the crystal structure can be predicted by targeted chemistry and global optimization simulations. In 2006, Yaghi introduced several different zinc imidazolate-based networks to obtain MOFs that are chemically stable (Park, Ni, Côté, Choi, Huang, Uribe-Romo, Chae, O'Keeffe, et al., 2006). These networks included mixtures: ZIF-1,4,6,8,10,11 with zinc; ZIF-9,12 with cobalt; and ZIF-5 with a mixture of zinc and indium. As a result of the study, the following two observations were made: The structure of ZIF-8 did not change in methanol, water, benzene for seven days, and likewise, after boiling ZIF-8 in sodium hydroxide concentrated solution for 24 hours. UiO-66 was added to the MOF list in 2008 after being identified by the Lillerud group at the University of Oslo (Cavka et al., 2008). NOTT, series 100-103, is also known as tetra carboxylate ligands. Schroder and his collaborators at the University of Nottingham synthesized and analyzed NOTT (Lin et al., 2009). In 2010, the Bio-MOF-11 synthesized solvothermal for improved selective carbon dioxide capture by Rosi and coworkers (T. Li et al., 2013). In 2011 the first MOF, CAU-5, with photo-exchangeable binders that can switch from trans to cis isomer by UV irradiation, was developed by the Stock's group from the Christian Albrechts University Kiel (Modrow, Zargarani, Herges, & Stock, 2011).

Previous work for MOFs mainly included transition metal-based materials. The leading group of metal-based networks is studied less. Materials consisting of Li or Mg porous coordination polymers have gained more importance because they can provide enhanced gas adsorption. The MOF-74 containing Mg was discovered by Caskey and Matzger in 2008 and was later approved in the studies of Yaghi and coworkers (Caskey, Wong-Foy, & Matzger, 2008). Apart from these, many articles have reviewed the properties and the future potential of MOFs in the last 20 years (Kuppler et al., 2009). Most notably, progress on MOFs was covered extensively in the second themed issue of Chemical Society Reviews (RSC) in 2014, after earlier mentions in Chemical Reviews (ACS) in 2009 and 2012 (H.-C. J. Zhou & Kitagawa, 2014). Numerous studies and reports have reported the feasibility of using MOFs in real-world applications.

Nonetheless, only a few efforts have been made to evaluate and/or overcome the barriers that currently face the further development of MOFs. In January 2016, Coordination Chemistry Reviews (Elsevier) published a special issue entitled 'Chemistry and applications of MOFs,' which dealt with a broad range of MOF-related subjects. That review discussed the diversity of MOF chemistry and some of the newly emerging areas in MOF-based composites; all of these subjects are important for the continued growth of this promising field and the realization of their full potential in real-world applications (Furukawa, Cordova, O'Keeffe, & Yaghi, 2013). Nevertheless, MOF research's key challenges must be addressed before these materials can be widely used in real-world applications. As of 2016, 75,600 MOF structures (almost 9% of all compounds) were submitted to the Cambridge Structural Database (CSD). Each material discovered and developed has contributed to many conveniences and developments for the future and today(A. M. Schejn, 2015).

1.3.2. Structure of MOFs

Metal-organic skeletons (MOFs) are crystalline, porous, high-volume materials formed by the self-polymerization of metal ions (or metal clusters) and organic multi-toothed ligands. The structure of MOFs results from the coordination and self-assembly of metal cations and organic ligands/linkers. Several bonding types can be observed in a MOF crystal: electrostatic interactions, hydrogen bonding, metal coordination, and pi-pi stacking (Carné, Carbonell, Imaz, & Maspoch, 2011).

In other words, MOFs are nodes formed by inorganic units called PBU (Primary Building Unit) linked with organic polydentate ligands; or one (1D), two (2D), or three-dimensional (3D) structures containing clusters of metal cations called SBU (Secondary Built Unit) (D. Banerjee, Wang, Deibert, & Li, 2016; Y. Cheng et al., 2009). Transition metals such as Zn, Cu, Fe, Cr, Co, Ni, V, Sc, Y are the most commonly used elements in nodes, but also alkaline earth metals (e.g., Mg, Ca, Sr, Ba, Ra), the main groups of the primary periodic table metals (e.g., Sn or Al) and/or rare earth metals (such as Lanthanides) have been used(Florczak, Janiszewska, Kędzierska, & Kowalak, 2011; Vagin, Ott, & Rieger, 2007). Metal ions play an essential role in controlling the properties, pores, and structures of MOFs. The selection of different metal ions can regulate the

assembly process, and different coordination geometries of metal ions can result in different network topology structures. The commonly reported metal ions in MOFs are transition metal ions, such as Zn^{2+}, Cu^{2+}, Ni^{2+}, Co^{2+}, Cr^{3+}, Fe^{3+}, Ag^{+}, and Zr^{4+}. The transition metals are elements that have partially filled shells of d-electrons and f-electrons in some of their compounds. Organic ligand (also called linker) is another essential building block of a MOF structure. O- (e.g., phosphonates, carboxylates, sulfonates) or N-donors (e.g., pyrazines, pyridines, imidazoles, terephthalates) are the most commonly used classes of binders (Horcajada et al., 2007; A. M. Schejn, 2015). Organic ligands, also known as organic linkers, play a decisive role in the synthesis of MOFs. Considerable diversity of organic ligands has been used for creating MOFs. Different ligands influence the topology structure of MOFs and control the distance of metal ions and the dimension of crystal structures (Tranchemontagne, Hunt, & Yaghi, 2008). However, it remains challenging to find methods to tune the structural characters of MOFs well. Organic ligands should contain two or more multidentate functional groups, for example, COOH, CS_2H, NO_2, SO_3H, and PO_3H. Carboxylate ligands are the most common ligands in MOFs due to their vital coordination function and various coordination patterns (Hu et al., 2012). The linker-based tunability of the structure allows researchers to achieve the desired MOF properties, such as high surface area, meso/microporosity, and proper functionalization (Howarth et al., 2017).

At present, this is accompanied by significant developments in synthesis methods using aqueous and non-aqueous media, including solvo / hydrothermal, microwave, ultrasound, electro, and mechanochemical methods (Dey, Kundu, Biswal, Mallick, & Banerjee, 2014). Relationships between these synthesis approaches and the essential properties of MOFs have been assessed comprehensively in several recent research papers (F. Chen et al., 2021). Careful consideration must be taken when choosing the synthetic method because this can affect the shape, size, phase formation, and many other properties of the resulting MOF. Many synthetic routes were initially developed following conventional hydrothermal, solvothermal, and slow diffusion methods using typical processing conditions (taking several hours to several days). For these conventional methods, heating was also required (e.g., electric heating, sand baths, oil baths, or heating jackets) (Qiuxiang Wang, Sun, Li, Zhang, & Yao, 2020; Y. Zhao et al., 2016). Recently, some alternative approaches (e.g., microwave (MW)-assisted hydrothermal, ultrasound (US) irradiation synthesis, sonocrystallization, mechanosynthesis, micro precipitation, co-precipitation methods, stirring, and solventless

high-pressure synthesis) have been introduced, providing several advantages (e.g., more facile preparation, fast kinetics, high phase purity, high yield, low cost, and commercially-viable routes toward the production of MOFs) (Dey et al., 2014; Kreno et al., 2012; Mueller et al., 2006). MW and US irradiation methods are the most attractive options due to their short crystallization time and low reaction temperature.

Proper control of MOF synthesis is expected to lead to the development of more stable, functional, and structurally sophisticated materials (Y. Cheng et al., 2009; Furukawa et al., 2013). MOFs are already challenging most of our perceptions of what is possible in the world of crystalline porous materials. For example, ultra-high surface areas (in the range of 1000-10,000 m2 / g), very low density (in the range of 0.13-1.5 g/cm3), large It has unique properties such as porosity (more than 50%), pore sizes in a wide 3--100 Å range, good thermal (up to 300-500°C), and chemical stability (Furukawa et al., 2013; Kreno et al., 2012; Morozan & Jaouen, 2012; Mueller et al., 2006). In addition to its large volume and surface area, it has become an exciting platform for drug release applications in recent years due to the detailed knowledge of its pores and cavities (M. X. Wu & Yang, 2017).

MOFs' exciting and unique feature is their ability to undergo reversible structural transformations in response to external stimuli such as temperature, pressure, and adsorption. At the same time, some remain in a crystalline state (D. Li & Kaneko, 2001; Morozan & Jaouen, 2012; Sarkisov, Martin, Haranczyk, & Smit, 2014).

However, the most crucial feature of MOFs is their modular structure. Using the simple variation of building blocks, many different structures can be constructed following the same topology. This means that new materials can be accurately designed to have specific properties (such as porosity, dimensions of channels, and surface chemistry) and functions (Dey et al., 2014; Kreno et al., 2012; Mueller et al., 2006). Moreover, the post-synthetic modification of MOFs offers additional avenues for the development of new structures that add additional functions and properties (Kreno et al., 2012). It is estimated that about 6000 new structures are reported each year (Bennett & Cheetham, 2014; Huxford, Della Rocca, & Lin, 2010).

This high level of "designability" of materials is genuinely unprecedented in the world of porous materials and opens a unique path towards multifunctional, bespoke materials for special applications (Dey et al., 2014; Kreno et al., 2012; Mueller et al., 2006).

Naturally, MOFs' unique properties are noted in the chemical community and for chemical engineering applications in materials engineering, nanotechnology, physics, energy, biology, medicine, and environmental engineering (Ryder & Tan, 2014).

Although MOFs are used as energy material applications (batteries, supercapacitors, and fuel cells), gas storage, catalysts, optronic and luminescent materials, porous magnets, sensors, and biomedical materials (drug delivery systems, diagnostic tests, imaging), the most important (scale and in terms of impact) potential industrial application is gas adsorption (mainly N_2, CO_2, H_2, CH_4) and separation (Kanoh et al., 2009; Kondo et al., 2009; Kondo et al., 2011; Kreno et al., 2012; Kuppler et al., 2009; Morozan & Jaouen, 2012). For large-scale applications, the cost and robustness of a MOF is predominant factor. However, for applications such as detection and drug delivery, this is not important and can significantly overcome the shortcomings when considering the benefits of MOFs (Bieniek et al., 2021).

The biomedical potential of MOF materials is predominantly due to their high porosity, ability to adsorb and host biologically active compounds, and the wide-ranging functionalization methods available. Among the available MOFs, several classes of MOF have been identified, which are non-toxic, biocompatible, and can have an interesting bespoke pH response (L.-L. Tan et al., 2015). MOF materials are used in biomedical applications as drug delivery systems, contrast agents, and/or therapeutic agents and sensors (Tamames-Tabar, García-Márquez, Blanco-Prieto, Serre, & Horcajada, 2014). The fact that the study of this material type on the nanoscale is the most significant yield is the increased permeability and retention effect of the developed metal-organic frameworks, increasing the accumulation of particles in the tumor tissues (Fang et al., 2011).

Metal-organic skeletons have advantages over traditional nanoparticles in drug delivery systems. It is aimed that the drug is delivered to the tumor tissue as much as possible, increasing the effectiveness of the developed nanoparticles and not affecting the healthy organs and tissues. For this reason, the use of nanoscale metal-organic frameworks would be very advantageous. Metal-organic frameworks have improved advantages of improved permeability and retention and different advantages than conventional drug release and transport systems. First, the drug loading capacity of MOFs is relatively high, and the size of the cavity pores they have is known. The encapsulation process can be done quickly by choosing a suitable MOF according to the size of the drug or biological material to be encapsulated. The second advantage is that, due to the

biodegradable property that comes from weak coordination bonds, MOFs break down into their constituent components when degraded (M. X. Wu & Yang, 2017).

Applications of non-toxic metals or metals with low toxicity (e.g., Fe, Zn, Ca, Mg, Bi) and ligands (such as amino acids) to form porous structures are biodegradable in aqueous solutions and/or physiological conditions. Thanks to the surface properties of MOF, biological adjustability of the accumulation of several active molecules can be further modulated by the inclusion of different polar or non-polar surface groups on the ligand, and the MOF structure can be made flexible and sensitive. These properties make MOF materials particularly suitable for internalization of drugs and controlled drug delivery (Horcajada et al., 2012; Rojas, Devic, & Horcajada, 2017).

Historically, the first method of incorporating therapeutics into the MOF has been by adsorption (Horcajada et al., 2006). This post-synthetic approach requires two steps. In the first step, the MOF with the specified properties is synthesized and activated. In the second step, a biologically active compound is incorporated into the pores of the MOF by chemical (covalent attachment to the structure) or physical adsorption (non-covalent attachment). In addition, He et al. should note that lower loadings are achieved in the case of nano-sized MOFs (NMOF or MOF nanoparticles) compared to bulk MOF materials (He, Liu, & Lin, 2015). The main disadvantages of this approach include the heterogeneous distribution of the active compound throughout the MOF structure. This heterogeneity makes the delivery kinetics challenging to control, which reduces the utility and efficacy of the drug. In the case of chemisorption, API forms chemical bonds with the host structure. Upon losing the chemical identity of the API process, it should be ensured that there is no loss in the biological activity of the API as a result. Also, to enable the delivery of an API, the adsorbed molecules must be separated under the necessary conditions. Systems that recover their biological activity through some degradation process when they reach their specific target are commonly referred to as prodrugs. An API covalently linked to a MOF is an example of this approach. The major disadvantage of covalent bonding (similar to the physical adsorption situation) is heterogeneous drug distribution. In this case, drug molecules generally tend to concentrate on the outer surface of the MOF (He et al., 2015). The first application of MOF as a drug carrier was reported in 2006 by Horcajada et al. Ibuprofen was adsorbed in the mesoporous chromium(III) carboxylates MIL-100 (Cr) (0.35 g/g) and MIL-101 (Cr) (1.38 g/g) structures.

Non-covalent coupling method was used (but separate some of the Ibuprofen coordinates to the metal site so it can also be considered chemisorption). They reported

that the drug was entirely administered 3 days after MIL-100 (Cr), while for MIL-101 (Cr), it was administered six days later and was stable in the first eight hours (Horcajada et al., 2006; Kaskel, 2016). A similar approach, MIL-53 (Cr) and MIL-53 (Fe) for flexible microporous chromium(III) and iron(III) terephthalates, could reverse pore sizes as a function of different stimuli (temperature, pressure, adsorbate). The very long (3 weeks) and unusual zero-order kinetic drug release from both times is a result of the flexibility of the framework (using carboxylic ibuprofen groups and the hydroxyl groups of the host material, formation of hydrogen bonds between them) that adapts the pore size to the dimensions of the drug to optimize drug-matrix interactions. Similar drug loadings (approximately 0.2 g/g) were observed in both MOFs (Cr and Fe). Reasonable values of available pore volume were the primary cause of low drug loading (Horcajada et al., 2008). The adsorption approach is the most widely applied approach for antiviral drugs ((azidothymidine triphosphate (AZT-Tp), cidofovir (CDV), busulfan (BU), and doxorubicin (DOX)) as well as anticancer drugs (Horcajada et al., 2010).

As an example of covalent bonding, Taylor-Pashow et al. synthesized nanometric iron (III) aminoterephthalate MIL-101-Fe (~ 200 nm). Next, BODIPY (a fluorescent derivative of the anticancer drug vinblastine) was covalently linked post-synthetically to the amine group of nano MOFs. Loading was in the 11% (w/w) range. In the same study, the drug c, c, t-[PtCl2(NH3)2(Out)O2CCH2CH2CO2H] (ethoxysuccinato-cisplatin) was added to the amine group of the nano amino-MIL-101 ligand with an equal 12.8% (w /w) loading (Taylor-Pashow, Della Rocca, Xie, Tran, & Lin, 2009). Compared to the non-covalent attachment approach, covalent attachment prevents early drug delivery because the drug is usually delivered after the degradation of the entire structure (Bieniek et al., 2021).

1.4. ZIF Family

The unprecedented advantages of nanomaterials have been introduced as a powerful platform in biomedicine that can play a vital role in treating and diagnosing many diseases in recent years (D.-E. Lee et al., 2012). For example, biomedical applications of porous materials such as metal-organic frameworks (MOFs) have been extensively investigated to produce new drug formulations with better biological

performance than conventional drugs (Cai et al., 2019a; K. Lu, Aung, Guo, Weichselbaum, & Lin, 2018; J. Zhou, Tian, Zeng, Song, & Bian, 2018). The zeolite imidazole ester skeleton compound (ZIF) is composed of tetrahedral units and has a similar structure to SiO2. A divalent metal M2+ cation (usually Zn2+) and four imidazolium anions (I'm-) are the main compositions of ZIF (Park, Ni, Côté, Choi, Huang, Uribe-Romo, Chae, O'Keeffe, et al., 2006). As a subfamily of metal-organic framework material (MOF), ZIF has desirable properties, including exceptional chemical stability due to high porosity, excellent thermal and mechanical stability, tunable surface properties, and high resistance to alkaline water and organic solvents (Park, Ni, Côté, Choi, Huang, Uribe-Romo, Chae, O'Keeffe, et al., 2006). These features made ZIFs excellent candidates for many applications such as gas capture (R. Banerjee et al., 2009), separations (Y. S. Li et al., 2010), chemical sensors(G. Lu & Hupp, 2010), drug delivery(C.-Y. Sun et al., 2012), and catalysis. From a structural point of view, ZIFs are constructed by coordination between M2+ cations and imidazole (I'm) anions which; where I'm acts as a linker to form connecting bridges between metal centers of M(I'm)4 tetrahedral units (Park, Ni, Côté, Choi, Huang, Uribe-Romo, Chae, O'Keeffe, et al., 2006; Xu et al., 2020). ZIFs are mainly prepared by both organic (Cravillon et al., 2009; Park, Ni, Côté, Choi, Huang, Uribe-Romo, Chae, O'Keeffe, et al., 2006), and aqueous solutions by solvothermal methods (Pan, Liu, Zeng, Zhao, & Lai, 2011). Binder modifications or encapsulation of guest species (for example, nanoparticles (NPs)) within ZIFs have been widely used to control the functionality of ZIFs. In addition, the pore size of ZIFs is simply adjustable, resulting in tunable molecular diffusion/mass transfer and loading of large cargoes (Karagiaridi et al., 2012; J. Yang et al., 2017). This unique feature has dramatically expanded the application of ZIFs to catalysis and drug delivery (Cai et al., 2019b; Yao, He, & Wang, 2015). Much like aluminosilicate zeolites, ZIFs consist of tetrahedral transition metal ions, namely Co^{2+}, Zn^{2+}, Cu^{2+}, or Fe^{2+}, and I'm linkers where I'm units bridge to connect metal centers. For example, ZIF-8 is formed by coordination between the 2-MeIm and cationic ions of Zn^{2+}(Park, Ni, Côté, Choi, Huang, Uribe-Romo, Chae, O'Keeffe, et al., 2006; Troyano, Carné-Sánchez, Avci, Imaz, & Maspoch, 2019).

The crystal size and morphology of ZIFs can also be controlled during the synthesis process by the type of solvent and metal salt, the ratio of metal salt to I'm binder, the mixing order of ZIF precursors, and the addition of surfactants (Cai et al., 2019b). The stability of ZIFs under physiological conditions and their pH-dependent degradability under acidic conditions make such MOFs highly attractive for creating pH-sensitive drug

delivery systems (DDSs) (Yao et al., 2015; Zhuang et al., 2014). As a result of the slightly acidic state of the tumor microenvironment (TME), ZIFs, particularly ZIF-8, have been extensively investigated as both in vitro and in vivo nanocarriers for cancer ablation (Adhikari, Das, & Chakraborty, 2015; L. Gao, Chen, Gong, Liu, & Li, 2019; M. Zheng, Liu, Guan, & Xie, 2015). Moreover, ZIF is multifunctional in cancer therapy (Q. Wu et al., 2018) and antimicrobial applications (Q. Wu et al., 2018), bioimaging (Shen, Liu, Lei, & Ju, 2018), and therapeutics. Many research efforts have been devoted to the new design of based composites (J.-C. Yang, Shang, Li, Cui, & Yin, 2018).

These porous nanostructures can be formed in organic solvents such as dimethylformamide (DMF) (Park et al., 2006) and methanol (Cravillon et al., 2009) by hydrothermal or solvothermal methods or aqueous solutions even reaction temperatures from room temperature to 200°C and reaction times ranging from hours to days (B. Chen, Yang, Zhu, & Xia, 2014; Pan et al., 2011). Although hydrothermal/solvothermal methods are widely used to prepare simple and easy ZIF-based nanostructures, such methods are difficult to scale and yield low products (Qu et al., 2018). To overcome the shortcomings, sonochemical (Cho, Kim, Kim, & Ahn, 2013) and mechanochemical (Yamamoto et al., 2013) methods were used to increase the efficiency of ZIF production. However, due to the wide range of controllable parameters, including synthesis routes, concentration and molar ratio of reactants, reaction temperature, solvents, and reaction time, there is a long way to go to industrialize the production of ZIF-8 and its other members (Qu et al., 2018). Green and sustainable production of ZIFs under mild synthesis conditions and non-toxic solvents (Pan et al., 2011) and solvent-free methods(Y.-R. Lee et al., 2015; Tanaka, Kida, Nagaoka, Ota, & Miyake, 2013) is significant in environmental protection. For example, in 2017, a fast and scalable method for the synthesis of hierarchical ZIFs, namely ZIF-8 and ZIF-67 and one-pot encapsulation of dyes or protein cargoes using organic base trimethylamine (TEA), was reported by Zou and colleagues. The addition of TEA to the Zn(NO3)2 6H2O solution promoted the formation of ZnO NPs, which rapidly converted to ZIF-8 NPS after the addition of 2-MeIm as a binder(Abdelhamid, Huang, El-Zohry, Zheng, & Zou, 2017).

1.5. ZIF-8

ZIF-8, one of the significant ZIF nanomaterials subgroups, makes the ZIF shell multifunctional while maintaining the structural crystallinity and porosity(W. H. Chen et al., 2018; K. Dong, Wang, Zhang, Ren, & Qu, 2018; Lian et al., 2017; M. Zheng et al., 2015). It should be noted that among the ZIF family, ZIF-8 is formed with biocompatible zinc and 2-methylimidazole, which imidazole is an essential component of amino acid histidine and zinc is the second most abundant transition metal element in living organisms(C.-Y. Sun et al., 2012; Vasconcelos et al., 2012; Zhuang et al., 2014), which is one of the leading members that is used extensively in many applications such as adsorption, catalysis, electrochemical energy storage, gas separation, drug delivery, sensing and electronics(L. Gao et al., 2019; Park, Ni, Côté, Choi, Huang, Uribe-Romo, Chae, O'Keeffe, et al., 2006).

ZIF-8 is widely reported as the most effective and promising drug delivery carrier for tumor therapy due to its chemical and thermal stability under neutral conditions. They are potential drug delivery carriers due to the satisfactory drug loading, ideal drug delivery capacity, low cytotoxicity, and biodegradability(Mengran, 2020). The disintegration of ZIF-8 in acidic media causes the release of Zn2+ ions that inhibit the Krebs cycle and induce the permeability transition of the mitochondrial inner membrane, enhanced production and accumulation of ROS leading to cell cycle arrest at the G2 phase, irreversible DNA damage subsequently initiating the apoptotic pathways(Mengran, 2020).

Due to its weak coordination bonds, ZIF-8 degrades at low pH values, and at the same time, its hydrophobic lattice structure does not appear to degrade at a body pH of 7.4. For this reason, it provides pH-sensitive transport of drugs to regions with more acidic pH, such as cancer tissues. Its biodegradable structure gives zinc and 2-methylimidazole to the environment simultaneously with drug release in cancerous tissues. ZIF-8 bright material was synthesized by the one-pot method. This synthesis method has led to the use of ZIF-8 material in biological research, and the encapsulation of molecules such as doxorubicin, rhodamine B, methyl orange, and methylene blue into the spaces of ZIF-8 was successfully performed (H. Zheng, Zhang, Liu, Wan, Guo, Nyström, et al., 2016). In addition, ZIF-8 with large hydrophobic and hydrophilic molecules such as caffeine (Liédana, Galve, Rubio, Tellez, & Coronas, 2012), cyt-c enzyme(C. Zhang et al., 2017),

turmeric(M. Zheng et al., 2015), methyladenine (3-MA)(M. Zheng et al., 2015), insulin(Duan et al., 2018), protein(G. Yang et al., 2018) have been allowed by the one-pot method. Looking at the anticancer molecules studied with ZIF-8, doxorobucin(H. Zheng, Zhang, Liu, Wan, Guo, Nyström, et al., 2016), 5-Fluorouacil(C.-Y. Sun et al., 2012), camptothecin(Zhuang et al., 2014), 6-Mercaptopurine(Kaur, Mohanta, Gupta, Kukkar, & Tyagi, 2017). ZIF-8 based drug delivery systems also provide combinatory tumor therapy strategies, such as chemotherapy and photodynamic therapy, chemo-photothermal therapy, chemotherapy and microwave thermal therapy, chemo-, photothermal-, photodynamic- and immuno-therapy and theranostic(Maleki, Shahbazi, Alinezhad, & Santos, 2020).

In the study conducted to examine the biocompatibility of ZIF-8, kidney, skin, metastatic breast, blood, bone, connective tissue cell lines were studied. As a result of this study, it was underlined that ZIF-8 is suitable for therapeutic applications. This study determined that the concentration value of ZIF-8 of 30 µg/mL is the upper limit to prevent cytotoxic effects on cell lines. It has been observed that when applied above this value, it increases reactive oxygen species (ROS) due to intracellular zinc release and leads to controlled death of cells(Hoop et al., 2018). In another study, it was seen that this drug delivery system had a minimum effect on the liver and kidney. It was revealed that it is ideal as a drug delivery system with its effect on system and blood biocompatibility and immune system (Hoop et al., 2018; S. Li et al., 2016). It is known in the literature that ZIF-8, as a source of zinc, may have a supportive effect on treatment. It has been shown that when doxorubicin is encapsulated into ZIF-8 and applied to HeLa cell lines, it has a supportive effect on cancer by increasing ROS (C. Zheng, Wang, Phua, Lim, & Zhao, 2017).

Type of sodalite bonded with Zn^{2+} by 2-MeIm has a frame containing 11.6 Å diameter lattices of ZIF-8 with a huge surface area of 1630−1700 m /g, accessible through a narrow six-ring pore (3.4 Å) and forming a post-working inner porosity. As a result of ultra-high thermal stability (stable up to 550 °C under an inert atmosphere), ZIF-8 can maintain its original structure in boiling water / organic solvents for seven days and even 8 molars NaOH (aqueous) at 100 °C. It is stable at 24 hours (Park, Ni, Côté, Choi, Huang, Uribe-Romo, Chae, O'Keeffe, et al., 2006).

The overall objective of the proposed project is to develop a new generation of intelligent, biocompatible, biodegradable, and multifunctional nanocarrier systems for the treatment of hepatocellular carcinoma (HCC) and prostate cancer to characterize its

cytotoxic effect by characterizing this nanocarrier. For this purpose, the sorafenib used in the treatment of HCC and apalutamide used in treating prostate cancer will be encapsulated into the ZIF-8 smart material to be formed with zinc and 2-methylimidazole. The material obtained will be examined in detail after the structural and functional effects of the new molecules in HCC and prostate cancer cell lines.

CHAPTER 2

CHARACTERIZATION AND INVESTIGATION OF CYTOTOXIC EFFECTS OF DOXORUBICIN LOADED ZIF-8 METAL-ORGANIC FRAMEWORKS SYNTHESIZED WITH DIFFERENT ZINC SOURCES

2.1. Aim of the study

The aim of this study is to develop a new generation of intelligent, biocompatible, biodegradable, and multifunctional nanocarrier systems for the treatment of human lung cancer cells to investigate its cytotoxic effect by characterizing this nanocarrier. Doxorubicin was encapsulated into the ZIF-8 smart material to be formed with zinc and 2-methylimidazole in various molar ratios compared characterizations and in cytotoxic activity in A549 lung cancer cells.

2.2. Doxorubicin

The search for anticancer compounds from soil-based microorganisms began in the 1950s. A new strain of Streptomyces peucetius, producing a bright red pigment, was isolated and produced as an antibiotic from this bacterium, which was found to have good activity against mouse tumors. The new compound was named daunorubicin and has been used successfully to treat acute leukemia and lymphoma (Arcamone et al., 1969; Brockmann, 1963). However, in 1967 it was recognized that daunorubicin could produce fatal cardiac toxicity (Rivankar, 2014).

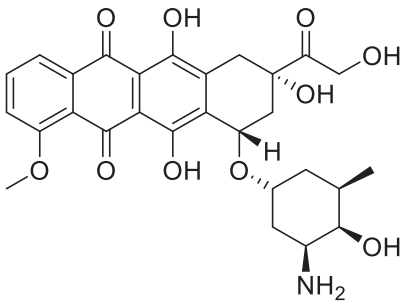

Figure 2.1. Structure of Doxorubicin

The researchers made genetic mutations into Streptomyces spp to produce a compound called Adriamycin, which was later called Doxorubicin. Despite the higher therapeutic index of Doxorubicin, cardiotoxicity remained a significant problem. These compounds became prototypes for subsequent research, and today there are more than 2000 known analogs of doxorubicin (Rivankar, 2014).

The exact mechanism of action of Doxorubicin is complex and still unclear. Doxorubicin inhibits macromolecular biosynthesis by intercalating with DNA (Fornari, Randolph, Yalowich, Ritke, & Gewirtz, 1994; Momparler, Karon, Siegel, & Avila, 1976). This further inhibits the progression of the enzyme topoisomerase II and relaxes the supercoils in DNA for transcription. Doxorubicin stabilizes the topoisomerase II complex after breaking the DNA chain for replication, preventing the reclosing of the DNA double helix and thus stopping the replication process. Another mechanism of Doxorubicin HCl is its ability to generate free radicals that cause DNA and cell membrane damage (Rivankar, 2014).

Doxorubicin is most commonly used to treat the bladder, breast, stomach, lung, ovaries, thyroid, soft tissue sarcoma, multiple myeloma, and Hodgkin lymphoma cancers. Commonly used doxorubicin-containing regimens may include Adriamycin, cyclophosphamide (AC), Taxotere, AC, Adriamycin, bleomycin, vinblastine, dacarbazine, bleomycin, etoposide, AC, vincristine, procarbazine and prednisone, cyclophosphamide, Adriamycin, Adriamycin, and vancomycin. 5-Fluorouracil, AC. Doxil is mainly used to treat advanced or relapsed ovarian cancer after platinum-based chemotherapy or in the treatment of AIDS-related Kaposi's sarcoma (Petit & Biard, 2013; Rivankar, 2014).

2.3. Doxorubicin-ZIF-8

Due to the side effects of traditional doxorubicin treatment, the need to develop a liposomal formulation with equal efficacy and fewer side effects arose. One of the main advantages of using liposomes as a delivery system is that the phospholipids used to form these vesicles are extracted from natural sources such as egg yolk or soybean and are safe in the body. In addition, the degree of saturation of the phospholipid bilayer can be varied to change the drug release rate. Liposomes, consisting of natural phospholipids mixed with varying amounts of cholesterol, are removed from the circulation by the reticuloendothelial system (RES) within a few minutes to several hours after removing opsonins from plasma. Due to this short circulation half-life, the use of conventional liposomes has limited clinical applications (Rivankar, 2014).

For the first time, Sun et al. demonstrated that ZIF-8 could be used for the in vitro delivery of anticancer drugs. 660 mg of 5-FU was significantly loaded In 1 g of ZIF-8, and pH-induced controlled release of the drug was observed, which was much faster at acidic pH (pH 5) than neutral pH (pH 7.4). This suggests that ZIF-8 is an excellent pH-sensitive DDS (C.-Y. Sun et al., 2012). However, since the pore window of ZIF-8 is 3.4 Å, this structural feature causes the penetration of large molecules into the pores, thus resulting in low cargo loading in the pores and burst release as a result of drug adsorption on the surface of the particles(H. Ren et al., 2014; Vasconcelos et al., 2012). To overcome this obstacle, a simple process combining ZIF in one-pot synthesis and cargo encapsulation has been reported by Zheng et al. In this process, the anticancer drug DOX and three organic dyes were successfully encapsulated in ZIF-8 and ZIF-67 with high cargo loading (14-20%). First, the metal ion and dye/drug molecules self-assemble to form coordination polymers. After the addition of organic linkers, the coordination polymers were disassembled, and thus the next generation ZIF network resulted in encapsulation of target molecules within ZIF hosts. The drug/dye-loaded crystals had hierarchical pore structures containing ordered micropores and homogeneously distributed mesopores filled by guests. Interestingly, hierarchical micro-and mesoporous ZIF-based structures were harvested by removing organic drug/dyes from the pores. DOX-loaded ZIF-8 exhibited pH-sensitive release behavior where the drug was not released under physiological conditions (pH 7.4), while the release of the drug occurred in a controlled manner at lower pH values of 5.0-6.5. Cytotoxicity analyzes on breast

cancer cell lines showed that DOX@ZIF-8 had higher toxicity than free DOX(H. Zheng, Zhang, Liu, Wan, Guo, Nyström, et al., 2016). In a different study on the controlled release behavior of DOX loaded on ZIF-8 and ZIF-7, it was shown that this ZIF-8 releases the drug in a more controlled manner than ZIF-7 under acidic conditions, which means ZIF-8 It was emphasized that ZIF species would be effective in the design of controlled DDSs by showing that it is more stable than the ZIF-7 carrier at acidic pH (Adhikari et al., 2015).

2.4. Materials and Methods

2.4.1. Synthesis and optimization of ZIF-8 and Doxorubicin@ZIF-8 nanoparticles

Synthesis of the small size of ZIF-8 nanoparticles was carried out with the minor modifications to be made in the method of Pan et al. (2011)(Pan et al., 2011). In this study, ZIF-8 was synthesized such that the Zn^{+2}:2-methylimidazole: H_2O molar ratio of 1:70:1238 was obtained (Kaur et al., 2017). According to these values, $Zn(NO_3)_2.6H_2O$ (585 mg) was dissolved entirely with 4 mL of DI water. On the other side, 2-methylimidazole (2-MeIM) (11.35 g) was dissolved in 40 mL of DI in water, and 6 mL of DMSO solution was added. Then two solutions are mixed together to form a white solution. After the mixture was continued for 5 minutes in room conditions, centrifuging at 14,000 rpm for 15 minutes caused precipitation of the white powders. Unreactants were removed by washing the solution three times with methanol and overnight at 65oC to obtain ZIF-8 nanoparticles.

For the synthesis of DOX@ZIF-8 nanoparticles, the same method described above was applied. In this study, 50 mg DOX was dissolved in 6 mL of DMSO and added to the dissolved 2-methylimidazole solution, and added to the dissolved zinc nitrate solution after stirring for 5 minutes. Other steps were continued as the ZIF-8 synthesis.

2.4.2. Nanoparticle Yield and Encapsulation Efficiency

The yield of the nanoparticles was determined by gravimetry after washing and drying a known volume of nanoparticle suspension. The drug loading and encapsulation efficiency were investigated directly by inductively coupled plasma- optical emission spectrometry (ICP-OES) (Agilent 5110 Dual View, United States). In ICP-OES analysis, the particles were decomposed in an aqueous solution of 5%HNO_3 prior to the measurement, and thus, the Zn compositions of the whole particle material were obtained. The encapsulation efficiency of the active agents was calculated as follows:

Encaps. efficiency (%) = (mass of drug in nanocomposite/mass of total loaded drug) × 100

2.4.3. Characterization of ZIF-8 and DOX@ZIF-8 nanoparticles

The synthesized nanoparticles were characterized by various analytical techniques in terms of properties such as particle charge, size and distribution, surface property, drug loading, and release activities.

The particle size and the zeta potential value are the parameters that must be examined because of the colloidal stability in the structure and the fact that the particle has a significant impact on the cellular retention rate in vitro applications. For this reason, Zetasizer Nano Z (Malvern Panalytical, United Kingdom) using Dynamic Light Scattering Method (DLS) ZIF-8 and DOX@ZIF-8 nanoparticles particle size and zeta potential was determined and examined. In addition, the dimensions of the nanoparticles to be generated by scanning electron microscopy (SEM) was verified. The samples were displayed using the 5 VK electron beam and 200 nm scale using the FEI QUANTA 250 FEG(USA) device. In addition, the images to be obtained by SEM analysis gave information about the structure properties (porosity, layer thickness, morphology) of the nanoparticle. Energy Dispersive X-ray Spectroscopy (EDX) was used to determine the elemental composition of ZIF-8 and DOX@ZIF-8 nanoparticles. X-Ray Diffraction Device (XRD) measurement was determined the crystallinity and impurity of the

nanoparticles to be formed. XRD analysis was performed by using the CuKα radiation in the Philips Xarakpert Pro diffractometer (Royal Philips Electronics, Amsterdam, The Netherlands) with a beam length of 1.541 A and keeping it at 40 kV and 25 mA. With the Fourier Transform Infrared Analysis (FT-IR) (PerkinElmer, USA), the functional groups present in ZIF-8 and ZIF-8 with DOX were examined.

2.4.4. Determination of Zn^{2+} Concentration

ZIF-8 nanoparticles were dissolved in three different solutions. ZIF-8 nanoparticles were dispersed in phosphate-citrate buffer at pH 5 and 6 and PBS at pH 7.4. Samples agitated at 150 rpm were centrifuged after five days, and the supernatants were transferred to a new tube for additional preparation steps. For pickling, after obtaining a 1:10 or 1: 50 dilutions with HCl and DI water, the samples were analyzed by flame atomic absorption spectroscopy at a wavelength of 213.9 nm.

2.4.5. Cell Culture

Cells were cultured in a CO2 incubator set at 37°C in RPMI 1640 or DMEM F/12 medium containing 5% penicillin/streptomycin, 5% L-glutamine, and 5-10% fetal bovine serum. The viability and proliferation of the cells were achieved by passaging the flasks after covering the 80% culture dish. Cells that actively proliferate in the logarithmic phase were used in the experiments.

2.4.6. Cell Viability and Cytotoxicity Test

The survival and growth trends of ZIF-8 and DOX@ZIF-8 nanoparticles on A549 cells were determined by MTT cell proliferation assay. The MTT test is a colorimetric test based on a sensitive, quantitative and reliable cell culture that measures cell viability, growth, and activation of cells. The test is based on the conversion of the water-soluble yellow 3-(4,5-dimethylthiazol-2-yl)-2,5-diphenyl tetrazolium bromide (MTT) substrate

into the water-insoluble purple formazan substrate of the living cells due to the mitochondrial dehydrogenase enzyme capacity. The amount of formazan produced is directly proportional to the number of live cells. The MTT test is a valuable method in determining the cells that are not dividing but still active(Mosmann, 1983),(Freshney et al., 1994). For this purpose, cells at a concentration of 5000 cells/well were seeded into 96-well cell culture dishes. These cells are incubated for 24 hours at 37°C, with 95% humidity and 5% CO2. After 24 hours, cells were incubated at various concentrations of ZIF-8 and DOX@ZIF-8. Samples were sterilized by UV irritation prior to cell culture. After 24, 48, and 72 hours incubation, 5 mg/mL of MTT solution was added, and after incubation at 37°C for 4 hours, formazan crystals were dissolved in DMSO and measured at 570 nm.

2.5. Results and Discussion

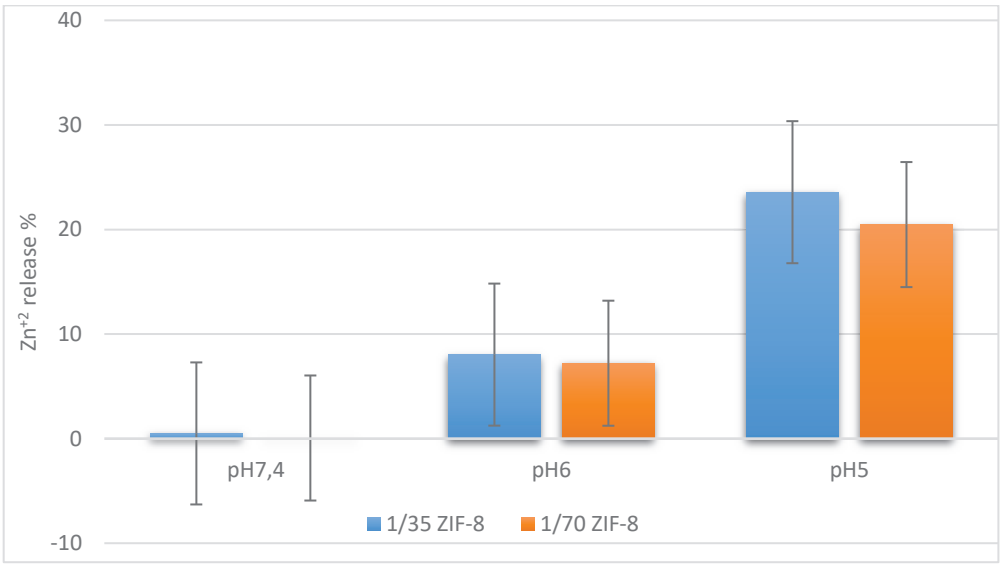

Figure 2.2. Zinc release from ZIF-8 (1:35 and 1:70) at pH 7.4, 6 and 5

Synthesis of the small size of ZIF-8 and DOX@ZIF-8 nanoparticles were carried out with the minor modifications to be made in the one-pot method. To assess the stability of ZIF-8 crystals in different pHs (pH 7.4, 6, and 5), we incubated ZIF-8 for five days and determined the release of Zn^{2+} by atomic absorption spectroscopy (AAS). ZIF-8 is degraded due to their weak coordination bonds at low pH values, so Fig 3. shows an almost linear relationship between pH and Zn^{2+} in the supernatant.

Table 1. Drug loading capacity of ZIF-8 in different Zinc salts

rxn time(min)	$Zn(NO_3)_2.6H_2O$	$Zn(CH_3CO_2)_2.2H_2O$	$ZnBr_2$	$ZnCl_2$
5	96,76	88,83	93,37	88,84
10	91,15	88,10	97,08	92,42
15	88,79	88,78	87,59	89,71
30	88,10	88,43	86,50	89,92

UV-Vis absorption spectroscopy has been used to determine the adequate DOX storage capacity. Firstly, the final adsorbed DOX depends on the relative affinity between the solvent, DOX, and the porous internal surface. Owing to the different polarity, the amounts of DOX were more significant using methanol rather than water as solvent(K. Ren, Wang, & Liu, 2021). In the same way, DOX loading capacity varied with the DOX to different Zn salts. Finally, the reaction time was also necessary; the loading capacity was not changed.

When the solvent changes with methanol, drug loading capacity decreases to 63,72%. On the other hand, doxorubicin absorption after synthesis of ZIF-8, loading capacity is 87,03%.

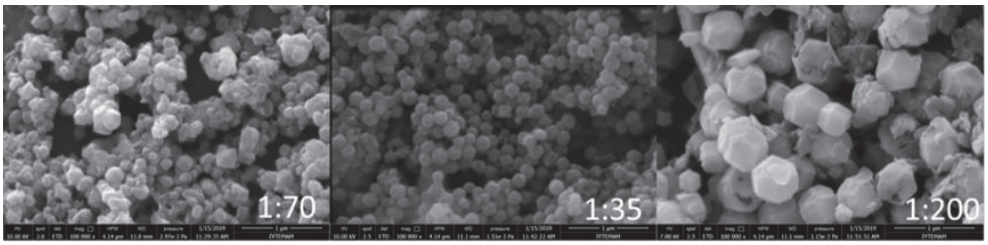

Figure 2.3. SEM micrographs of ZIF-8 from different Zn^{+2}: 2-MeIM ratios; 1:70, 1:35 and 1:200

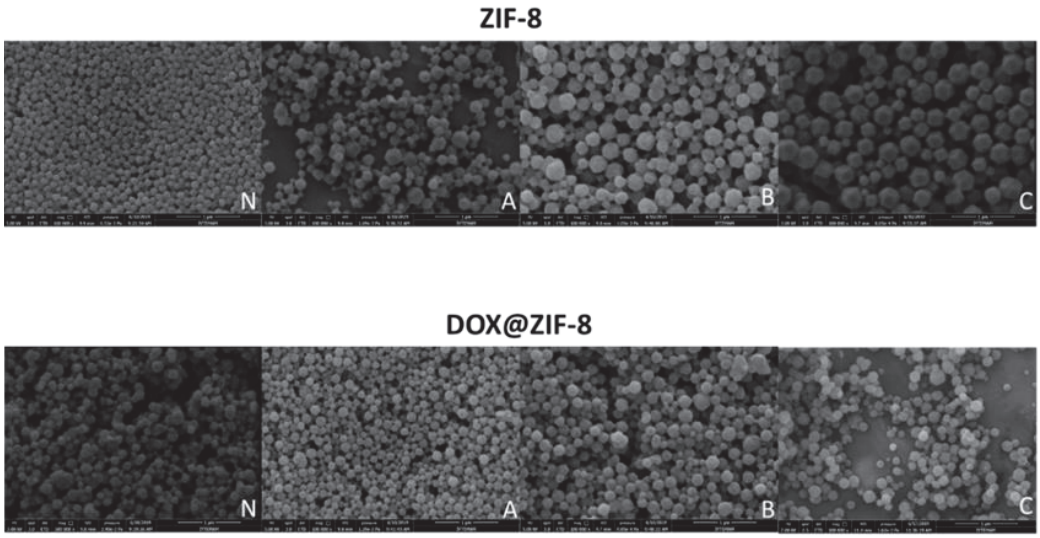

Figure 2.4. SEM micrographs of ZIF-8 and DOX@ZIF-8 from different Zinc sources

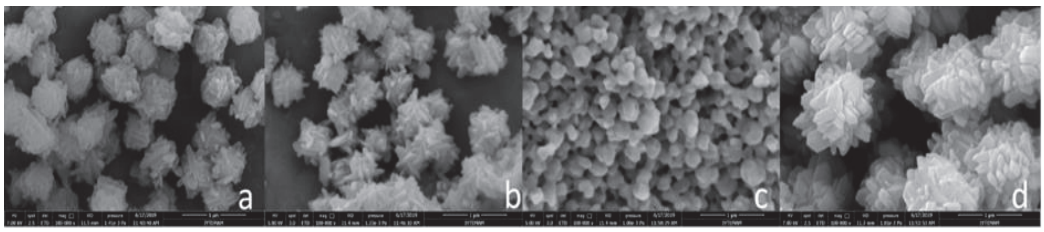

Figure 2.5. SEM micrographs of ZIF-8 and DOX@ZIF-8 from using methanol:H_2O 1:3 different Zn ratios nonstirring 6h a) ZIF-8 1:4 mmol b) ZIF-8 0,6:4 mmol c) DOX@ZIF-8 1:4 mmol d) DOX@ZIF-8 0,6:4 mmol

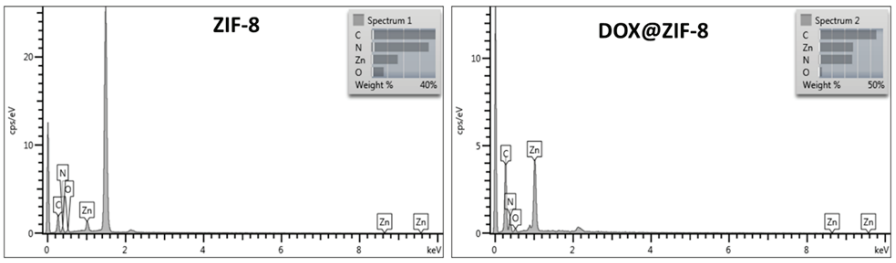

Element	Wt%	Atomic %
C	39.98	50.29
N	35.72	38.53
O	7.80	7.37
Zn	16.50	3.81
Total:	100.00	100.00

Element	Wt%	Atomic %
C	44.81	60.66
N	25.99	30.17
O	2.49	2.53
Zn	26.72	6.64
Total:	100.00	100.00

Figure 2.6. EDX curves and elemental compositions of ZIF-8 and DOX@ZIF-8

Table 2. Particle sizes of ZIF-8 and DOX@ZIF-8 measured by SEM and DLS

	Particle diameters (nm) from SEM	**Particle diameters (nm) from DLS**
ZIF-8	113	226
DOX@ZIF-8	171	361
ZIF-8 A	161	773
DOX@ZIF-8 A	234	837
ZIF-8 B	292	610
DOX@ZIF-8 B	314	662
ZIF-8 C	287	825
DOX@ZIF-8 C	307	869
ZIF-8 1/70	150	340
ZIF-8 1/35	192	403
ZIF-8 1/200	527	809

The particle size was studied by dynamic light scattering (DLS). The obtained nanoparticles can be well dispersed in methanol to form a stable suspension. The average particle size of ZIF-8 and DOX@ZIF-8 was found to be 340 nm and 809 nm from DLS analysis, respectively, showing an increase in the size of the ZIF-8 upon loading of the drug. The DLS-determined mean particle size values from 340 nm to 1047 nm were obtained for ZIF-8 crystals.

Varying the molar ratio of 2-methylimidazole to zinc nitrate can further reduce the crystal size but has little effect on the morphology. The crystal size was reduced when increasing the sonication time. The polydispersity index is around 0.289 measured from dynamic light scattering.

The particle size of ZIF-8 from different Zn salts was further studied by (DLS). With these four reactive zinc precursors (soft Zn^{2+} acid associated with hard bases such as $NO3^{-}$), a considerable amount of Zn^{2+} ions is available to coordinate with Hmim, and the number of nuclei generated by the complex formation is probably mainly resulting in a decrease in crystal size and crystal anisotropy. For this zinc precursor with lower reactivity (soft Zn^{2+} acid associated with the soft Br^{-} base), the density of nuclei is reduced, and nanoparticles grow through further direct addition of single monomeric mim^{-} and solvated Zn^{2+} ion species until the framework is formed.

Scanning electron microscopy (SEM) showed that the ZIF-8 and DOX@ZIF-8 materials consisted of isolated crack-free particles of diameter between 113,89−527,86 nm. As shown in Fig 2.3 and 2.4, scanning electron microscopy (SEM) images of the resulting structures indicate the formation of rhombic dodecahedral crystals, which corresponds to the average size of biomedically relevant ZIF-8 encapsulating biomacromolecules, as previously reported by Falcaro and co-workers(Hoop et al., 2018). As expected,energy-dispersive X-ray (EDX) spectroscopy maps confirm the presence of Zn, C, and N elements uniformLy distributed throughout each crystal.

SEM images indicated that at high concentrations of 2-methylimidazole and zinc nitrate, all of the obtained particles exhibited the cruciate flower-like structure, while the rhombic dodecahedral particles were only formed at high 2-methylimidazole concentration but low zinc nitrate concentration. The above findings suggest that the MOF precursor concentrations and the properties of the biomolecules can both have an influence on the morphology of the synthesized particles, depending on the synthetic conditions(Chu et al., 2018).

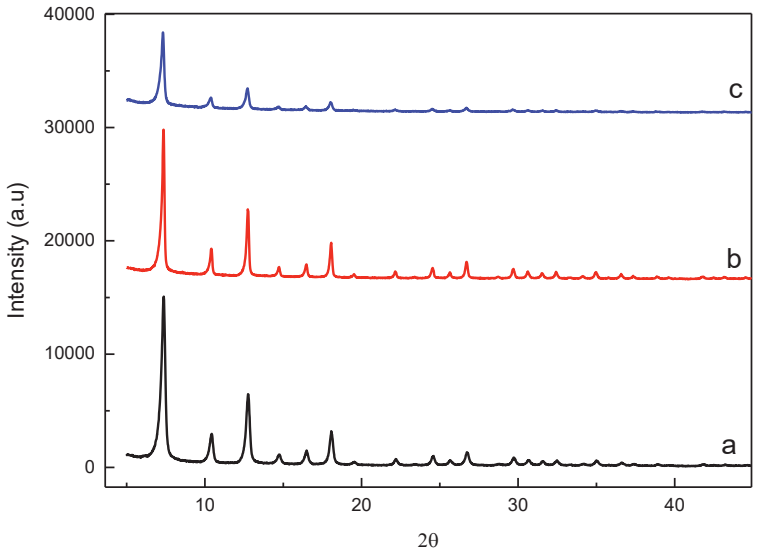

Figure 2.7. XRD patterns of ZIF-8 from different Zn^{+2}: 2-MeIM ratios; a)1:70, b)1:35 and c)1:200

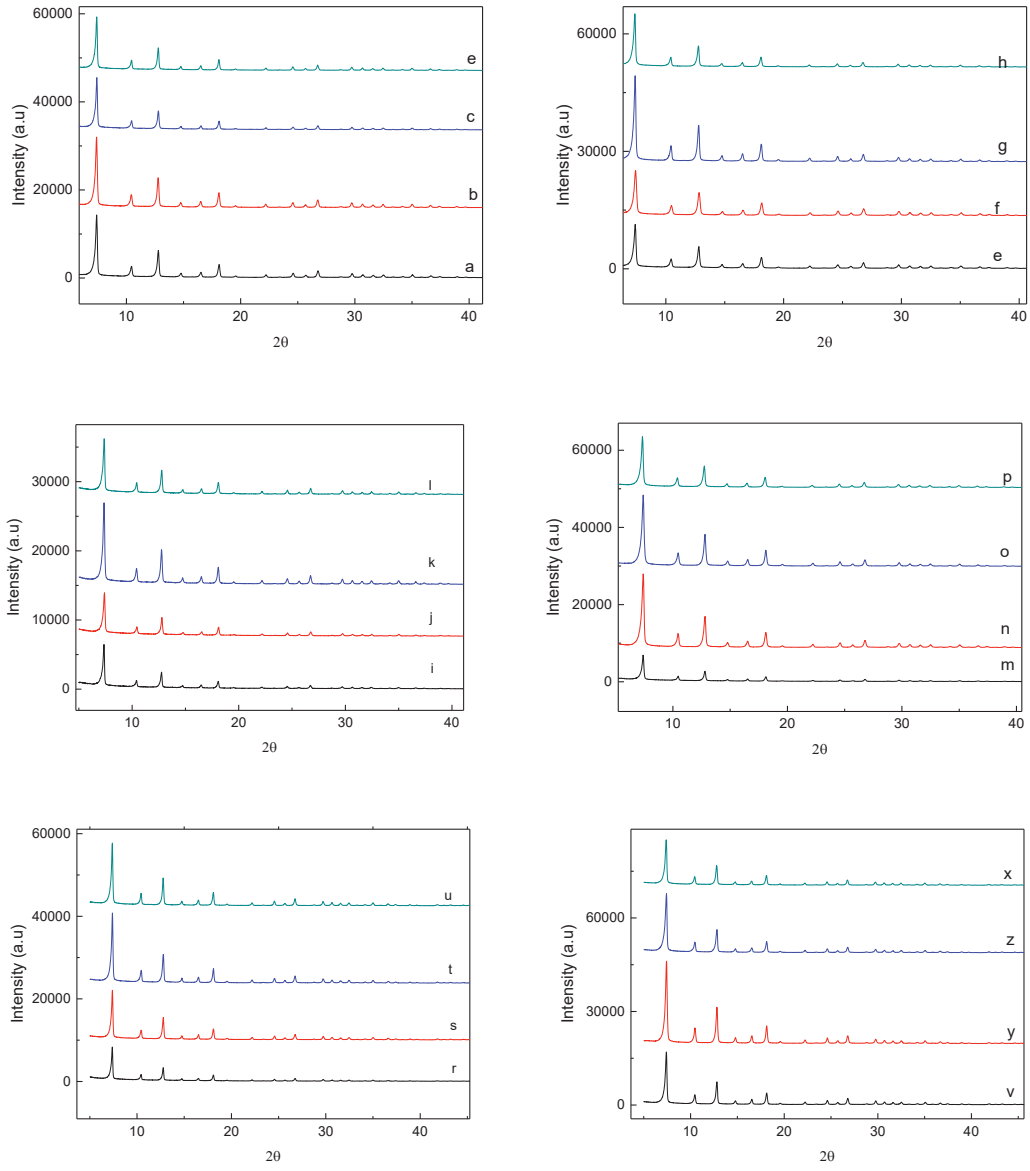

Figure 2.8. XRD patterns of ZIF-8 and DOX@ZIF-8 nanocrystals prepared with different Zinc salts with various reaction times from 5 min to 30 mins. a-d) ZIF-8/A 5-10-15-30 min e-h) DOX@ZIF-8/A 5-10-15-30 min i-l) ZIF-8/B 5-10-15-30 min m-p) DOX@ZIF-8/B 5-10-15-30 min r-u) ZIF-8/C 5-10-15-30 min v-x) DOX@ZIF-8/C 5-10-15-30 min

Comparison of the sample XRD pattern to the pattern simulated from the published ZIF-8 structure data indicates that the product is pure-phase ZIF-8 material. Peak broadening can be clearly observed from the sample XRD pattern, indicating the formation of nanosized crystals. Each synthesis yielded pure-phase ZIF-8 crystals, as demonstrated by X-ray diffraction (XRD) patterns (Fig 5). Patterns generated by the ordered porous structure of the ZIF-8 particles between 2θ values of 5 and 40° can be

observed, and the peak broadening observed indicates the formation of nanosized crystals. The relative intensities and the sharp peaks in the diffraction pattern of ZIF-8 at 2θ=7.11°, 12.5°, 17.75°, and 26.4° prominent peak positions, including 011, 002, 112, 022, 013, and 222, are in good agreement with previous reports,(Cravillon et al., 2009; Park, Ni, Côté, Choi, Huang, Uribe-Romo, Chae, O'Keeffe, et al., 2006) confirming the sodalite structure, which is the typical structure of ZIF-8, and the well-defined peaks revealed high crystallinity. The interplanar spacings calculated using Bragg's law from the reflection at different Bragg's angles correspond to a body-centered cubic structure with a unit cell parameter of 17 Å and are in accordance with those reported in the literature. The growth of ZIF-8 crystals is known to evolve with time from cubes exposing 6 (Al-Salama) faces to intermediate shapes, and finally, to rhombic dodecahedra 23 exposing 12 (Cui et al.) faces, the latter being most likely the stable equilibrium morphology of ZIF-8.

The largest pore size in the ZIF-8 structure has a diameter of ca. 11.6 A° interconnected by 6-ring windows of a diameter of 3.40 A°, whereas Doxorubicin has dimensions of 14.64 610.02 66.90 A°, and XRD analysis of the complex shows unchanged lattice parameters for ZIF-8 previous to and after Doxorubicin loading. Hence, Doxorubicin appears overly large to pass through even the most significant pore entrance.

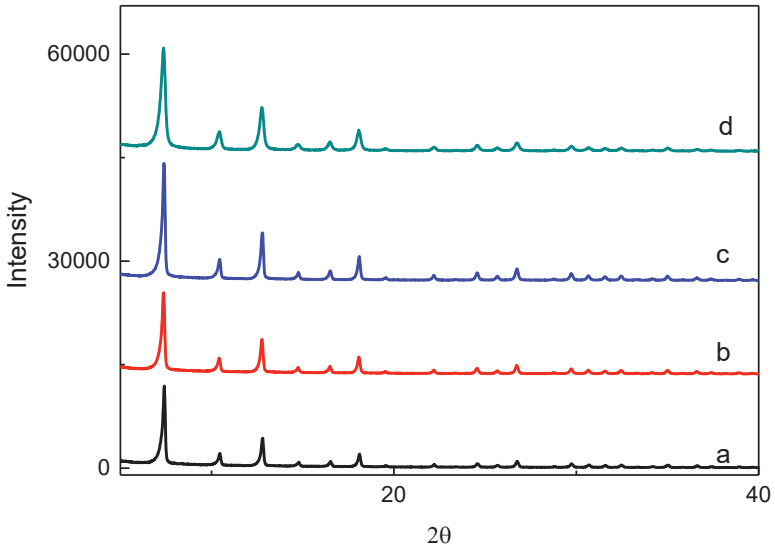

Figure 2.9. XRD patterns of ZIF-8 nanocrystals prepared with different Zinc salts a) ZIF-8/A, b) ZIF-8/B c) ZIF-8/C, d)ZIF-8/N

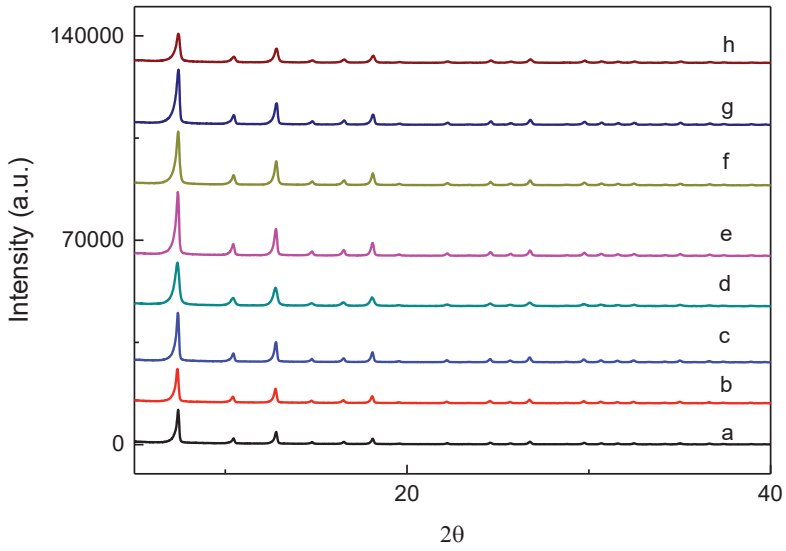

Figure 2.10. XRD patterns of ZIF-8 and DOX@ZIF-8 nanocrystals prepared with different Zinc salts a) ZIF-8/A, b) ZIF-8/B c) ZIF-8/C, d)ZIF-8/N e)DOX@ZIF-8/A, f) DOX@ZIF-8/B g) DOX@ZIF-8/C h) DOX@ZIF-8/N

Figure 2.10 revealed the XRD results of samples derived from distinct zinc salts. The XRD pattern o.f ZIF-8 prepared from $Zn(NO_3)_2.6H_2O$ showed a flat baseline without unusual phases, with only one appropriate to the crystalline structure of ZIF-8. Meanwhile, XRD patterns of ZIF-8 from $ZnCl_2$ and ZnAce possessed abnormal phases besides the main one, attributed to the dense structure of Zn, which is similar to reports(Ta et al., 2018). Thus, different salts had a considerable impact on the formation of ZIF-8. Sample ZIF8 from $Zn(NO_3)_2.6H_2O$ crystallized best, with no Zn phase included because it was prepared from nitrate. The XRD pattern also showed that ZIF-8 from $Zn(NO_3)_2.6H_2O$ owned the largest specific peak width, proving that the sample had the smallest particle size, and this is consistent with the literature(A. Schejn et al., 2014a; Ta et al., 2018). Therefore, among the employed salts, $Zn(NO_3)_2.6H_2O$ was the best one for ZIF-8 synthesis.

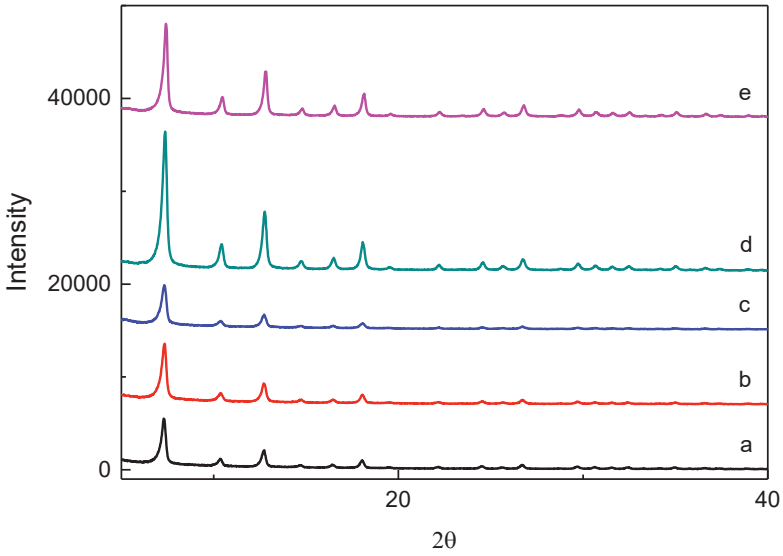

Figure 2.11. XRD patterns of ZIF-8 and DOX@ZIF-8 from using methanol and H_2O as a solvent a) DOX@ZIF-8 ns six h in methanol b) ZIF-8 ns six h in methanol c) ZIF-8 s 6 h in methanol d) ZIF-8 in H_2O e) DOX@ZIF-8 in H_2O.

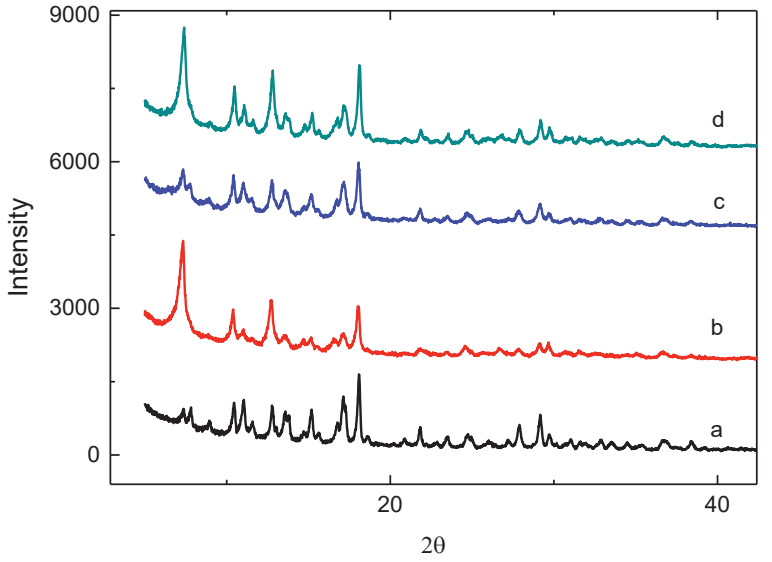

Figure 2.12. XRD patterns of ZIF-8 and DOX@ZIF-8 from using methanol:H_2O 1:3 different Zn ratios nonstirring 6h a) ZIF-8 1:4 mmol b) ZIF-8 0,6:4 mmol c) DOX@ZIF-8 1:4 mmol d) DOX@ZIF-8 0,6:4 mmol

Organic solvent plays a significant role in the synthesis of ZIF-8. In this study, H_2O, MeOH with different volume ratios were employed in order to prepare ZIF-8 in the

same condition. The solvent dissolved zinc salt and Hmim and dissociated H^+ from Hmim to form Mim^-. The Zn^{2+} cations combined with Mim- to form a polymer, and then ZIF-8. Clearly, the higher the polarity of the solvent, the easier H^+ dissociated from Hmim, resulting in a higher ZIF-8 yield. This statement was consistent with the actual yields obtained

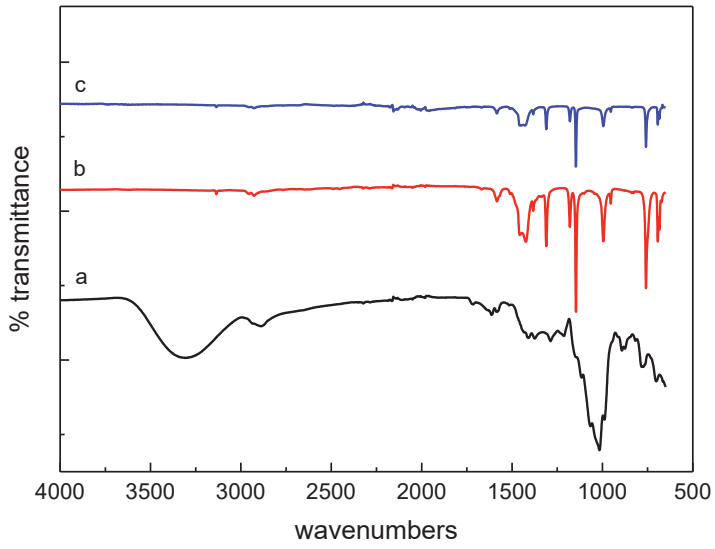

Figure 2.13. FTIR spectra for a) Doxorubicin b) ZIF-8, and c) DOX@ZIF-8.

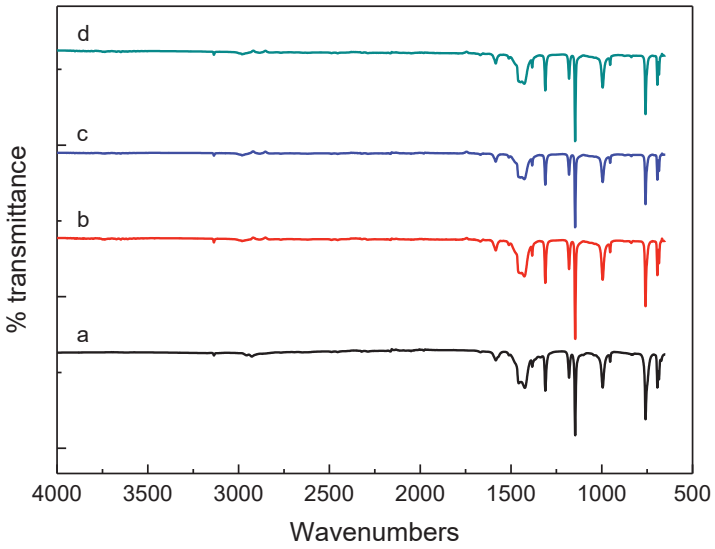

Figure 2.14. FTIR spectra of ZIF-8 from various Zn salts a) ZIF-8/N, b) ZIF-8/A c) ZIF-8/B, d)ZIF-8/C

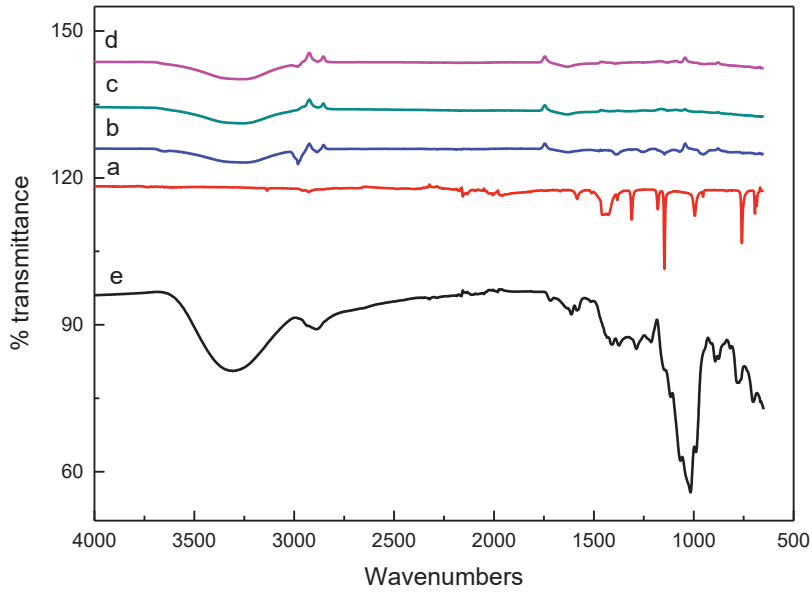

Figure 2.15. FTIR spectra of DOX@ZIF-8 from various Zn salts a) DOX@ZIF-8/N, b) DOX@ZIF-8/A c) DOX@ZIF-8/B, d) DOX@ZIF-8/C e) doxorubicin.

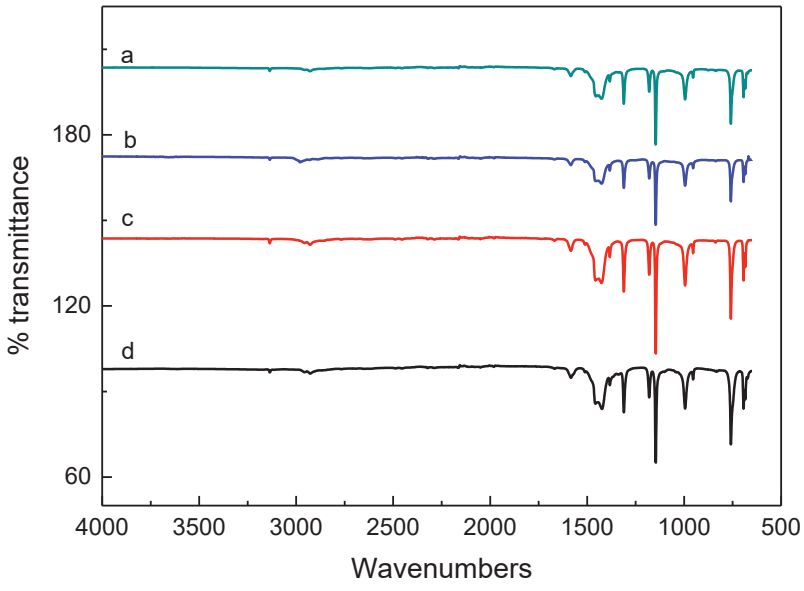

Figure 2.16. FTIR spectra of ZIF-8 and DOX@ZIF-8 from using methanol and H_2O as a solvent a) DOX@ZIF-8 ns six h in methanol b) ZIF-8 ns six h in methanol c) ZIF-8 s 6 h in methanol d) ZIF-8 in H_2O

FTIR spectra were obtained for ZIF-8, Doxorubicin (as a model drug), and the complex DOX@ZIF-8. In the spectrum corresponding to ZIF-8, two bands at 3135 and 2928 cm^{-1} can be observed for the aromatic C–H stretch and the aliphatic C–H stretch of the imidazole, respectively. The 1606 cm^{-1} band is for the C–C stretch, and the peak at 1580 cm^{-1} is for the C–N stretch. The C–N absorption bands are found in the 1100–1400 cm^{-1} region. The absorption band at 421 cm^{-1} is associated with the Zn–N stretching mode. These assignments are in agreement with the FTIR measurements from Park et al.(Park, Ni, Côté, Choi, Huang, Uribe-Romo, Chae, O'Keeffe, et al., 2006). Several bands are observed for Doxorubicin: the band at 3441 cm^{-1} is due to an axial strain of the N–H bond, at 2936 cm^{-1} to C–H axial deformation, at 1635 cm^{-1} to the axial deformation of the C–O bond, and at 100–1260 cm^{-1} to the absorption associated with the stretching of the alcohol group. In the region between 675–900 cm^{-1}, there is an out-of-plane bending of the –OH group that has also been reported by Chouhan et al.(Chouhan & Bajpai, 2009). Noticeably, consistent results are also obtained from products synthesized at different zinc sources and different solvents. These FT-IR results are consistent with pure ZIF-8 that was previously reported in the literature, The FTIR spectrum analysis for the system DOX@ZIF-8 does not undoubtedly show the adsorption of Doxorubicin into ZIF-8, but the detection of characteristic bands for both ZIF-8 and DOX indicates the presence of both compounds. Moreover, the incorporation of Doxorubicin into ZIF-8 is supported by the color change of the ZIF-8 crystals, which were initially colorless, and after the incorporation process, exhibited a purple color.

Doxorubicin interacts with the Zn^{2+} cations via chelating sites comprised of the quinone and the phenolic oxygens on both sides of the anthracycline aromatic moiety. The Zn^{2+} cations in the ZIF-8 structure exhibit tetrahedral geometry coordinated by four neighboring imidazolate groups. It is expected that the Zn^{2+} cations on the surface of the ZIF-8 structure have two imidazolate ligands replaced by water molecules.

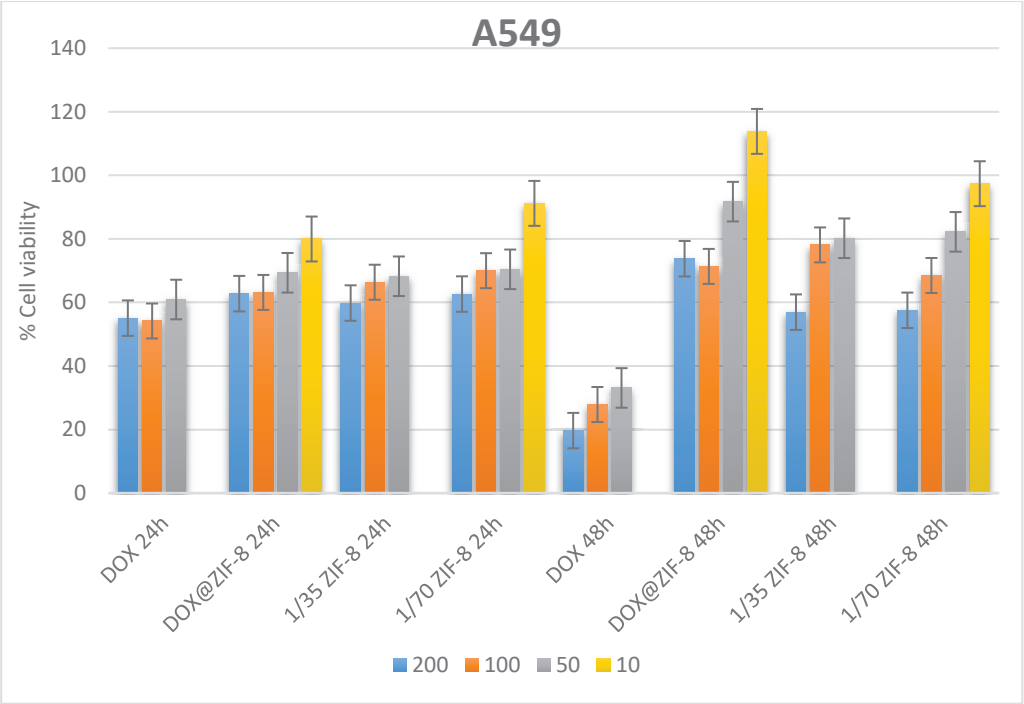

Figure 2.17. Cell viability in A549 cell lines when incubated at 24 and 48 h with the ZIF-8 (1:35 and 1:70) and DOX@ZIF-8 in MTT assay

The cytotoxicities of ZIF-8 and the complex DOX@ZIF-8 were assessed by the colorimetric MTT assay. We assessed the influence of various ZIF-8 concentrations (50, 100, and 200 μg mL^{-1}) and different Zn^{+2}:2-methylimidazole ratios (1:35 and 1: 70) on the cell viability and proliferation response of all A549 cell lines using the MTT assay. MTT assay depends on the reduction activity of intra-cellular, mitochondrial dehydrogenases of alive cells that converts the added tetrazolium compound into a water-insoluble formazan crystal(Mosmann, 1983). Eventually, the amount of crystal formation (determined by absorbance spectroscopy) corresponds to the viability of the present cell culture. Fig. shows the cell viability values of all cell lines after 24 h and 48 h, respectively. From the results, we can conclude that ZIF-8 concentrations of different 2-MIM ratios cause only a low reduction of cell viability to approximately 80% compared to the control. Furthermore, the results after 24 and 48 h show no evident variation, suggesting that the incubation time is not a pivotal factor for the reduction in cell viability. ZIF-8 was not cytotoxic at the tested concentration. The reduced cytotoxicity of DOX@ZIF-8 compared to DOX may be explained by the slow release of the drug. It is shown that the complex DOX@ZIF-8 exhibits lower cytotoxicity than pure Doxorubicin for the tested cells, possibly due to the slower release of the incorporated drug.

CHAPTER 3

SYNTHESIS, CHARACTERIZATION, AND INVESTIGATION OF CYTOTOXIC EFFECTS OF SORAFENIB-LOADED ZIF-8 METAL-ORGANIC FRAMEWORKS

3.1. Aim of the Study

The aim of this study is to develop a new generation of intelligent, biocompatible, biodegradable, and multifunctional nanocarrier systems for the treatment of hepatocellular carcinoma cells. Sorafenib was encapsulated into the ZIF-8 smart material to be formed with zinc and 2-methylimidazole. Characterization and drug release studies were done. Cytotoxic activity profiles, effect on cell cycle and apoptosis mechanism were investigated in HUH-7 and HEPG2 cell lines.

3.2. Introduction

3.2.1. Liver Cancer

Liver cancer is a cancer of liver origin and is an aggressive tumor that often occurs in chronic liver disease and cirrhosis. Primary liver cancer, or hepatocellular carcinoma (HCC), is the fifth most common cancer in men and the seventh most common in women and is the third leading cause of cancer-related death worldwide(Ferlay et al., 2010; Jemal et al., 2011). Also, HCC is the most common type of liver cancer and occurs mainly in China, Southeast Asia, and Sub-Saharan Africa(Sagnelli, Macera, Russo, Coppola, & Sagnelli, 2020).

Despite advances in its treatment, liver cancer remains one of the most challenging cancers to treat(J. M. Llovet, Schwartz, & Mazzaferro, 2005). Treatment options for HCC include hepatectomy, image-guided transcatheter tumor therapy, liver transplantation, transcatheter arterial chemoembolization (TACE), radiotherapy, chemotherapy, and

combination therapy(Dimitroulis et al., 2017). However, recurrence of HCC remains a significant problem after curative therapy, reaching an incidence of over 70% at five years(J. M. Llovet et al., 2005).

Even in patients with early, small HCC (<3 cm) who underwent surgery, the 5-year survival rate is unsatisfactory (47% to 53%)(Altekruse, McGlynn, Dickie, & Kleiner, 2012; Fong & Tanabe, 2014; Poon, Fan, Lo, Liu, & Wong, 2002). Typically, HCC is usually diagnosed at an advanced stage, and many patients with advanced-stage are not eligible for curative treatments. Moreover, conventional systemic chemotherapy shows low efficacy and little survival benefit(Verslype et al., 2009). Approval of Sorafenib, a multikinase inhibitor, has shown some survival benefit in patients with advanced HCC and preserved liver function, highlighting a promising molecular-targeted strategy for advanced HCC(J. M. Llovet et al., 2008).

The treatment of liver cancer is now multidisciplinary, and multimodal treatment options are generally selected on an individualized basis based on the complex interplay between tumor stage and extent of underlying liver disease and the patient's overall general health. There are differences in recommendations for the management of liver cancers according to specialties and geographic regions(Fong & Tanabe, 2014).

Currently, conventional antitumor drugs lack selectivity for tumor tissues(Hourdequin, Schpero, McKenna, Piazik, & Larson, 2013; Miyahara et al., 2017; Mochalova & Koroleva, 2013), and the main barriers to chemotherapy are multidrug resistance (MDR) and drug toxicity(X. Dong & Mumper, 2010).

Among solid tumors, HCC is considered a typical drug-resistant tumor, and strategies designed to overcome MDR are urgently needed(Awan et al., 2017; Limeres, Moretton, Bernabeu, Chiappetta, & Cuestas, 2019; Tang et al., 2020). In recent years, advances in medical science and technology have facilitated the development of multiple tumor molecule-targeted therapies, and drugs targeting specific molecules have shown promising efficacy in the treatment of HCC(Choueiri et al., 2010; Harshman et al., 2012). Molecule-targeted drugs are more specific to tumor tissue and more effective than conventional chemotherapy drugs in the treatment of cancer cells(Sowa & Sakai, 2015; H.-T. Wang & Xia, 2019). Sorafenib (SRF) is a dual aryl urea multikinase inhibitor(Kong et al., 2021; Zhu, Zheng, Wang, & Chen, 2017).

3.2.2. Sorafenib

Sorafenib is a multikinase inhibitor, platelet-derived growth factor receptor (PDGFR) that represses the activity of Raf-1 and other tyrosine kinases such as vascular endothelial growth factor receptor 2 (VEGFR-2), VEGFR-3, Fms-like tyrosine kinase 3 (FLT3), and fibroblast growth factor receptor 1 (FGFR-1), is the first targeted therapy approved by FDA for the treatment of advanced HCC in patients with relatively preserved liver function, that prolongs the life of patients between 3 and 4 months (Josep M Llovet & Hernandez-Gea, 2014).

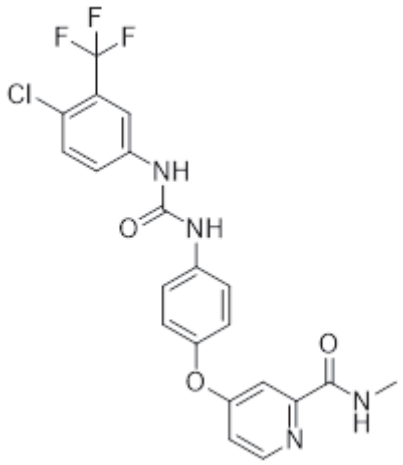

Figure 3.1. Structure of Sorafenib

SRF applies potent antitumor and antiangiogenic effects. It not only directly inhibits tumor cell proliferation by blocking the cell signaling pathway mediated by Raf/MEK/ERK but also indirectly inhibits tumor cell growth by blocking tumor angiogenesis by inhibiting it(R. Pang & Poon, 2006). SRF satisfactorily improves patient survival(Palazzo, Iacovelli, & Cortesi, 2010).

Although SRF is currently widely used, it still has some negative side effects(Josep M Llovet et al., 2008; S. Zhang et al., 2020). For example, non-specific uptake of SRF by normal tissues can lead to a number of adverse effects such as skin rash, diarrhea, high blood pressure, and redness of the palms or soles (A.-L. Cheng et al., 2009; M. Li et al., 2018; Mancuso, Airoldi, Vigano, & Pinzello, 2011). In addition, SRF is poorly water-soluble and is rapidly cleared and metabolized, leading to low absorption efficiency in tumor tissues(Blanchet et al., 2009; Z. Zhang et al., 2014). Moreover, some

patients have an innate resistance to SRF or become resistant after treatment. However, SRF exerts antimetastasis and antiproliferation effects through multiple targets such as EGFR, Raf, and PDGFR; not all HCC tumors overexpress these targets. Some tumors are not dependent on the above pathways during tumorigenesis, and some pathways are selectively downregulated during treatment due to tumor heterogeneity. This indicates that acquired or primary SRF resistance is the main barrier to the survival of patients with liver cancer (Zhu et al., 2017).

3.2.3. Encapsulation of Sorafenib

In order to improve the treatment of Sorafenib, which has limited efficacy, research is directed towards the development of new generation drug platforms and drug delivery systems that will make HCC cells susceptible to Sorafenib. Researchers have developed many new SRF nanocarriers to overcome drug resistance in HCC. Nanoparticles (NPs) for drug delivery applications are typically 5–200 nm in size (Fagin & Wells Jr, 2016; Gleiter, 2000). In recent years, the literature on NPs in the treatment of HCC has increased significantly and has made significant progress in the application of NPs to treat HCC. SRF-loaded NPs (SRF-NPs) have a high release efficacy and bioavailability and actively target tumor tissues(Pellosi et al., 2016; R. Zhao et al., 2017; Z.-B. Zhao et al., 2018). SRF-NPs have a small diameter and large surface area, which increases the resolution of SRF. Furthermore, the properties of SRF-NPs can be controlled to facilitate delivery to target tumor tissue(Gu et al., 2018; Kayser, Lemke, & Hernandez-Trejo, 2005). In addition, the zeta potential and other properties of NPs can be engineered to improve cellular response. For example, a high absolute zeta potential indicating high surface charge density increases cancer cell death and improves the treatment efficacy of SRF-NPs(Patra & Dasgupta, 2012). Moreover, by controlling drug release, NPS effectively reduces the therapeutic dose and frequency of administration. NPS reduces the cytotoxicity and degradation rate of chemotherapy drugs(Gu et al., 2018). Moreover, many drug-loaded NPs are delivered to tumor tissues in vivo using magnetic fields, and drug release can be triggered by acidic tumor environments. SRF-NPS effectively treats cancer by bypassing the physical and physiological barriers that

block conventional drugs. Therefore, nanotechnology has the potential to change the resistance of cancer cells to cancer drugs and overcome MDR(Limeres et al., 2019).

NPS is attractive for medical applications due to its excellent stability, superior structural design, variable and controlled solubility, low immunogenicity, good cellular biocompatibility, antigenicity, three-dimensional geometric structure, and specific tissue/cell targeting abilities(Pasut & Veronese, 2007; Pergal et al., 2012). Modes of action of SRF-NPS include controlled release of amphiphilic drugs, sustained release of therapeutic agents, cyclic dosing, and passive delivery of drugs to tumor tissues via enhanced permeability and retention (EPR) effect. In addition, active targeting of NPs, specifically through binding of cancer tissue ligands to the NP surface, confirms the clinical efficacy of enhanced drugs(M. A. Khan, Raza, Ovais, Sohail, & Ali, 2018; Qilong Wang et al., 2019).

Metabolic kinetics are the main factors affecting the toxicity of NPs in vivo. Some physical and chemical properties of NPs (e.g., size, charge, and surface properties) directly affect their metabolism(Kong et al., 2021). The advent of nanomedicine has made drugs of poor solubility worthwhile. Poorly soluble drugs can be encapsulated, coated, or chemically bound to NPs(Sapavatu, Chinthala, & Jadi, 2020). NPS has also been developed with favorable pharmacokinetics to avoid toxicity and side effects, target the desired site of action, and provide triggered drug release(I. Khan, Joshi, Nakhate, Kumar, & Gupta, 2019). The therapeutic outcome depends on the NP biodistribution affected by the tissue targeting approach. Passive targeting uses disease physiology, whereas active targeting uses specific surface coatings or conjugated ligands(Alavi & Hamidi, 2019; Shreya, Raut, Managuli, Udupa, & Mutalik, 2019). The blood and lymphatic circulation play an essential role in the transport of NPs. Most uncoated NPs are cleared from the circulation by the mononuclear phagocyte system(Kong et al., 2021).

In recent years, researchers have created not only nanoplatforms to improve the biocompatibility of SRF but also nanoplatforms with active targeting capabilities, pH response, and magnetic field response, expanding the application possibilities. These nanoplatforms have improved the resolution, tumor tissue retention, and therapeutic efficacy of SRF in vivo. These results were obtained by methods such as increasing the concentration of SRF entering tumor cells, controlling the release of SRF in time/space, and real-time monitoring of SRF(D.-Y. Gao et al., 2015; Paliwal, Paliwal, & Vyas, 2015; Xiao et al., 2016).

Targeted delivery of SRF-NPS is an effective method to improve treatment efficacy and reduce the toxicity of SRF to non-tumor cells. Tumor targeting mechanisms fall into two categories: passive targeting and active targeting. Passive targeting requires the EPR effect, which causes infiltration of NPS into tumor tissue through abnormal and highly heterogeneous microvasculature and retention due to dysfunctional lymphatic drainage. In contrast, active targeting involves interactions between specific receptors overexpressed on target cells in tumor tissues and targeting modifiers that bind to the surface of SRF-NPs (Swain, Sahu, Beg, & Babu, 2016). It is generally believed that the targeting effect of active strategies is more critical than passive targeting but is also more challenging to modify (Kong et al., 2021).

3.3. Materials and Methods

3.3.1. Synthesis and optimization of ZIF-8 and SRF@ZIF-8 nanoparticles

Synthesis of the small size of ZIF-8 nanoparticles was carried out with the minor modifications to be made in the method of Pan et al. (2011) (Pan et al., 2011). In this study, ZIF-8 was synthesized such that the Zn_{+2}:2-methylimidazole: H2O molar ratio of 1: 70: 1238 was obtained (Kaur et al., 2017). According to these values, $Zn(NO_3)_2.6H_2O$ (585 mg) was dissolved entirely with 4 mL of DI water. On the other side, 2-methylimidazole (2-MeIM) (11.35 g) was dissolved in 40 mL of DI in water, and 6 mL of DMSO solution was added. Then two solutions are mixed together to form a white solution. After the mixture was continued for 5 minutes in room conditions, centrifuging at 14,000 rpm for 15 minutes caused precipitation of the white powders. Unreactants were removed by washing the solution three times with methanol and overnight at 65^{o}C to obtain ZIF-8 nanoparticles.

For the synthesis of SRF@ZIF-8 nanoparticles, the same method described above was applied. In this study, 50 mg of Sorafenib were dissolved in 6 mL of DMSO and added to the dissolved 2-methylimidazole solution and added to the dissolved zinc nitrate solution after stirring for 5 minutes. Other steps were continued as the ZIF-8 synthesis.

3.3.2. Nanoparticle Yield and Encapsulation Efficiency

The yield of the nanoparticles was determined by gravimetry after washing and drying a known volume of nanoparticle suspension. The drug loading and encapsulation efficiency were investigated directly by inductively coupled plasma- optical emission spectrometry (ICP-OES) (Agilent, United States). In ICP-OES analysis, the particles were decomposed in an aqueous solution of 5%HNO3 prior to the measurement, and thus, the Zn compositions of the whole particle material were obtained. The encapsulation efficiency of the active agents was calculated as follows:

Encaps. efficiency (%) = (mass of drug in nanocomposite/mass of total loaded drug) × 100

3.3.3. Characterization of ZIF-8 and SRF@ZIF-8 nanoparticles

The synthesized nanoparticles were characterized by various analytical techniques in terms of properties such as particle charge, size and distribution, surface property, drug loading, and release activities.

The particle size and the zeta potential value are the parameters that must be examined because of the colloidal stability in the structure and the fact that the particle has a significant impact on the cellular retention rate in vitro applications. For this reason, Zetasizer Nano Z (Malvern Panalytical, United Kingdom) using Dynamic Light Scattering Method (DLS) ZIF-8 and SRF@ZIF-8 nanoparticles particle size and zeta potential was determined and examined. In addition, the dimensions of the nanoparticles to be generated by scanning electron microscopy (SEM) was verified. The samples were displayed using the 5 VK electron beam and 200 nm scale using the FEI QUANTA 250 FEG(USA) device. In addition, the images to be obtained by SEM analysis gave information about the structure properties (porosity, layer thickness, morphology) of the nanoparticle. Energy Dispersive X-ray Spectroscopy (EDX) was used to determine the elemental composition of ZIF-8 and SRF@ZIF-8 nanoparticles. X-Ray Diffraction Device (XRD) measurement was determined the crystallinity and impurity of the nanoparticles to be formed. XRD analysis was performed by using the CuKα radiation in the Philips Xarakpert Pro diffractometer (Royal Philips Electronics, Amsterdam, The

Netherlands) with a beam length of 1.541 A and keeping it at 40 kV and 25 mA. With the Fourier Transform Infrared Analysis (FT-IR) (PerkinElmer, USA), the functional groups present in ZIF-8 and ZIF-8 with Sorafenib were examined.

3.3.4. Drug Release Studies

Tumor cells have an acidic pH due to their rapid metabolism and anaerobic respiration. In addition, ZIF-8 has been shown to decompose in the acidic buffer by Sun et al. 38. This encourages current drug release kinetics to control at the pH 5.0 level, which mimics the internal environment of tumor cells; releases the drug. Moreover, release studies were performed at physiological pH 7.4. As a result, drug release kinetics were investigated in PBS at physiological temperature (37°C), pH = 7.4 and 5.0 with continuous shaking (3 mg SRF@ZIF-8 powder material was used in 1 mL). At regular intervals (0 to 120 hours), the centrifugation supernatant is removed and replaced with fresh PBS. PBS samples were collected each time. Absorbance measurement of the supernatants was taken with a UV-Vis spectrophotometer (Shimadzu-UV-2550, Japan). In order to calculate the amount of drug released, the maximum absorbance peak given by the drug was taken as a reference. (for Sorafenib at 265 nm)

3.3.5. Cell Culture

Cells were cultured in a CO_2 incubator set at 37°C in RPMI 1640 or DMEM F/12 medium containing 5% penicillin/streptomycin, 5% L-glutamine, and 5-10% fetal bovine serum. The viability and proliferation of the cells were achieved by passaging the flasks after covering the 80% culture dish. Cells that actively proliferate in the logarithmic phase were used in the experiments.

3.3.6. Cell Viability and Cytotoxicity Test

The survival and growth trends of ZIF-8 and SRF@ZIF-8 nanoparticles on HUH-7 and HEPG2 cells were determined by MTT cell proliferation assay. The MTT test is a colorimetric test based on a sensitive, quantitative and reliable cell culture that measures cell viability, growth, and activation of cells. The test is based on the conversion of the water-soluble yellow 3-(4,5-dimethylthiazol-2-yl)-2,5-diphenyl tetrazolium bromide (MTT) substrate into the water-insoluble purple formazan substrate of the living cells due to the mitochondrial dehydrogenase enzyme capacity. The amount of formazan produced is directly proportional to the number of live cells. The MTT test is a valuable method in determining the cells that are not dividing but still active (Mosmann, 1983), (Freshney et al., 1994). For this purpose, cells at a concentration of 5000 cells/well were seeded into 96-well cell culture dishes. These cells are incubated for 24 hours at 37°C, with 95% humidity and 5% CO2. After 24 hours, cells were incubated at various concentrations of ZIF-8 and SRF@ZIF-8. Samples were sterilized by UV irritation prior to cell culture. After 24, 48, and 72 hours incubation, 5 mg/mL of MTT solution was added, and after incubation at 37°C for 4 hours, formazan crystals were dissolved in DMSO and measured at 570 nm.

3.3.7. Apoptosis Analysis

The apoptotic effects of ZIF-8 and SRF@ZIF-8 nanoparticles on HUH-7 and HEPG2 cells were tested by using Annexin V-FITC Detection Kit. (BioVision,USA). Into 6-well plates, 1980 µL of cell suspension at a density of 5x105 cells per well were inoculated and incubated in a CO_2 incubator at 37°C. After 24 hours, 20 µL of test compounds dissolved in DMSO were added to incubated cells at a final volume of 2 mL and final concentrations of 5, 10, 20 µg/mL. The treated cells were incubated for 24 hours in a CO2 incubator at 37°C. After incubation, cells were harvested by trypsin and centrifuged at 800 rpm for 5 minutes. The pellet was dissolved in 5 mL of PBS and centrifuged again. The pellet was resuspended in 250 µL of binding buffer, one µL of Annexin V-FITC and 2,5 µL of PI were added. The stained cells were incubated for 15

minutes at room temperature. After incubation, the apoptotic effects of test compounds were determined by a flow cytometer (BD FACSCanto, USA).

3.3.8. Cell Cycle Analysis

The effects of ZIF-8 and SRF@ZIF-8 nanoparticles on the cell cycle were tested in HUH-7 and HEPG2 cancer cell lines by propidium iodide staining (BioVision, USA). Into 6-well plates, 1980 µL of cell suspension at a density of 5 x 105 cells per well were inoculated and incubated for 24 hours. Test compounds were dissolved in DMSO and added to incubated cells to maintain the final concentrations of 5, 10, 20, 50, 100 µg/mL. The cells treated with test compounds were incubated for 24 hours in a CO2 incubator at 37 °C.

After incubation, cells were harvested by trypsin and centrifuged at 1200 rpm for 10 minutes. The supernatant was poured, and the pellet was dissolved in 5 mL of PBS. The cell suspension was centrifuged again. The pellet was resuspended in 1 mL cold PBS and fixed by adding 4 mL of -20 °C ethanol (99.8%) (Merck) on a low-speed vortex. The fixed cells were incubated at -20 °C for at least 24 hours. After incubation, the fixed cell suspension was centrifuged at 1200 rpm for 10 minutes at four °C. The pellet was dissolved in 5 mL of PBS and centrifuged again. The pellet was resuspended in a 200 µL phosphate buffer, including 0.1% Triton X-100. 20 µL RNase A (200 µg/mL) was added to the cell suspension, and cells were incubated in a CO2 incubator at 37 °C for 30 minutes. After incubation, 20 µL PI (1 mg/mL) was added, and cells were incubated at room temperature for 15 minutes. The cell cycle distribution was determined by flow cytometer (BD FACSCanto, USA), and data were analyzed by ModFit LT software. For each sample, at least 10,000 events were collected.

3.3.9. Serum protein binding and hemolysis

Fetal bovine serum (FBS): nanocarrier mixtures were prepared at 10:90, 20:80, 40:60 and 60:40 (v/v) ratios with 1000 µL final volume. The mixtures were incubated for two h at 37oC and centrifugated. Pellets were washed with PBS buffer (pH 7.4). Bradford

assay (Bradford, 1976) was used for protein determination in supernatants, then protein-binding amount and yield were calculated.

To determine hemolysis potentials, erythrocytes were mixed with nanoparticles at 1, 5, and 10 µg/mL ZIF-8 and SRF@ZIF-8 (in PBS solution) at 1:1 (v/v) ratio and incubated at 37oC for four h. PBS was used as a negative control group and 1% Triton X-100 as a positive control group. End of incubation, erythrocytes and nanocarriers were separated from the mixture by centrifugation, and hemoglobin was spectrophotometrically determined at the upper layer at 540 nm. Hemolysis ratio calculated via absorbance with the formula below (Mayer et al., 2009; Yallapu et al., 2015).

(% Hemolysis = (A sample - A negative control) * 100/A positive control)

3.4. Results and Discussion

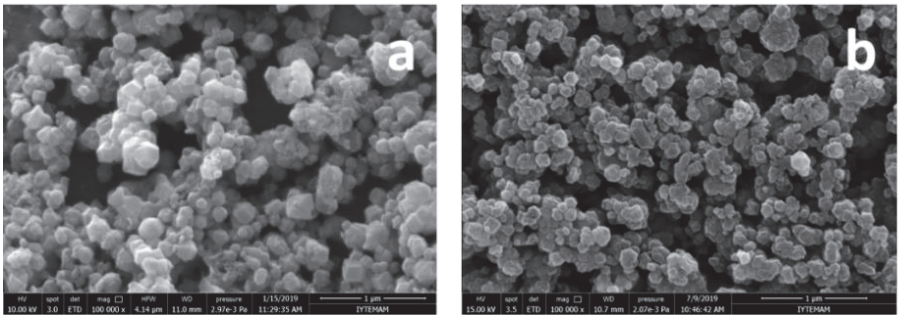

Figure 3.2. SEM micrographs of a)ZIF-8 b)SRF@ZIF-8

The synthesis of ZIF-8 and SRF@ZIF-8 nanoparticles were performed using the one-pot method. Scanning electron microscopy (SEM) showed that the ZIF-8 and SRF@ZIF-8 consisted of isolated crack-free particles of diameter between 113 −140 nm. As shown in Fig 3.2, scanning electron microscopy (SEM) images of the resulting structures indicate the formation of rhombic dodecahedral crystals, which corresponds to the average size of biomedically relevant ZIF-8 encapsulating biomacromolecules, as previously reported by Falcaro and co-workers(Hoop et al., 2018). As expected,energy-

dispersive X-ray (EDX) spectroscopy maps confirm the presence of Zn, C, and N elements uniformly distributed throughout each crystal, whereas; Sorafenib has F, S, and Cl(Chu et al., 2018). The atomic percent distribution of ZIF-8 is in accordance with the $C_8H_{10}N_4Zn$ formula. When the distribution of SRF@ZIF-8 and ZIF-8 nanoparticles are compared, it is observed that the F and Cl elements from SRF are added in the atomic percentage distribution of SRF@ZIF-8, and the percentage of element C increases. These results overlap with the SRF with the formula $C_{21}H_{16}ClF_3N_4O_3$.

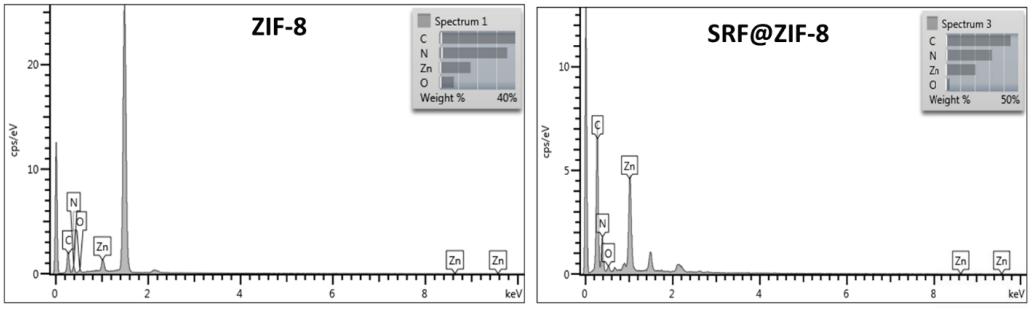

Element	Wt%	Atomic %
C	39.98	50.29
N	35.72	38.53
O	7.80	7.37
Zn	16.50	3.81
Total:	100.00	100.00

Element	Wt%	Atomic %
C	44.80	57.48
N	31.88	35.08
O	2.67	2.58
Zn	20.64	4.87
Total:	100.00	100.00

Figure 3.3. EDX Analysis of a)ZIF-8 b)SRF@ZIF-8

Comparison of the sample XRD pattern to the pattern simulated from the published ZIF-8 structure data indicates that the product is pure-phase ZIF-8 material. Peak broadening can be clearly observed from the sample XRD pattern, indicating the formation of nanosized crystals. Each synthesis yielded pure-phase ZIF-8 crystals, as demonstrated by X-ray diffraction (XRD) patterns (Fig 3.4). Patterns generated by the ordered porous structure of the ZIF-8 particles between 2θ values of 5 and 40° can be observed, and the peak broadening observed indicates the formation of nanosized crystals. The relative intensities and the sharp peaks in the diffraction pattern of ZIF-8 at 2θ=7.11°, 12.5°, 17.75°, and 26.4° prominent peak positions, including 011, 002, 112, 022, 013, and 222, are in good agreement with previous reports,(Cravillon et al., 2009; Park, Ni, Côté, Choi, Huang, Uribe-Romo, Chae, O'Keeffe, et al., 2006) confirming the sodalite structure, which is the typical structure of ZIF-8, and the well-defined peaks revealed high crystallinity.

The XRD shows the exact crystal structure of ZIF-8 NPs, showing that the addition of SRF did not alter the structure of ZIF-8. XRD analysis of the complex shows unchanged lattice parameters for ZIF-8 previous to and after SRF loading.

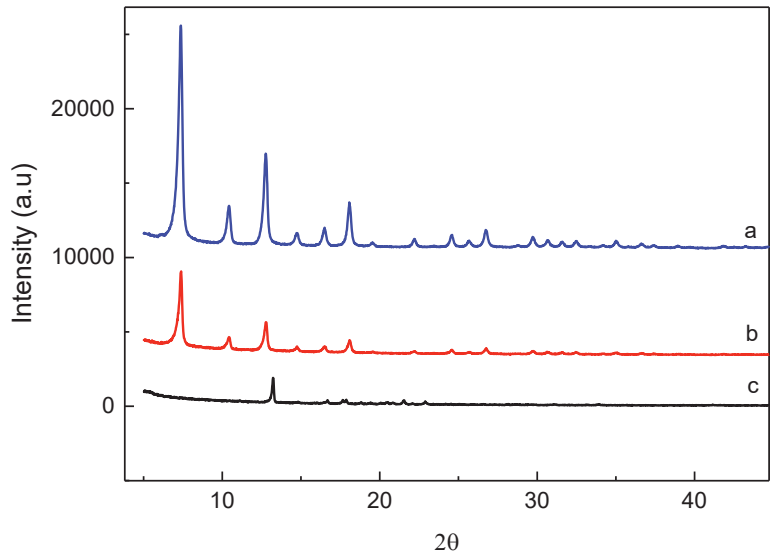

Figure 3.4. XRD patterns of a)ZIF-8, b)SRF@ZIF-8 and c)SRF

The zeta potential of nanoparticles is an essential factor for cellular retention rate *in vitro* applications. The particles must have surface charges to prepare a reasonable dispersion without agglomeration in any colloidal structure, and understanding the surface charges is therefore critical for deciding the adsorption of these particles to a surface or their affinity to the targeted site. The zeta potential is a crucial indicator of the stability of colloidal dispersions. The colloids with high zeta potential (negative or positive) are electrically stabilized, while colloids with low zeta potentials tend to coagulate or flocculate. Therefore, zeta potential and hydrodynamic radii of ZIF-8 and SRF @ ZIF-8 nanoparticles synthesized were investigated by DLS measurement. The zeta potentials of the nanoparticles were measured as -21,3 and 17.8 mV, respectively. This change in zeta potential can be attributed to the encapsulation of the drug. The difference of zeta potential further provided evidence to the success of nanocrystals synthesis. Also, indicating SRF@ZIF-8 has better stability (the more excellent value, the more stable) and is not easy to polymerize in solution. In addition, this change of electronegativity will enhance cellular uptake. The hydrodynamic radius of the ZIF-8

nanoparticles was approximately two times larger than the values in the SEM measurement. The results found as a result of the measurement are shown in Table 3.

To synthesize nanoparticles that can be encapsulated in small size with high loading, high efficiency, and high encapsulation efficiency of Sorafenib is essential for drug delivery applications. ICP-OES was used to determine the adequate SRF loading capacity. In the ICP-OES analysis, nanoparticles were degraded in 5% HNO_3 solution before measurement, and thus the amount of Zn in the nanoparticle was obtained. Based on the Zn amount obtained, the ZIF-8 yield was calculated. The amount of SRF in ZIF-8 using the gravimetrically determined ZIF-8 and SRF@ZIF-8 quantities is shown in Table 3.

Table 3. Yield, Hydrodynamic radius, Drug loading capacity, and zeta potentials of a)ZIF-8 and b)SRF@ZIF-8

	Yield (%)	**Hydrodynamic radius (nm)**	**Drug Loading Capacity (%)**	**Zeta Potential (mV)**
ZIF-8	**68,3**	**340**		**-21,3**
SRF@ZIF-8	**53,8**	**809**	**58**	**17,8**

FTIR spectra were obtained for ZIF-8, SRF, SRF@ZIF-8. In the spectrum corresponding to ZIF-8, two bands at 3135 and 2928 cm^{-1} can be observed for the aromatic C–H stretch and the aliphatic C–H stretch of the imidazole, respectively. The 1606 cm^{-1} band is for the C–C stretch, and the peak at 1580 cm^{-1} is for the C–N stretch. The C–N absorption bands are found in the 1100–1400 cm^{-1} region. The absorption band at 421 cm^{-1} is associated with the Zn–N stretching mode. These assignments are in agreement with the FTIR measurements from Park et al.(Park, Ni, Côté, Choi, Huang, Uribe-Romo, Chae, O'Keeffe, et al., 2006). Several bands are observed for SRF@ZIF-8. The FTIR spectrum analysis for the system SRF@ZIF-8 does not undoubtedly show the adsorption of drugs into ZIF-8, but the detection of characteristic bands for both ZIF-8 and drugs indicates the presence of both compounds.

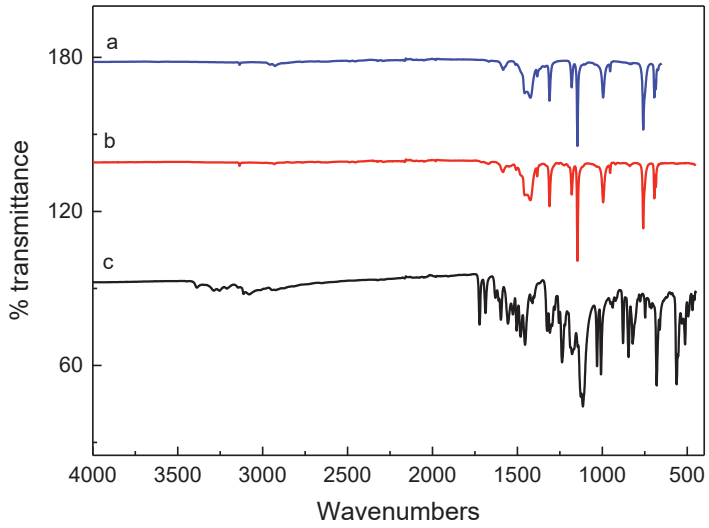

Figure 3.5. FTIR spectra for a) ZIF-8 b) SRF@ZIF-8 and c) SRF

Metal-organic frameworks are organic coordination compounds with high porosity. The surface areas of these materials are quite large. Therefore, the N_2 adsorption/desorption slopes of the ZIF-8 nanoparticles were deduced (Fig 3.6.). The curve obtained corresponds to the Type I isotherm. Thanks to this measurement, it is calculated that the nanoparticles have 1017.3249 m²/g and 1495.7186 m²/g BET and Langmuir surface areas. The surface area results were found to correspond to those known in the literature.

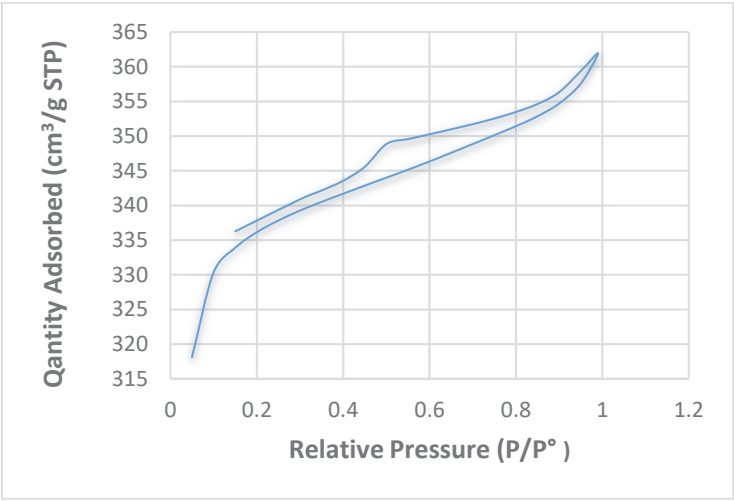

Figure 3.6. N_2 adsorption / desorption slope of ZIF-8

In order to observe the change of drug release from SRF@ZIF-8 nanoparticles over time, pH 5 solution mimicking acidic cancer cell environment and PBS buffer solutions with normal cell pH of 7.4 were created. SRF@ZIF-8 nanoparticles were incubated in these two different pH environments at 150 rpm for five days. Absorbance values of supernatants were measured with a UV-Vis spectrophotometer to calculate the amount of drug released in a specific time period. The cumulative emission graph obtained at pH 5 and 7.4 is in Fig 3.7.

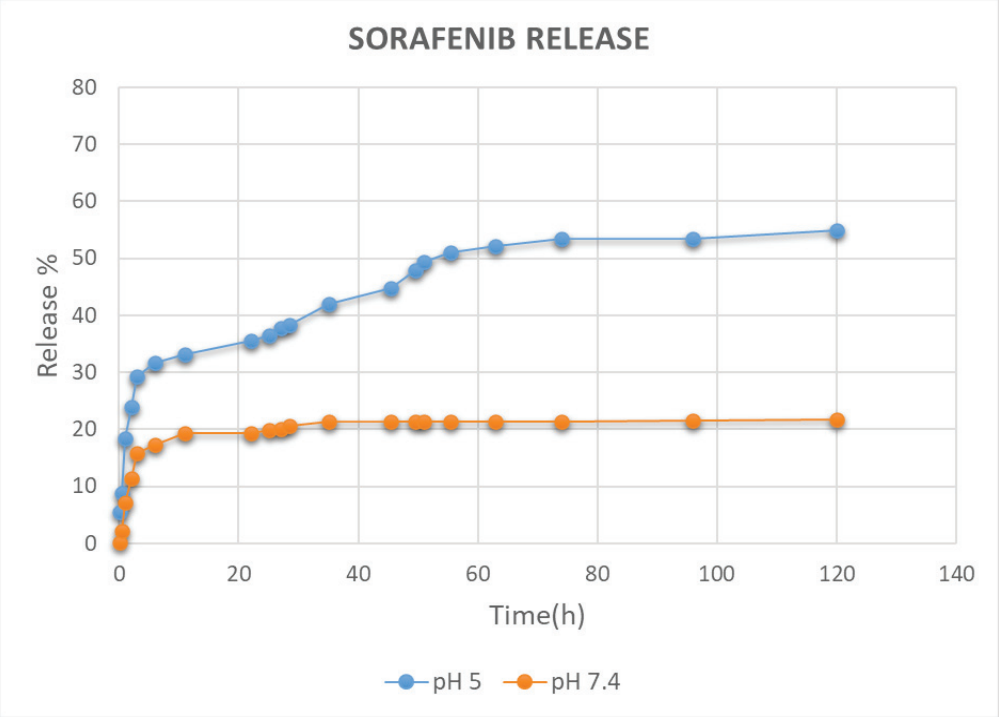

Figure 3.7. The drug release profile of SRF from ZIF-8

Erythrocytes, also known as red blood cells, constitute 48% of blood. The erythrocytes-MOFs interaction is essential to study the hemoglobin release(known as hemolysis). The percentage of erythrocyte cells in the blood of ZIF-8 and SRF@ZIF-8 nanoparticles were investigated. It is known that increased concentration of nanoparticles and especially positive surface charged nanoparticles undergo more hemolysis by erythrocytes in blood than negatively charged ones(Ferdous & Nemmar, 2020). The hemolysis rate of ZIF-8, SRF@ZIF-8 nanoparticles on erythrocytes was investigated in three different concentrations: 1 µg/mL, 5 µg/mL and 10 µg/mL. The hemolysis rate of

ZIF-8 and SRF@ZIF-8 nanoparticles was found to be consistent with each other as 0.53% and 0.42%, respectively (Fig 3.8.). These values are below 5%, which supports the biocompatibility of nanoparticles.

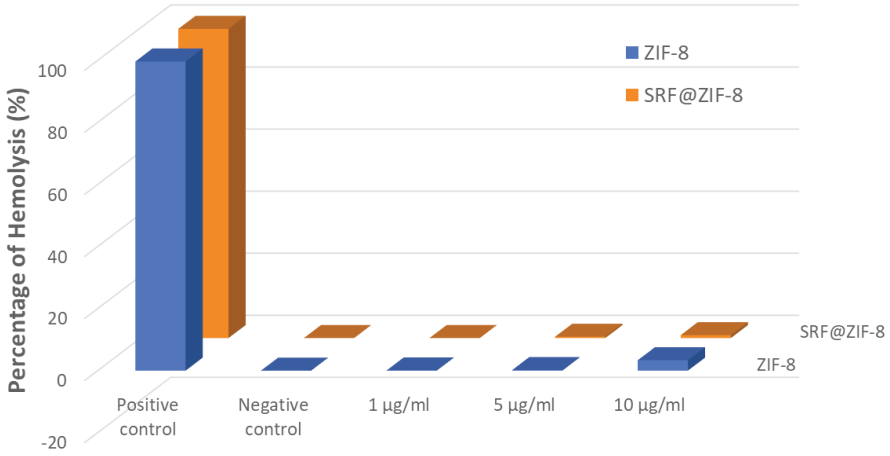

Figure 3.8. Hemolysis rates of ZIF-8 and SRF@ZIF-8 nanoparticles

Cytotoxicity of ZIF-8 and SRF@ZIF-8 crystals was evaluated by a colorimetric MTT test. Cell viability of various nanoparticle concentrations (25-250 µg mL^{-1}) at 24, 48, and 72 hours in HEPG2 and HUH7 cell lines was examined using the MTT assay. MTT test is based on the conversion of tetrazolium salt in MTT compound into formazan salt as a result of mitochondrial enzyme activity in living cells. The intensity of the purple-colored solution formed depending on the cell viability varied. The intensity of the purple color formed was read at 570 nm with the aid of a spectrophotometer in the visible region.

Fig 3.9 shows the cell viability values in HEPG2 and HUH7 cell lines at 24, 48, and 72 hours, respectively. It is known by the literature that an amount less than 30 µg/mL of ZIF-8 does not have a cytotoxic effect on cells. When the results obtained are examined, nearly 100% of the cells preserved their viability at 25 µg/mL ZIF-8, and these results are consistent with the literature. While 250 µg/mL ZIF-8 showed approximately 60% viability on both cell lines, it was observed that it was not cytotoxic at lower concentrations. As a result of the MTT test, it is shown that SRF@ZIF-8 nanoparticles create a significant cytotoxic effect on HEPG2 and HUH7 cells compared to ZIF-8. Cell

death by SRF@ZIF-8 was found to be more effective in the HEPG2 cell line than HUH7 cells.

While SRF@ZIF-8 nanoparticles in HEPG2 cells decreased by 40% at a dose of 250 μg/mL and at the end of 24 hours, in HUH7 cells, this ratio decreased by 20%. In both cell lines, cell viability showed an inversely proportional effect due to the increased dose of SRF@ZIF-8 nanoparticles. Along with the increase in incubation time, it was observed that SRF@ZIF-8 nanoparticles also increased cellular inhibition. HUH7, on the other hand, demonstrated an instant cell viability reduction towards 60-65% for each concentration while gradually increasing overdosage amount and exposure time. Besides, in 72 hours for HUH7 cells, exposure to 250 μg/mL of ZIF-8 presented an approximately half cell viability reduction.

Against SRF@ZIF exposure HEPG2 and HUH7 displayed different reactions. HEPG2 influenced much more quickly and more severely (to 10-25%) against higher doses 100 and 250 μg/mL. At the same time, they were tolerating lower concentrations around 65-80 % of cellular viability. Conversely, HUH7 is visibly affected by each concentration inversely, and this detrimental effect is grown overexposure duration for each dosage. HUH7 cell line viability gradually decreased from 40-60% to 15-55 and eventually hit lowest at 5-25 %.

High cytotoxic effects were observed in Sorafenib at HUH7 and HEPG2 cell lines. The low cytotoxicity of SRF@ZIF-8 compared to SRF on cell death can be explained by the slow release of the drug.

Nanoparticles are taken by active transport into the cytoplasm and other cell organelles through endocytosis. This may cause the formation of nanoparticle agglomerates inside the cell. The interaction between metal-containing nanoparticle aggregates and living cells leads to cell death. This is more clearly observed with morphological changes, incubation time, and an increase in nanoparticle concentration.

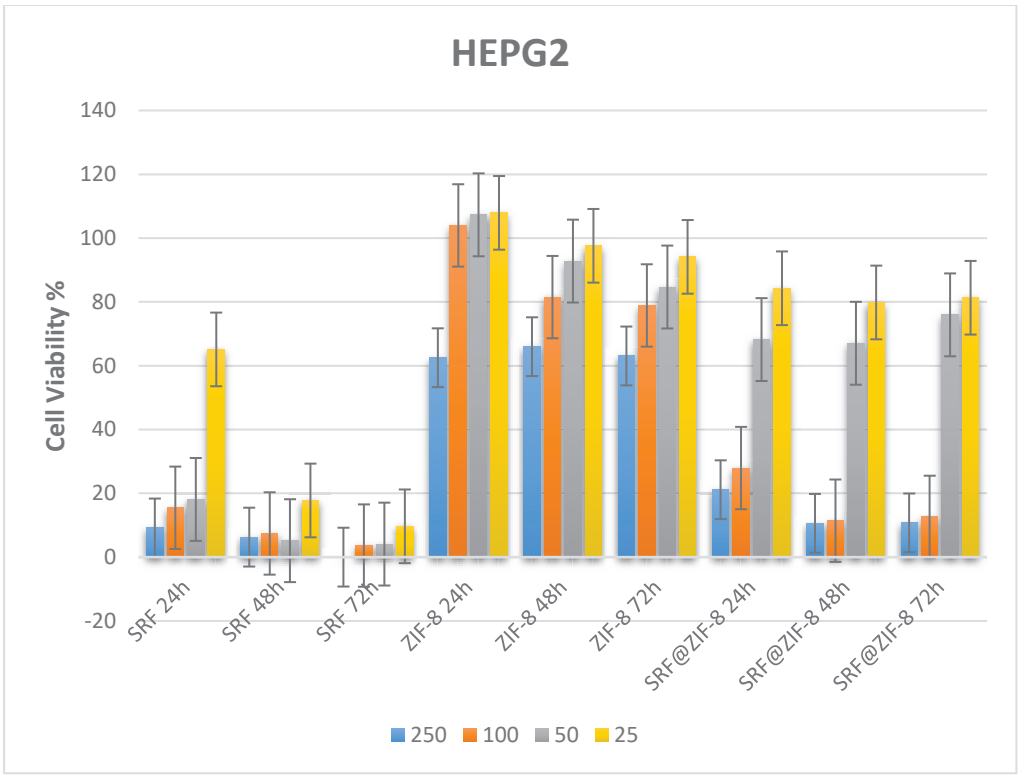

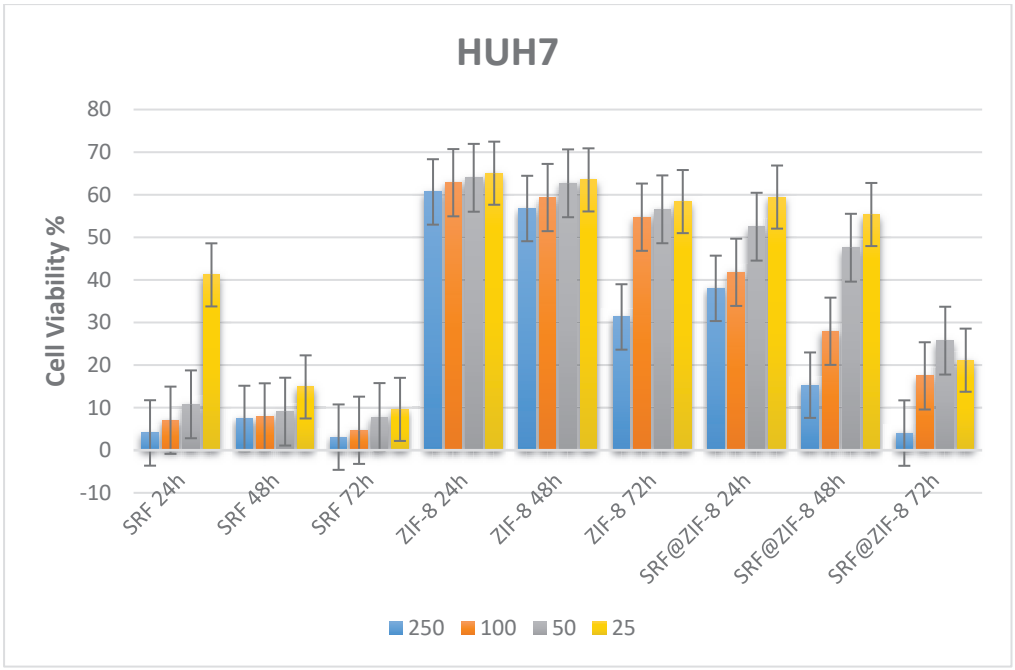

Figure 3.9. Cytotoxic activity profiles of SRF, ZIF-8, and SRF@ZIF-8 in HEPG2 and HUH7 cell lines at 24, 48, and 72 hours.

When the HEPG2 cell line was examined in a 24-hour period, when the values of 20 µg/mL Sorafenib and 100 µg/mL SRF@ZIF-8 were compared, it was observed that the apoptosis rate increased from 68.0% to 91.5%, while the rate of necrosis decreased from 30.5% to 8.0%. When the HUH7 cell line was examined in a 24-hour period, when the 50 µg/mL Sorafenib and 100 µg/mL SRF@ZIF-8 values were compared, it was observed that the apoptosis rate increased from 80.1% to 93.9%, while the necrosis rate decreased from 19.3% to 4.8% (Fig 3.10). As expected, the rate of apoptosis was increased, and the desired reduction in the rate of necrosis was achieved. In addition, when the viability rates in the cell are examined, it has been shown that the decrease in the survival rate in the SRF@ZIF-8 complex is compatible with the results of apoptosis. In addition, when evaluated in terms of the effects of ZIF-8 concentration on cell viability, apoptosis results were observed to be consistent with MTT results.

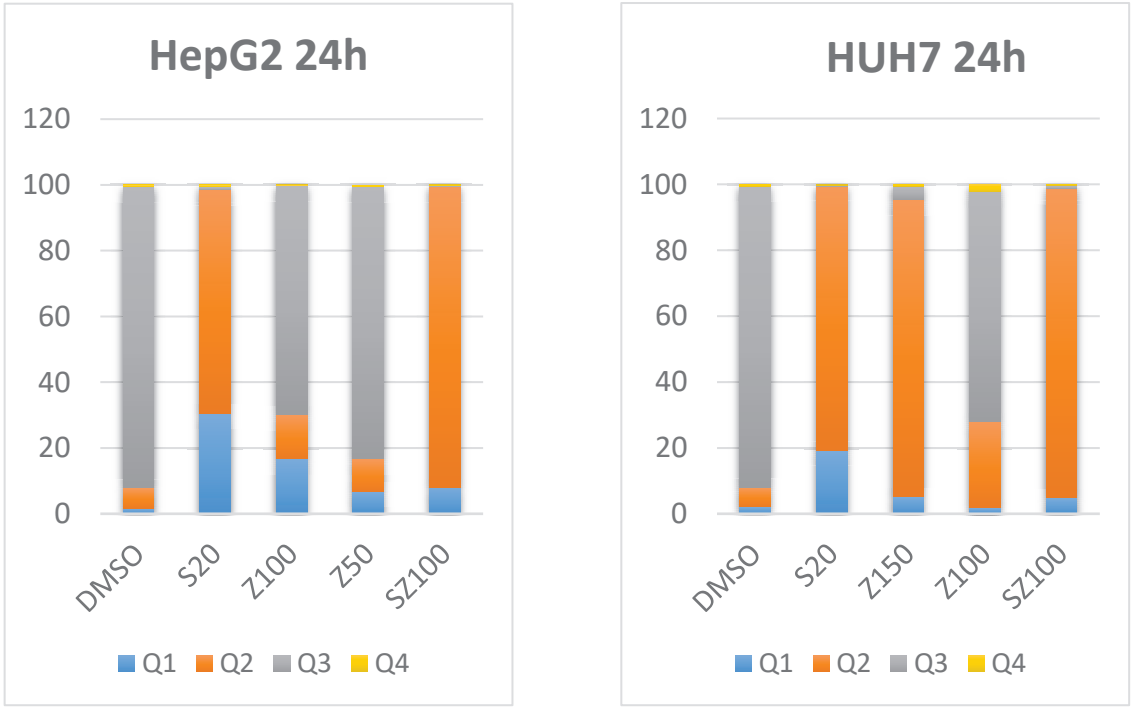

Figure 3.10. Apoptosis analysis of SRF, ZIF-8, and SRF@ZIF-8 at 24 hours in HEPG2 and HUH7 cell lines (necrosis (Q1), late apoptosis (Q2), viability (Q3), and early apoptosis (Q4) rates)

According to the literature, Sorafenib is known to downregulate Cyclin D1 and Cyclin D3 & CDK4 proteins. It is also known that the aforementioned proteins are involved in passing the G1 phase, which is one of the cell cycle control phases. When the graphs are examined comparatively, the findings showing that the highest amount of HEPG2 and HUH7 cells were found in the G1 phase (Figure 3.11) are consistent with the literature.

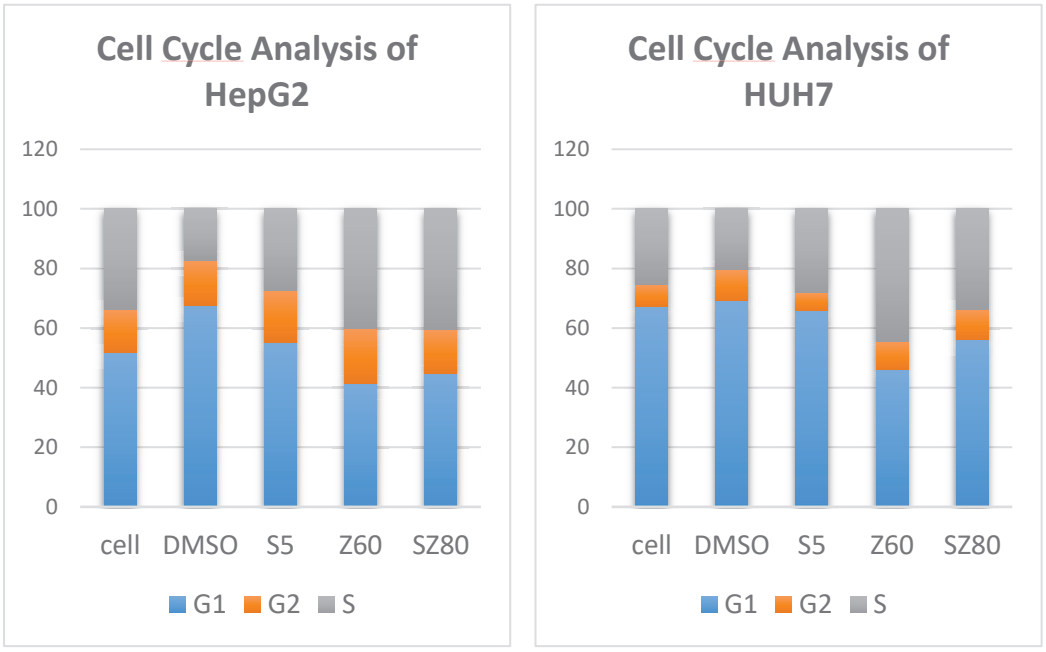

Figure 3.11. The cell cycle analysis for SRF, ZIF-8, and SRF@ZIF-8 at 24 hours in HEPG2 and HUH7 cell lines

When the confocal microscope image results of Sorafenib and SRF@ZIF-8 were examined, accumulation around this region, including the cell nucleus, was observed with DAPI staining. The organelles of the nucleus, nucleus membrane, and endoplasmic reticulum are closest to these regions. Sorafenib is known to cause stress in the ER, in the literature. The nucleus, nuclear membrane endoplasmic reticulum, and the Golgi device form the endomembrane complex and function together. The accumulation of Sorafenib in the specified regions is known to be associated with the kinase inhibition activity stated in the literature. Sorafenib, known as a multikinase inhibitor, is thought to cause stress by affecting the organelles that cooperate with ER and ER and disrupt their work since its activity takes place in these regions.

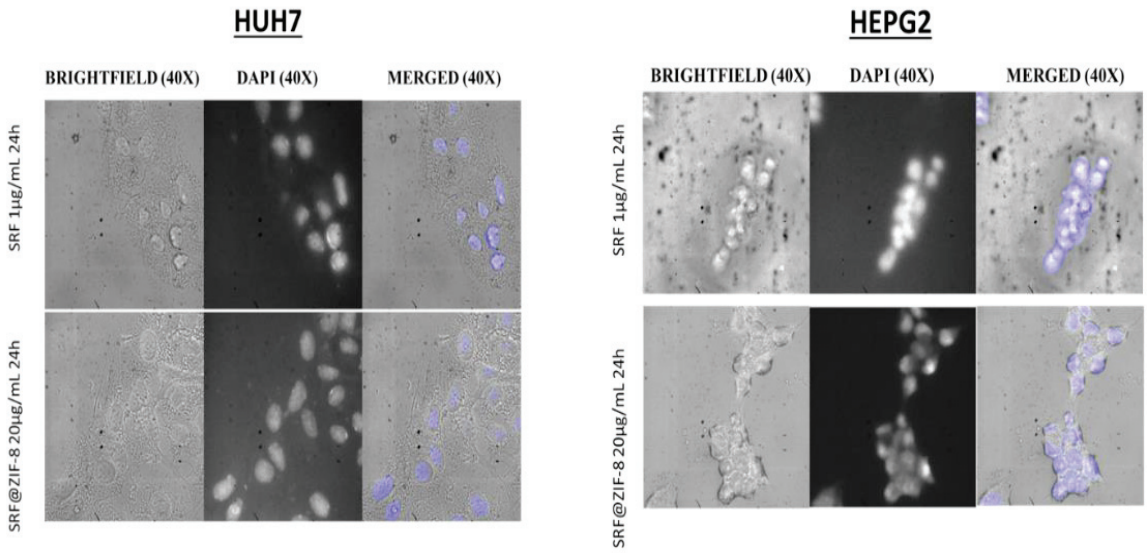

Figure 3.12. Confocal images of SRF and SRF@ZIF-8 at 24 hours in HEPG2 and HUH7 cell lines

CHAPTER 4

METALLO-ENCAPSULATION OF APALUTAMIDE FOR PROSTATE CANCER TREATMENT; INVESTIGATION OF IN VITRO, IN VIVO AND EX VIVO EFFICACIES

4.1. Aim of the Study

The purpose of this chapter is to develop a new generation of intelligent, biocompatible, biodegradable, and multifunctional nanocarrier systems for the treatment of prostate cancer. It is aimed to create dual cytotoxic effects on cancer cells by combining the effects of zinc-apalutamide on a single platform. Apalutamide, which received FDA approval in 2018 for non-metastatic castration-resistant prostate cancer (CRPC), was encapsulated into the ZIF-8 smart material to be formed with zinc and 2-methylimidazole. After characterization and drug release studies cytotoxic activities, cell cycle and Apoptotic effects ROS Luciferase activity Western Blot analysis of ZIF-8 and APA@ZIF-8 were investigated.

4.2. Introduction

4.2.1. Prostate Cancer

When we look at cancer types in more detail, prostate cancer is the most common internal organ cancer in men and ranks second in cancer-related deaths(Siegel, Miller, & Jemal, 2017). According to the 2016 statistics of the World Health Organization (WHO) database, with approximately 1.1 million new cases added each year, 300,000 people die annually due to this disease. According to the results of the Turkey Unified Database, prostate cancer in the male population was the second most common malignancy in our country between 2006 and 2010, and the age-standardized incidence rate was 27.9-33.8/hundred thousand people (Ekin & Zorlu, 2013). Prostate cancer can be quite

insidious and usually does not show symptoms until advanced stages. The elevation makes the first diagnosis of this type of cancer of PSA (prostate-specific antigen) in the blood and/or rectal examination. Patients with suspected prostate cancer are then diagnosed with the disease by applying multiparametric magnetic resonance imaging. The treatment of the disease is with hormonal therapy, chemotherapy, radiotherapy, and/or surgical treatment, depending on the person and staging.

In general, the first preferred method is androgen deprivation (lowering) treatments with hormone therapy. What is desired with this hormone therapy is to reduce the androgen hormone, which is thought to cause prostate cancer, to a negligible amount and stop cancer growth. After being produced in the adrenal gland and testes, androgens (male hormones) enter the cell and bind to androgen receptors in the cytosol, and the continuity of the prostate gland is realized through this androgen signaling pathway(Massie et al., 2011; Shafi, Yen, & Weigel, 2013). Early in its development, prostate cancer growth occurs in the presence of high levels of androgens (Scardino, 1989). Thus, prostate cancer is referred to as androgen-dependent or androgen-sensitive because treatments that reduce androgen levels (hormone therapy (chemical castration) or Orchiectomy (surgical castration)) prevent cancer from growing. Prostate cancer drugs used in the clinic today target androgen synthesis and the androgen receptor. These drugs are part of androgen deprivation treatments. After androgen-lowering treatments, androgen level and androgen receptor activity in the blood decrease, and cancer is stopped by preventing uncontrolled proliferation. Although some patients respond to this treatment after a period of application, most patients become resistant to low androgen levels over time, and the disease relapses (recurs). This condition is called castration-resistant prostate cancer. Even if there are not enough androgens to stimulate the androgen receptor externally, the intracellular androgen signaling pathway is active, and cancer grows. Factors such as mutations in the androgen receptor, androgen receptor gene variants, low androgen sensitivity are influential in activating this pathway(Devlin & Mudryj, 2009; Schröder, 2008). Recently, it has been determined that androgen receptor variants lead to resistance to prostate cancer drugs(Zhiyong Guo et al., 2009; S. Sun et al., 2010). Antiandrogen drugs have been developed. In treating this type of prostate cancer, antiandrogens can be given to patients undergoing hormone therapy or Orchiectomy, and cancer growth can be controlled by combined androgen blockade.

4.2.2. Apalutamide

Apalutamide (other index names; ARN-509, Erleada, JNJ-56021927) is a promising new generation drug acting as an androgen inhibitor, which received FDA approval in 2018 for non-metastatic castration-resistant prostate cancer (CRPC) (Tarapchak 2018). Apalutamide (4-[7-[6-cyano-5-(trifluoromethyl)pyridin-3-yl]-8-oxo-6-sulfanyli-dene-5,7-diazaspiro[3.4]octan-5-yl]-2 -fluoro-N-methylbenzamide) directly binds to the ligand-binding site of AR, blocking the effects of androgens and causing inhibition of AR nuclear translocation, binding of DNA, and inhibition of AR-mediated transcription(Al-Salama, 2018). Apalutamide has several advantages over other androgen inhibitors(X. Pang, Wang, & Chen, 2017; Rathkopf et al., 2017). Koukourakis et al. showed that Apalutamide was more effective on cell proliferation by blocking the AR pathway better than Bicalutamide under normoxia and hypoxia conditions(Koukourakis et al., 2018). In another study, it was reported that although Apalutamide and Bicalutamide bind to the same ligand binding site, Apalutamide is more effective by binding to the AR receptor with a seven to ten-fold higher affinity(Clegg et al., 2012). The in vivo efficacy of apalutamide was evaluated using castrate immunodeficient mice harboring LNCaP/AR xenograft tumors. In this study, 10% of Bicalutamide-treated mice showed 50% tumor regression, while 80% of Apalutamide-treated mice showed 50% tumor regression(Clegg et al., 2012) (Clegg et al., 2012). Pang et al. reported that although Apalutamide has similar in vitro activity to Enzatulamide, it shows a higher in vivo activity in castration-resistant prostate cancer (CRPC) xenograft models(X. Pang et al., 2017). Clinical studies have shown that Apalutamide is as effective as Enzatulamide, which is currently used to treat prostate cancer and exhibits similar side effects(Wallis et al., 2018).

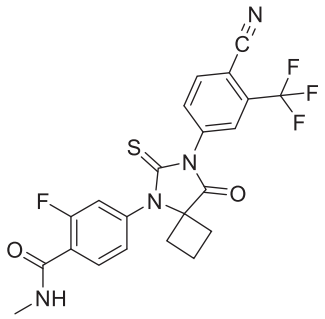

Figure 4.1. Structure of Apalutamide

However, the hydrophobic structure of Apalutamide, low solubility, and stability decreased effectiveness without going to the prostate, high side effects, and expensiveness limits the applications of this drug in treatment. In order to eliminate these similar problems, which can also be seen in other chemotherapy drugs, nano-drug carrier systems are being developed today, and by using these systems, lower doses of the drug can be used. Less damage to healthy tissues can be achieved. There is an increasing interest in developing active substance-loaded nanocarrier systems that are therapeutic, provide controlled release, are biocompatible, non-toxic, and non-carcinogenic, increase the stability of the molecules they carry in the system, dissolve in biological systems, and can be targeted to the desired region.

4.2.3. Zinc-Prostate

Zinc has been described as the ‘calcium of the twenty-first century’(Su et al., 2019). Zinc-based degradable biomaterials have recently emerged thanks to their intrinsic physiological relevance, biocompatibility, biodegradability, and pro-regeneration properties. Zinc-based biomaterials mainly include metallic zinc alloys, zinc ceramic nanomaterials, and zinc metal-organic frameworks (MOFs). Metallic zinc implants degrade at a desirable rate, matching local tissues' healing pace and stimulating the remodeling and formation of new tissues. Zinc ceramic nanomaterials are also beneficial for tissue engineering and therapy thanks to their nanostructures and antibacterial properties(Su et al., 2019). MOFs have large surface areas and are easily functionalized, making them ideal for drug delivery and cancer therapy. Zinc and prostate have an interesting relationship(Costello & Franklin, 2012).

Deficiency or excess of this element has been accepted as a risk factor for prostate cancer. Epidemiological studies to date have produced mixed results regarding the efficacy of zinc supplementation against prostate cancer. Case-control studies have been conducted to reduce the risk of prostate cancer with the use of individual zinc supplements. It has been observed that 15 mg of zinc per day reduces the risk of prostate cancer by 57% compared to those who do not use it(Leitzmann et al., 2003). Other studies have shown that long-term and/or high-dose zinc supplementation may increase the risk of prostate cancer(Gonzalez, Peters, Lampe, & White, 2009). It is thought that exceeding

100 mg/day in zinc intake may cause adverse health reactions and increase the risk of cancer(Leitzmann et al., 2003). Zinc element is an essential factor in healthy prostate tissue and the cancerous stage of this tissue. Intracellular zinc in healthy prostate tissue is 5-10 times higher than in other tissues. Only 5% of zinc is found in the inactive cytoplasm form in other tissues, while this amount is 30% for prostate tissue(P. Feng et al., 2000). This increase in the amount of zinc suggests that this element has particular importance for prostate tissue. It has been emphasized that sufficient zinc concentration in the prostate tissue is vital to the prostate. It has been predicted that zinc acts as a potent tumor suppressor and is necessary for keeping the prostate healthy(Liang et al., 1999; Prasad et al., 2010). A study demonstrated the necessity of low intracellular zinc for prostate cancer metastasis by zinc measurements made in and around the tumor lesion(Costello & Franklin, 2017). As a result of the studies carried out based on this, it was revealed that zinc is essential in the protection of the p53 gene associated with apoptosis, and the high amount of zinc in the mitochondria inhibits citrate oxidation and m-aconitase activity, thus triggering reactions that can lead the cell to controlled mitochondrial death(P. Feng et al., 2000). These functions of zinc in healthy tissues have led to the investigation of zinc for prostate cancer. Clinical studies have shown that prostate cancer cells, unlike healthy prostate tissues, lose their ability to accumulate intracellular zinc. It has been concluded that there is a 65% reduction in intracellular zinc in prostate cancer patients(Costello & Franklin, 2006; Zaichick, Sviridova, & Zaichick, 1997). This reduction has been found to increase even more, especially when prostate cancer is resistant to castration(Shiina, Igawa, & Ishibe, 1996). A decrease in the amount of zinc in prostate cancer tissues has been associated with the decrease (downregulation) of ZIP-1 transport proteins, which are thought to be responsible for the uptake of zinc into the cell, which is necessary for the normal functioning of the prostate(Costello & Franklin, 2017). In in vitro and in vivo studies with the idea that zinc may have a therapeutic effect, it has been observed that mobile zinc ion has a cytotoxic effect on prostate cancer and prevents invasion(Costello & Franklin, 2006, 2012).

Considering that AR functions as an essential effector in prostate cancer development and continues to function in castration-resistant prostate cancer, the need to develop zinc-based cancer therapeutics for prostate cancer emerges. In a study on human prostate cancer cells, it was observed that zinc chloride (15-150 μM) suppressed androgen-responsive proliferation and significantly inhibited androgen-mediated transactivation, expression of many androgen-targeting proteins, including PSA and

p21(Phuong Kim To et al., 2017). Zinc has also been shown to downregulate AR protein levels in cancer cells(Phuong Kim To et al., 2017). Another study reported that zinc modulates insulin-like growth factors (ICG) and signaling molecules, reducing the survival of androgen-independent prostate cancer cells (Banudevi et al., 2010). In addition, zinc has been shown to inhibit the oncogenic NF-κB pathway, sensitizing cells to cytotoxic agents. The downregulation of AR protein levels observed is due to facilitated protein degradation rather than transcription control(Uzzo et al.). These results also reveal that intracellular zinc inhibits cancer cell growth by decreasing AR levels to inhibit the growth of prostate cancer. In vivo studies have also reported that zinc significantly reduces prostate tumor size and has low AR protein levels in tumor cells(Phuong Kim To et al., 2017). All these studies have shown that mobile and free zinc for prostate cancer can be used to treat this type of cancer and has led to the search for an agent that will provide mobile and free zinc to prostate cancer(Banudevi et al., 2010; Costello & Franklin, 2017; Phuong Kim To et al., 2017). There is a need to develop new formulations for prostate cancer, including zinc, such as commercially available anticancer metallo-drugs such as cisplatin, carboplatin, and oxaliplatin. It is believed that zinc ions and therapy can take the quality of treatment one step further, targeting androgen suppression and androgen receptor inhibition, which is the current treatment method.

4.3. Materials and Methods

4.3.1. Synthesis and optimization of ZIF-8 and APA@ZIF-8 nanoparticles

Synthesis of small size of ZIF-8 nanoparticles was carried out with the small modifications to be made in the method of Pan et al. (2011)(Pan et al., 2011). In this study, ZIF-8 was synthesized such that the Zn^{+2}:2-methylimidazole: H_2O molar ratio of 1: 70: 1238 was obtained(Kaur et al., 2017). According to these values, $Zn(NO_3)_2.6H_2O$ (585 mg) was dissolved entirely with 4 mL of DI water. On the other side, 2-methylimidazole (2-MeIM) (11.35 g) was dissolved in 40 mL of DI in water, and 6 mL of DMSO solution was added. Then two solutions are mixed to form a white solution. After the mixture was continued for 5 minutes in room conditions, centrifuging at 14,000

rpm for 15 minutes caused precipitation of the white powders. Unreactants were removed by washing the solution three times with methanol and overnight at 65 oC to obtain ZIF-8 nanoparticles.

For the synthesis of APA@ZIF-8 nanoparticles, the same method described above was applied. In this study, 60 mg of apalutamide was dissolved in 6 mL of DMSO and added to the dissolved 2-methylimidazole solution, and added to the dissolved zinc nitrate solution after stirring for 5 minutes. Other steps were continued as the ZIF-8 synthesis.

4.3.2. Nanoparticle Yield and Encapsulation Efficiency

The yield of the nanoparticles was determined by gravimetry after washing and drying a known volume of nanoparticle suspension. The drug loading and encapsulation efficiency were investigated directly by inductively coupled plasma- optical emission spectrometry (ICP-OES)(Agilent, United States). In ICP-OES analysis, the particles were decomposed in an aqueous solution of 5%HNO3 prior to the measurement, and thus, the Zn compositions of the whole particle material were obtained. The encapsulation efficiency of the active agents was calculated as follows:

Encaps. efficiency (%) = (mass of drug in nanocomposite/mass of total loaded drug) × 100

4.3.3. Characterization of ZIF-8 and apalutamide@ZIF-8 nanoparticles

Various analytical techniques characterized the synthesized nanoparticles in terms of particle charge, size and distribution, surface property, drug loading, and release activities.

The particle size and the zeta potential value are the parameters that must be examined because of the colloidal stability in the structure and the fact that the particle has a significant impact on the cellular retention rate in vitro applications. For this reason, Zetasizer Nano Z (Malvern Panalytical, United Kingdom) using Dynamic Light Scattering Method (DLS) and ZIF-8 and APA@ZIF-8 nanoparticles particle size and zeta potential was determined and examined. In addition, the dimensions of the nanoparticles

to be generated by scanning electron microscopy (SEM) was verified. The samples were displayed using the 5 VK electron beam and 200 nm scale using the FEI QUANTA 250 FEG(USA) device. In addition, the images to be obtained by SEM analysis gave information about the structure properties (porosity, layer thickness, morphology) of the nanoparticle. Energy Dispersive X-ray Spectroscopy (EDX) was used to determine the elemental composition of ZIF-8 and APA@ZIF-8 nanoparticles. X-Ray Diffraction Device (XRD) measurement determined the crystallinity and impurity of the nanoparticles be formed. XRD analysis was performed using the CuKα radiation in the Philips Xarakpert Pro diffractometer (Royal Philips Electronics, Amsterdam, The Netherlands) with a beam length of 1.541 A and keeping it at 40 kV and 25 mA. With the Fourier Transform Infrared Analysis (FT-IR)(PerkinElmer, USA), the functional groups present in ZIF-8 and APA@ZIF-8 were examined.

4.3.4. Drug Release Studies

Tumor cells have an acidic pH due to their rapid metabolism and anaerobic respiration. In addition, ZIF-8 has been shown to decompose in the acidic buffer by Sun et al. 38. This encourages current drug release kinetics to control at the pH 5.0 level, which mimics the internal environment of tumor cells; releases the drug. Moreover, release studies were performed at physiological pH 7.4. As a result, drug release kinetics were investigated in PBS at physiological temperature (37°C), pH = 7.4 and 5.0 with continuous shaking (3 mg SRF@ZIF-8 powder material was used in 1 mL). At regular intervals (0 to 120 hours), the centrifugation supernatant is removed and replaced with fresh PBS. PBS samples were collected each time. Absorbance measurement of the supernatants was taken with a UV-Vis spectrophotometer (Shimadzu-UV-2550, Japan). In order to calculate the amount of drug released, the maximum absorbance peak given by the drug was taken as a reference. (for apalutamide at 270 nm)

4.3.5. Determination of Zn^{2+} Concentration

ZIF-8 and APA@ZIF-8 nanoparticles were dissolved in three different solutions. ZIF-8 nanoparticles were dispersed in phosphate-citrate buffer at pH 5 and 6 and PBS at pH 7.4. Samples agitated at 150 rpm were centrifuged after five days, and the supernatants were transferred to a new tube for additional preparation steps. For pickling, after obtaining a 1:10 or 1: 50 dilution with HCl and DI water, the samples were analyzed by flame atomic absorption spectroscopy at a wavelength of 213.9 nm.

4.3.6. Cell Culture

Cells were cultured in a CO_2 incubator set at 37°C in RPMI 1640 or DMEM F/12 medium containing 5% penicillin/streptomycin, 5% L-glutamine, and 5-10% fetal bovine serum. The viability and proliferation of the cells were achieved by passaging the flasks after covering the 80% culture dish. Cells that actively proliferate in the logarithmic phase were used in the experiments.

4.3.7. Cell Viability and Cytotoxicity Test

The survival and growth trends of ZIF-8 and APA@ZIF-8 nanoparticles on PC-3 and LnCap 104R2 cells were determined by WST-1 cell proliferation assays. WST-1 is a non-radioactive colorimetric assay for the measurement of cell proliferation, cell viability, and cytotoxicity(Peskin & Winterbourn, 2000). This method is based on the principle that mitochondria in live cells can cleave the tetrazolium ring of the WST azol 1 agent. This reaction depends on the activity of a sensitive mitochondrial enzyme, succinate dehydrogenase. As a result of the cleavage of the tetrazolium ring, the pale yellow WST-1 agent is transformed into a yellow formazan product. For this purpose, cells at a concentration of 5000 cells/well were seeded into 96-well cell culture dishes. These cells are incubated for 24 hours at 37°C, with 95% humidity and 5% CO2. After 24 hours, cells were incubated at various concentrations of ZIF-8 and APA@ZIF-8. Samples were sterilized by UV irritation prior to cell culture. After 24, 48, and 72 hours

of incubation, WST-1 (10 µL) solution was added and incubated for a further 2 hours. The absorbance of each well was monitored at 440 nm.

4.3.8. Apoptosis Analysis

The apoptotic effects of ZIF-8 and APA@ZIF-8 nanoparticles on PC-3 and LnCaP cells were tested using Annexin V-FITC Detection Kit. (BioVision,USA). Into 6-well plates, 1980 µL of cell suspension at a density of 5x105 cells per well were inoculated and incubated in a CO2 incubator at 37°C. After 24 hours, 20 µL of test compounds dissolved in DMSO were added to incubated cells at a final volume of 2 mL and final concentrations of 5, 10, 20 µg/mL. The treated cells were incubated for 24 hours in a CO2 incubator at 37°C. After incubation, cells were harvested by trypsin and centrifuged at 800 rpm for 5 minutes. The pellet was dissolved in 5 mL of PBS and centrifuged again. The pellet was resuspended in 250 µL of binding buffer, 1 µL of Annexin V-FITC, and 2,5 µL of PI were added. The stained cells were incubated for 15 minutes at room temperature. After incubation, the apoptotic effects of test compounds were determined by a flow cytometer (BD FACSCanto, USA)

4.3.9. Cell Cycle Analysis

The effects of ZIF-8 and APA@ZIF-8 nanoparticles on the cell cycle were tested in PC-3 and LnCaP cancer cell lines by propidium iodide staining (BioVision, USA). Into 6-well plates, 1980 µL of cell suspension at a density of 5 x 10^5 cells per well were inoculated and incubated for 24 hours. Test compounds were dissolved in DMSO and added to incubated cells to maintain the final concentrations of 5, 10, 20, 50, 100 µg/mL. The cells treated with test compounds were incubated for 24 hours in a CO_2 incubator at 37 °C.

After incubation, cells were harvested by trypsin and centrifuged at 1200 rpm for 10 minutes. The supernatant was poured, and the pellet was dissolved in 5 mL of PBS. The cell suspension was centrifuged again. The pellet was resuspended in 1 mL cold PBS and fixed by adding 4 mL of -20 °C ethanol (99.8%) (Merck) on a low-speed vortex. The

fixed cells were incubated at -20 °C for at least 24 hours. After incubation, the fixed cell suspension was centrifuged at 1200 rpm for 10 minutes at 4 °C. The pellet was dissolved in 5 mL of PBS and centrifuged again. The pellet was resuspended in a 200 µL phosphate buffer, including 0.1% Triton X-100. 20 µL RNase A (200 µg/mL) was added to the cell suspension, and cells were incubated in a CO2 incubator at 37 °C for 30 minutes. After incubation, 20 µL PI (1 mg/mL) was added, and cells were incubated at room temperature for 15 minutes. The cell cycle distribution was determined by flow cytometer (BD FACSCanto, USA), and data were analyzed by ModFit LT software. For each sample, at least 10,000 events were collected.

4.3.10. Serum protein binding and hemolysis

Fetal bovine serum (FBS): nanocarrier mixtures were prepared at 10:90, 20:80, 40:60 and 60:40 (v/v) ratios with 1000 µL final volume. The mixtures were incubated for two h at 37oC and centrifugated. Pellets were washed with PBS buffer (pH 7.4). Bradford assay(Bradford, 1976) was used for protein determination in supernatants, then protein-binding amount and yield were calculated.

To determine hemolysis potentials, erythrocytes were mixed with nanoparticles at 1, 5, and 10 µg/mL ZIF-8 and APA@ZIF-8 (in PBS solution) at a 1:1 (v/v) ratio and incubated at 37oC for 4 h. PBS was used as a negative control group and 1% Triton X-100 as a positive control group. End of incubation, erythrocytes and nanocarriers were separated from the mixture by centrifugation, and hemoglobin was spectrophotometrically determined at the upper layer at 540 nm. Hemolysis ratio calculated via absorbance with the formula below(Mayer et al., 2009; Yallapu et al., 2015).

(% Hemolysis = (A sample - A negative control) *100/A positive control)

4.3.11. Reactive Oxygen Species (ROS) Detection Assay

ROS Assay is a measurement that is aimed to measure reactive oxygen species in a cell, mainly hydroxyl, peroxyl, and other ROS(Starkov, 2010). The assay mechanism

consists of the fluorogenic probe DCFH-DA diffusing into the cells and deacetylated by the cellular esterases into the non-fluorescent DCFH. Following this, in the presence of ROS, DCFH is quickly oxidized to DCF, which is a significantly fluorescent compound. This fluorescence comes to "light" in the fluorescent plate reader.

Drugs are metabolized mainly by Cyt450 and produce radicals that are converted to radicals of ROS. ROS then accumulates into oxidative stress and functions in apoptosis induction, tying them to both drugs and apoptosis. ROS assay helps visualize dosage & ROS relation ROS assay aids in comparing different drug combinations and their effects. It can express individual cell line reactions to the studied drug type, dosage, and duration alike. It also presents an illustration of duration and dosage comparison.

BioVision Reactive Oxygen Detection Assay (USA) protocol followed by manufacturer guidelines. On a 96-well plate, adherent cells were seeded with $2.5x10^4$ concentration. Cells were then incubated for 24 hours until 70-80 % confluence was reached. After 24 hours of incubation, old media were removed. Adherent cells were rinsed with 100 µl of ROS buffer. Then, 100 µl of ROS label was diluted in ROS buffer added in each well and incubated in the dark. ROS label was then removed, and 100 µl of ROS buffer or PBS was added. After addition, varying nanoparticles concentrations were added and incubated for 24 h. ROS buffer was used as a control. Spectroscopic measurement was performed at 495 excitations and 529 emission ranges.

4.3.12. Reporter Assay

1×10^5 LNCaP cells were seeded in 48 well culture plate and cultured at 37°C for 48 h, and transfected with Fugene vectors for 24 h. Then the cells were treated with APA, ZIF-8, APA@ZIF-8, and R1881 for 24h and then washed with PBS and collected with passive lysis buffer. Luciferase activity was measured by using a dual-luciferase reporter activity kit (Promega, Mannheim, Germany).

4.3.13. Western-Blot

In order to determine the varying protein amounts of Apalutamide, ZIF-8, APA@ZIF-8 in prostate cancer cells, western blot analysis was performed by treating with antibodies to the desired proteins by total protein isolation. For this purpose, cells were scraped with cell scrapers, and cell lysate was collected into 1.5 mL Eppendorf tubes by treatment with RIPA (50mM Tris-HCl pH 7.4, 150 mM NaCl, 1 mM EDTA pH 8.0, 1% NP-40, 1X protease inhibitor cocktail, 1 mM NaF, 1 mM Na3VO4) buffer. Mixed at 5-minute intervals on ice and incubated for 30 minutes. After incubation, the cells were centrifuged at 13000 rpm for 15 minutes, and the supernatant was collected. The total protein amount in the collected supernatant was determined by BCA assay. After the protein amount was determined, equal amounts of protein samples (40µg) were loaded into 10-12% SDS polyacrylamide gel electrophoresis. The proteins in the run gel were then transferred to the PVDF membrane by electroblotting. The transferred proteins were blocked for 1 hour at room temperature with Tris buffer containing 5% skimmed milk powder and 0.1% Tween-20. To determine androgen sensitivity after blocking and to examine its changes, KLK4(PSA), AR, NKX3.1, and y-H2AX(S139), pATM(S1981) for possible DNA damage, and B-actin proteins as controls, to these proteins were examined by hybridization with specific antibodies. Antibodies used will be diluted at 1:500 and 1:1000 concentrations in phosphate buffer containing 0.1% Tween-20 and 3% bovine serum albumin and incubated in the membrane at 4˚C overnight. After this incubation, 1 mL of ECL-Plus reagent (1:1 ratio A and B solution, respectively) was prepared for each membrane with the HRP enzyme attached to the second antibody tip for 1 hour at room temperature. The ECL solution was poured over the membrane in the darkroom at low agitation for 4 minutes and spread over the entire membrane surface. The film placed between two acetate sheets on the membrane tray was placed at different exposure periods. The film was first washed with a developer solution, and then patches of Fixer solution were seen on the film provided. As an experimental control, β-actin was used during the whole analysis.

4.4. RESULTS and DISCUSSION

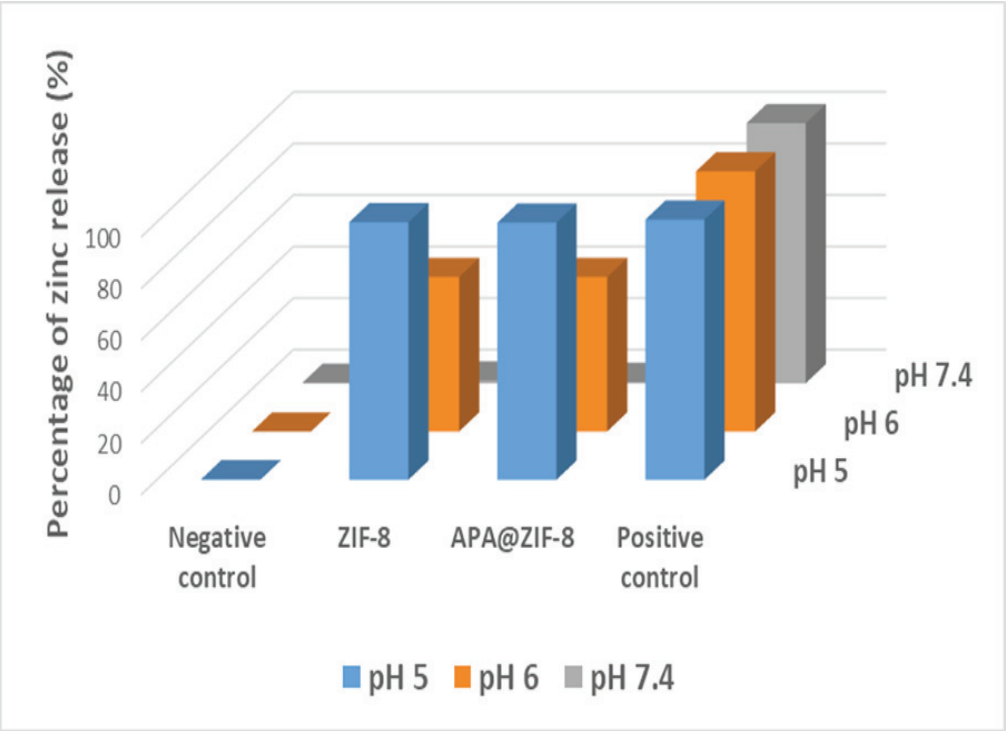

Figure 4.2. Zinc release from ZIF-8 and APA@ZIF-8 at pH 7.4, 6 and 5

The synthesis of ZIF-8 and APA@ZIF-8 nanoparticles were performed using the one-pot method. The most important feature of this material is that it is pH sensitive, so it has been tested for stability. To assess the stability of ZIF-8 crystals in different pHs (pH 7.4, 6, and 5), we incubated ZIF-8 for five days at room temperature and determined the release of Zn^{2+} by atomic absorption spectroscopy (AAS). Fig 4.2. shows a nearly inversely proportional relationship between pH and release of Zn^{2+} in the supernatant. Because ZIF-8 is degraded due to their weak coordination bonds at low pH values. Interestingly, at a concentration of 30 µg mL^{-1} of ZIF-8 crystals, the amount of Zn^{2+} released was around 3–5 µg mL^{-1}, a value that corresponds to reported in the literature, 3–6.4 µg mL^{-1} in the human blood (Buxaderas & Farré-Rovira, 1985).

We aimed to synthesize nanocrystals capable of encapsulating apalutamide with high loading, high yield, high encapsulation efficiency, and small size. ICP-OES has been

used to determine the effective APA loading capacity. The final adsorbed APA in ZIF-8 depends on the relative affinity of the solvent, the drug, and the porous internal surface.

Table 4. Yield, Hydrodynamic radius, Drug loading capacity, and zeta potentials of a)ZIF-8 and b)APA@ZIF-8

	Yield (%)	**Hydrodynamic radius (nm)**	**Drug Loading Capacity (%)**	**Zeta Potential (mV)**
ZIF-8	68,3	340		-21,3
APA@ZIF-8	69,4	200	47,8	24,5

SEM Images of the nanocrystals suggested significantly smaller than those found by Dynamic Light Scattering (DLS) measurements (Fig 4.3.). This can be interpreted as the fact that the DLS method displays the hydrodynamic diameter of the nanocomposites while SEM shows them in a dry state. It cannot be excluded that the aggregation of some smaller particles occurred, which can also indicate a larger size during the DLS study. The zeta potential measurements might support this latter hypothesis, which provided relatively low negative values, which means that their aggregation might have taken place. Therefore, zeta potential and hydrodynamic radii of ZIF-8 and APA@ZIF-8 nanoparticles synthesized were investigated by DLS measurement. The zeta potentials of ZIF-8 and APA@ZIF-8 nanoparticles were measured as -21,3 and 24,5 mV, respectively. This change in zeta potential can be attributed to the encapsulation of the drug(Joseph & Singhvi, 2019). The electronegativity enhances the cellular uptake with a negative zeta potential, providing better mitochondria targetability, cell biocompatibility(Apostolova & Victor, 2015).

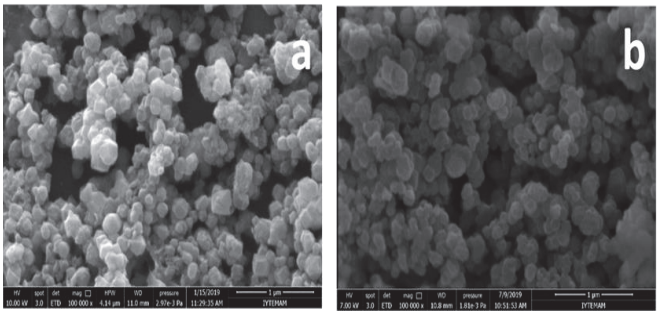

Figure 4.3. SEM micrographs of a)ZIF-8 and b) APA@ZIF-8

Scanning electron microscopy (SEM) showed that the ZIF-8 and APA@ZIF-8 nanoparticles consisted of isolated crack-free particles diameter between 113,89−200,18 nm. As shown in Fig 4.3, scanning electron microscopy (SEM) images of the resulting structures indicate the formation of rhombic dodecahedral crystals, corresponding to the average size of biomedically relevant ZIF-8 encapsulating biomacromolecules, as previously reported by Falcaro and co-workers(Hoop et al., 2018). As expected,energy-dispersive X-ray (EDX) spectroscopy maps confirm the presence of Zn, C, and N elements uniformly distributed throughout each crystal, whereas apalutamide has F and S.

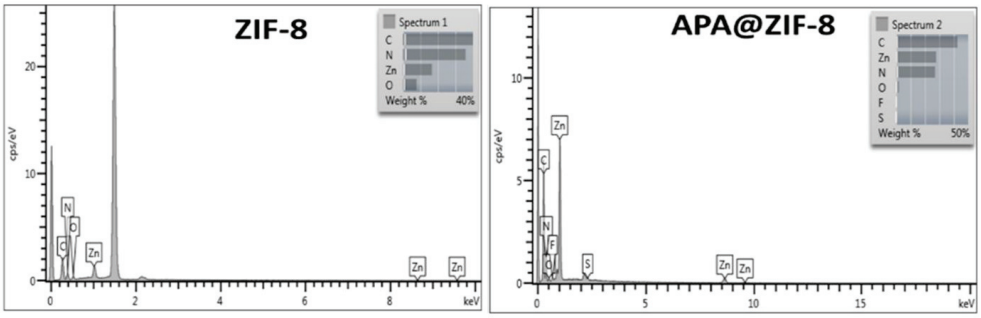

Element	Wt%	Atomic %
C	39.98	50.29
N	35.72	38.53
O	7.80	7.37
Zn	16.50	3.81
Total:	100.00	100.00

Element	Wt%	Atomic %
C	42.52	58.50
N	26.99	31.85
O	1.85	1.91
F	0.77	0.67
S	0.12	0.06
Zn	27.75	7.02
Total:	100.00	100.00

Figure 4.4. EDX Analysis of a)ZIF-8 and b)APA@ZIF-8

Comparison of the sample XRD pattern to the pattern simulated from the published ZIF-8 structure data indicates that the product is pure-phase ZIF-8 material. Each synthesis yielded pure-phase ZIF-8 crystals, as demonstrated by XRD (Fig 4.5). Patterns generated by the ordered porous structure of the ZIF-8 particles between 2θ values of 5 and 40° can be observed, and the peak broadening observed indicates the formation of nanosized crystals. The relative intensities and the sharp peaks in the diffraction pattern of ZIF-8 at 2θ=7.11°, 12.5°, 17.75°, and 26.4° prominent peak positions, including 011, 002, 112, 022, 013, and 222, are in good agreement with previous reports,(Cravillon et al., 2009; Park, Ni, Côté, Choi, Huang, Uribe-Romo, Chae, O'Keeffe, et al., 2006) confirming the sodalite structure, which is the typical structure of ZIF-8, and the well-defined peaks revealed high crystallinity. The interplanar spacings calculated using Bragg's law from the reflection at different Bragg's angles correspond to a body-centered cubic structure with a unit cell parameter of 17 Å. They are following those reported in the literature (A. Schejn et al., 2014b). The growth of ZIF-8 crystals is known to evolve with time from cubes exposing 6 (Al-Salama) faces to intermediate shapes. Then to rhombic dodecahedra, 23 exposing 12 (Cui et al.) faces and, this final being is likely the most stable equilibrium morphology of ZIF-8.

The XRD shows the exact crystal structure of ZIF-8 nanoparticles showing that the addition of APA did not alter the structure of ZIF-8. XRD analysis of the APA@ZIF-8 shows unchanged lattice parameters for ZIF-8 before and after APA loading. (fig.4.6) According to XRD results, the sharp peaks of APA@ZIF-8 are consistent with stimulated ZIF-8, which means APA has no effect on the structure of the ZIF-8, and its crystal structure remains intact. APA seems to react with neither Zn2+ nor 2-methylimidazole.

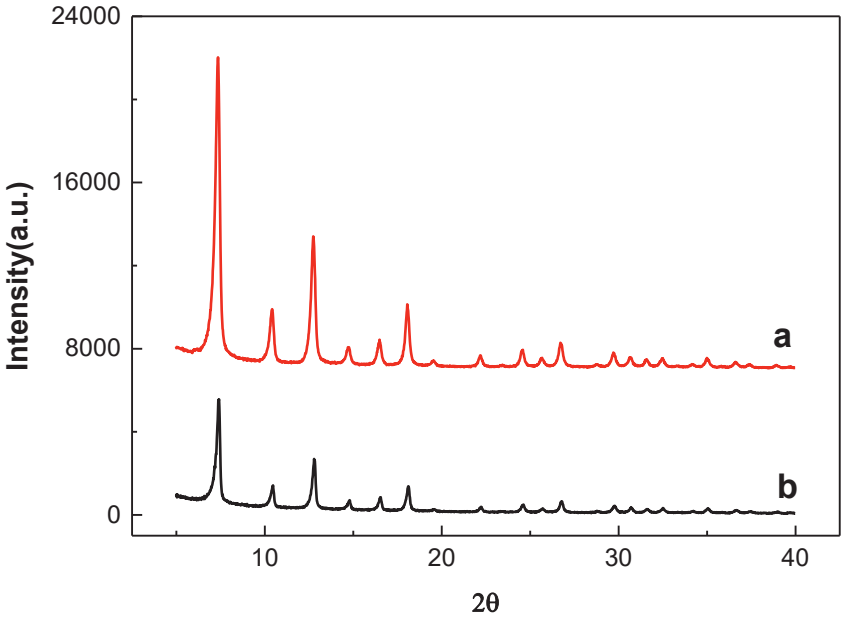

Figure 4.5. XRD patterns of a)ZIF-8 and APA@ZIF-8

FTIR spectra were obtained for ZIF-8 and APA@ZIF-8. In the spectrum corresponding to ZIF-8, two bands at 3135 and 2928 cm^{-1} can be observed for the aromatic C–H stretch and the aliphatic C–H stretch of the imidazole, respectively. The 1606 cm^{-1} band is for the C–C stretch, and the peak at 1580 cm^{-1} is for the C–N stretch. The C–N absorption bands are found in the 1100–1400 cm^{-1} region. The absorption band at 421 cm^{-1} is associated with the Zn–N stretching mode. These assignments are in agreement with the FTIR measurements from Park et al.(Park, Ni, Côté, Choi, Huang, Uribe-Romo, Chae, O'Keeffe, et al., 2006). Several bands are observed for APA@ZIF-8. The FTIR spectrum analysis for the system APA@ZIF-8 undoubtedly shows the adsorption of drugs into ZIF-8, but the detection of characteristic bands for both ZIF-8 and drugs indicates the presence of both compounds.

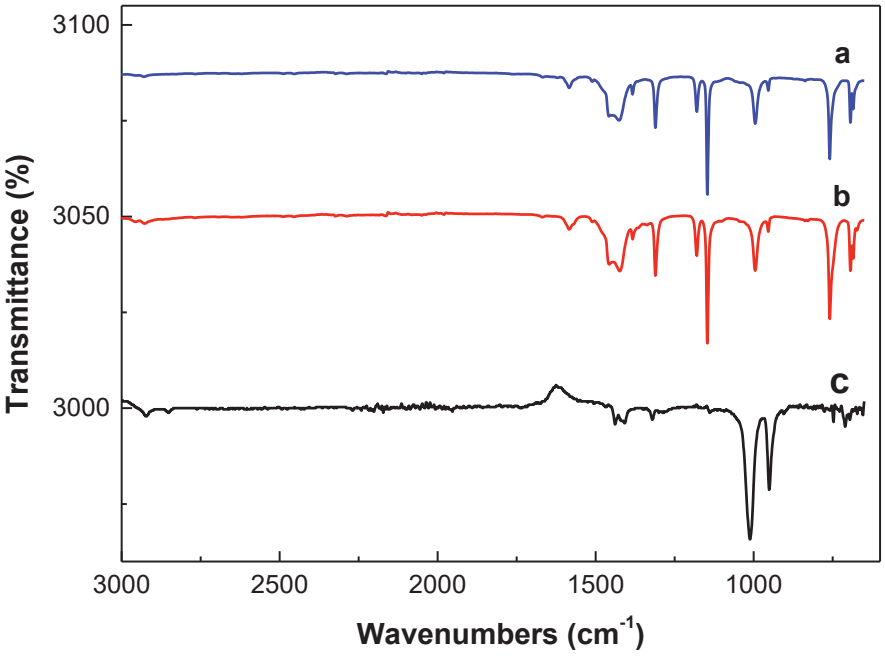

Figure 4.6. FTIR spectra for a) ZIF-8 b) APA@ZIF-8, and c) APA

The slopes of weight loss obtained from thermogravimetric analysis of ZIF-8 and APA @ ZIF-8 under nitrogen gas are shown in Figure 17. It is known that ZIF-8 is stable up to 450-500°C and begins to decompose above. According to the TGA slopes obtained, the change in mass of both nanoparticles is similar up to 130°C. When reaching 200°C, APA@ZIF-8 nanoparticles lost approximately 9%, while this ratio remained at 0.64% in ZIF-8 nanoparticles. After the decrease of approximately 8.5% continued up to 400°C, the difference was equalized at 583°C. This difference in the thermogravimetric slope indicates the presence of the drug in APA@ZIF-8 nanoparticles. Since there is no guest molecule left at this stage, it is thought that both nanoparticles show a similar slope. Above 620ºC, the last weight loss of 30% was observed related to the collapse of the crystal structure by decomposing the nanoparticles at high temperatures(A. Schejn et al., 2014c).

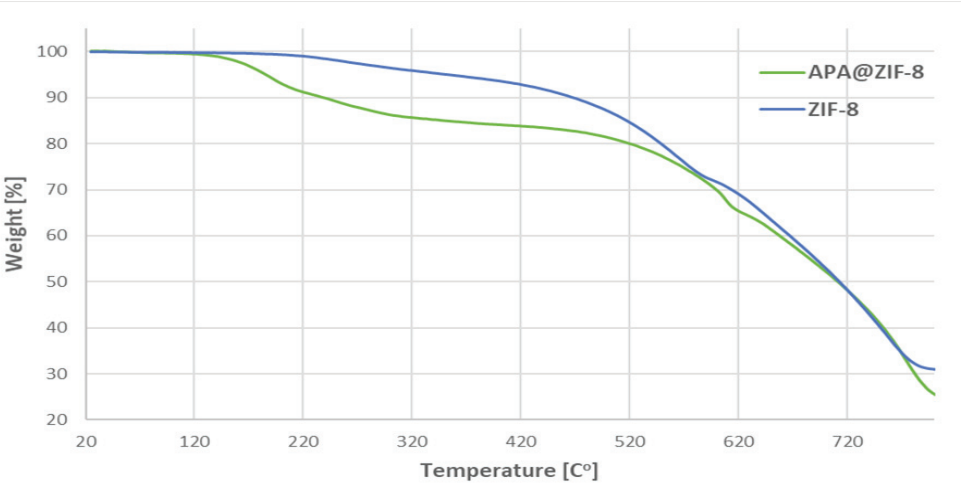

Figure 4.7. TGA graphs of ZIF-8 and APA@ZIF-8

Metal-organic frameworks are organic coordination compounds with high porosity. The surface areas of these materials are quite large. Therefore, the N_2 adsorption/desorption slopes of the ZIF-8 nanoparticles were deduced (Fig 4.7). The curve obtained corresponds to the Type I isotherm. This measurement calculated that the nanoparticles had 1017.3249 m^2/g and 1495.7186 m^2/g BET and Langmuir surface areas. The found surface area results were compatible with the literature(Y. Feng, Li, Xu, Liu, & Yao, 2016).

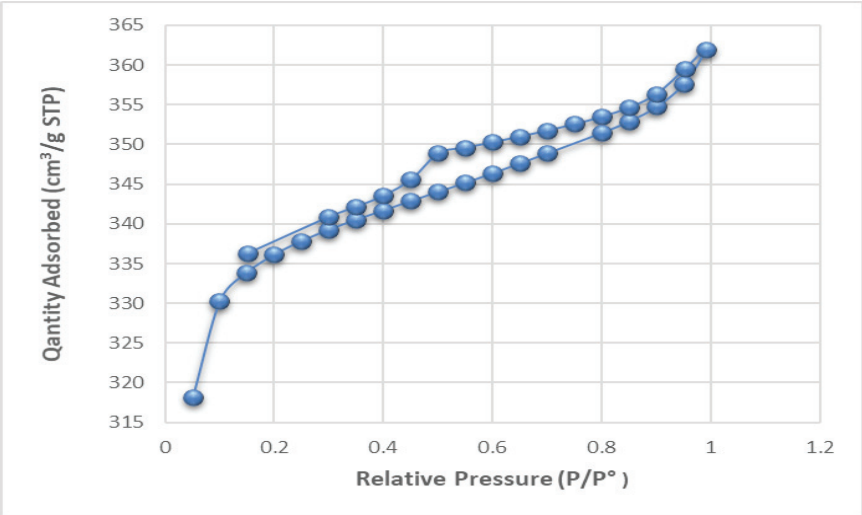

Figure 4.8. N_2 adsorption/desorption slopes of the ZIF-8

In order to observe the change of drug release from APA@ZIF-8 nanoparticles over time, pH 5 solution mimicking acidic cancer cell environment and pH 7.4 PBS buffer solutions as typical cell environment. APA@ZIF-8 nanoparticles were incubated in these two different pH environments at 150 rpm for five days. Absorbance values of supernatants were measured with a UV-Vis spectrophotometer to calculate the amount of drug released in a specific time period. The cumulative drug release was obtained at pH 5, and 7.4 which is shown in Fig 18. According to these results, drug release from the nanoparticles observed is fast at pH 5, while it exhibits a slower profile at pH 7.4, as in the literature. A slight burst release behavior was observed at the beginning, which may be caused by framework degradation, and APA@ZIF-8 presented a significant pH-dependent release behavior. It was observed that the drug released from APA@ZIF-8 reached the release plateau within the first 12 hours, and after this period, there was a slight increase in drug release. When the release of the drug at pH 7.4 was examined, it was observed that it reached the plateau in the first 48 hours, and the release remained at 60% within five days.

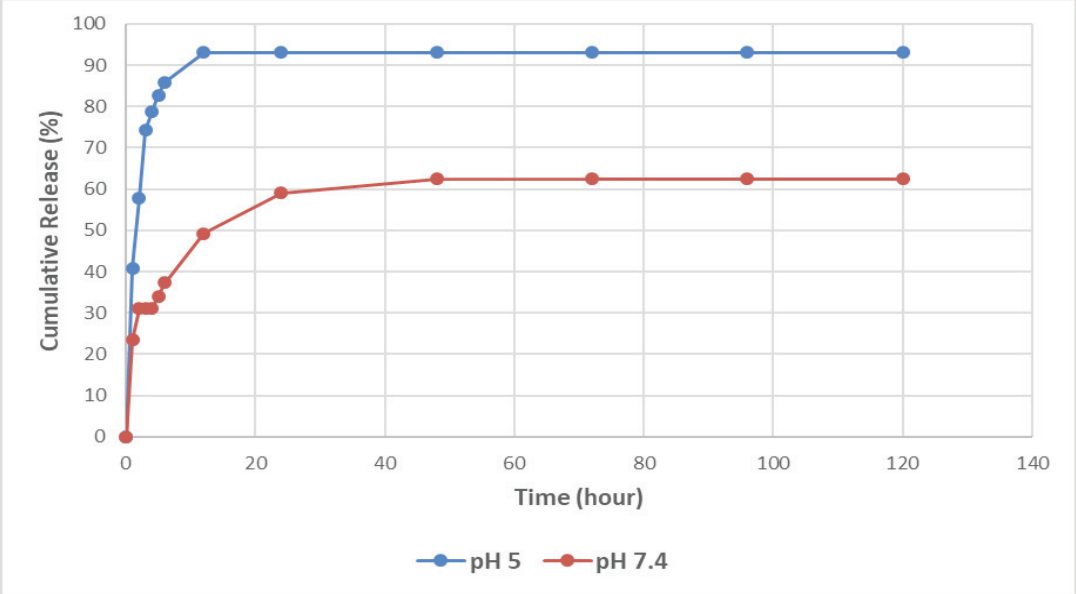

Figure 4.9. Drug release profiles of APA @ ZIF-8 nanoparticles at pH 5 and 7.4

ZIF-8 and APA@ZIF-8 (3mg mL^{-1}) nanoparticles were incubated in PBS (1X) buffer medium, an acidic medium (pH 3, 5) at 37°C for 1-48 hours. The pellet (solid) collected after the incubation of ZIF-8 nanoparticles was analyzed by XRD. Accordingly, it has been shown that the rhombic dodecahedral-shaped morphology of ZIF-8 nanoparticles is disrupted. (Fig 4.10). It has been found that the normalized intensity of the peak originating from the plane of the Sod-ZIF-8 crystal (011) decreases with increasing incubation time. In particular, after 1 hour, the peak intensity falls below its original value. When the XRD patterns collected after the incubation process were examined, no new diffraction peaks suggesting by-product formation were observed. XRD patterns show that APA@ZIF-8 particles decay faster than ZIF-8 particles. This was evidenced by the rapid decrease in the intensity of both Bragg peaks of the sodalite ZIF-8. The decrease in the scattering intensity at the low angle diffraction peak attributed to plane (011) sod-ZIF-8 showed the instability of the ZIF-8 particles in the PBS solution, and the crystallinity completely disappeared within 2 hours(fig 20). The faster degradation of APA@ZIF-8 particles can be explained by the large surface area exposed to the PBS environment. All nanoparticles did not degrade after 48 hours of incubation at 37°C and pH 7.4.

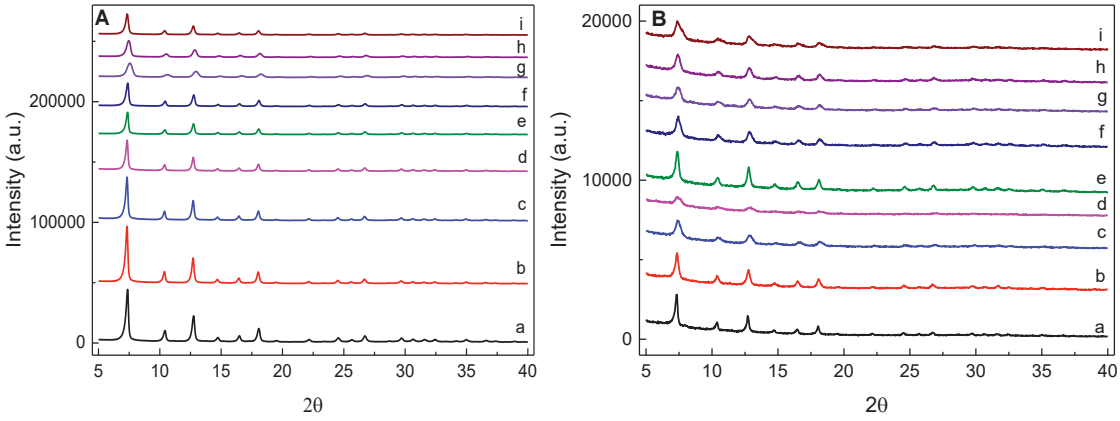

Figure 4.10. XRD patterns illustrating the structural evolution of A)ZIF-8 and B)APA@ZIF-8 particles before and after the incubation process in PBS pH 5.[a) 0 h b) 30 min c) 1 h d)2he) 4hf) 6hg) 12hh) 24h i) 48h]

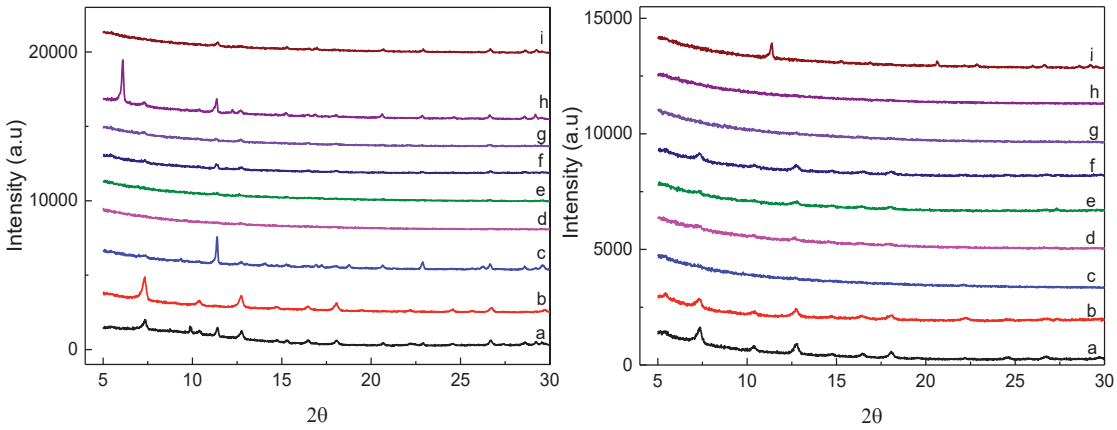

Figure 4.11. XRD patterns illustrating the structural evolution of A)ZIF-8 and B)APA@ZIF-8 particles before and after the incubation process in PBS pH 3.[a) 0 h b) 30 min c) 1 h d)2he) 4hf) 6hg) 12hh) 24h i) 48h]

The rate of binding of synthesized nanoparticles to serum proteins was investigated to show the biocompatibility of ZIF-8 and APA@ZIF-8 nanoparticles. The amount of serum proteins binding was calculated by measuring FBS (as serum protein equivalent) in the presence of nanoparticles after two hours of incubation at 37°C. Since it is known that intravenous drugs are removed from the body in approximately 2 hours, the time is set as 2 hours. In addition, incubation was carried out at 37°C, which is body temperature. Since serum protein can vary from person to person, trials have been conducted by changing the serum: drug carrier ratios. The maximum binding ratio of nanoparticles to proteins was observed at a ratio of 60:40 serum: ZIF-8. The value found corresponds to 45.32%. When other serum: nanocarrier ratios are examined, the percentage of binding to serum proteins of nanoparticles with or without drugs is much lower.

Another method used during the evaluation of nanoparticles in terms of biocompatibility is hemolysis analysis. Erythrocytes, also known as red blood cells, constitute 48% of blood. The erythrocytes-ZIF-8s interaction is essential to study the hemoglobin release(known as hemolysis). The percentage of erythrocyte cells in the blood in the presence of ZIF-8 and APA@ZIF-8 nanoparticles was investigated. It is known that increased concentration of nanoparticles and especially positive surface charged nanoparticles undergo more hemolysis than negatively charged ones by erythrocytes in blood [13-14]. In the light of this information, the hemolysis rate of ZIF-8 and APA@ZIF-8 nanoparticles on erythrocytes was investigated in three concentrations: 1 µg/mL,5 µg/mL, and 10 µg/mL. The hemolysis rate of ZIF-8 and APA@ZIF-8

nanoparticles was found to be consistent with each other as 0.53% and 0.54%, respectively (Fig 4.12). The addition of nanoparticles resulted in lowering the hemolysis value. Furthermore, these values are well within the hemolytic limit (5%) as per ASTM F-756-08 standard. (ref) Thus, the results indicated the non-hemolytic nature of the ZIF-8 and APA@ZIF-8 nanoparticles that the values are below 5%, which supports the biocompatibility of the nanoparticles(Modi, Verma, & Bellare, 2018).

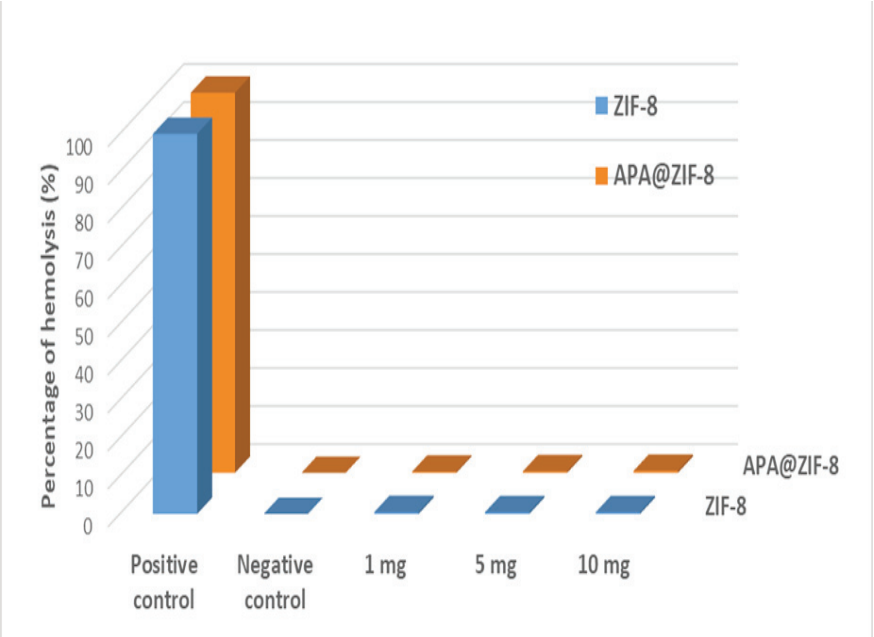

Figure 4.12. Hemolysis rates of ZIF-8 and APA@ZIF-8 nanoparticles

WST-1 is a non-radioactive colorimetric assay to measure cell proliferation, cell viability, and cytotoxicity. This method is based on the principle that mitochondria in live cells can cleave the tetrazolium ring of the WST-1 agent. This reaction depends on the activity of a sensitive mitochondrial enzyme, succinate dehydrogenase. As a result of the cleavage of the tetrazolium ring, the pale yellow WST-1 agent is transformed into a yellow formazan product.

Fig.4.13 represents WST-1 readings depicting cell viability response of LNCaP prostate cancer cell line exposed to 250, 100, 50, and 25 µg/mL of ZIF-8 and APA@ZIF-8 at 24, 48, and 72 hours respectively. ZIF-8 is degraded in Zn^{+2} and 2-MIM, which is biodegradable and biocompatible with negligible cell viability influence tested on A549 and HeLa cell lines. However, Zn^{+2} is known to have regenerative effects, thus constituting beneficial cell viability result of ZIF-8 exposure shows the cell viability values of all cell lines after 24, 48, and 72 hours, respectively. However, the extent of this

exposure has a limit, as it is also known that above 30 µg/mL level ZIF-8 proves to be cytotoxic.

Our XRD measurements indicate ZIF-8 completely degrades into its constituents within 48 hours. Our results of the above cell viability associated with this finding can see from 24 to 48 hours starting 25 µg/mL increases in LNCaP cell viability. The peak will be reduced only a little in the 72-hours (Fig 22a). This occurs from that introduced finite ZIF-8 amount leading to a finite Zn+2 ion release, and thereby this amount is entirely metabolized by the LNCaP cell line. For ZIF-8, it is observed that viability levels for all three concentrations are lower than those of 25 µg/mL while following a similar trend due to cytotoxic Zn^{+2} being peaked at 48 hours. For APA@ZIF-8, the expected result is a gradual loss of cell viability, as our drug release studies prove that around pH 5.0, APA is detected to be released from ZIF-8 after 4-6 hours. Our 24 hours results show no significant reduction in cell viability upon comparison with ZIF-8 treatment. Nevertheless, once 48 hours is reached, cell viability is reduced around 15-30 %, with top reduction belonging to 250 µg/mL. This cell viability reduction is continued for 72 hours for 250, 100, and 50 µg/mL concentrations.

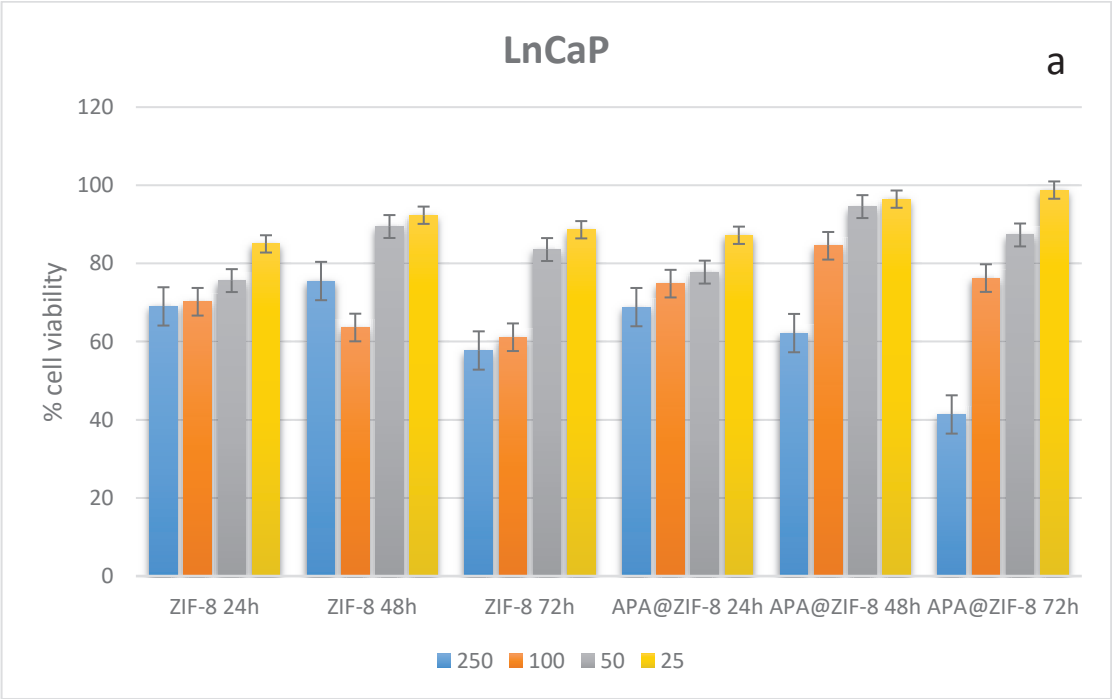

Fig 4.13b demonstrates the cellular viability profile presented by 104R2 towards ZIF-8 and APA@ZIF-8 exposure throughout 24, 48, and 72h. Within each dosage and time point, APA@ZIF-8 has demonstrated dosage-dependent cell viability reduction for 104R2. Towards ZIF-8, however, 104R2 cell line has not expressed proliferation decrease. 104R2 cell line compared to both LNCaP and PC-3 cell lines has been less responsive to both ZIF-8 and APA@ZIF-8 exposure. (104R2 androgen-independent, LNCaP androgen-dependent, PC3 prostate cancer cell line).

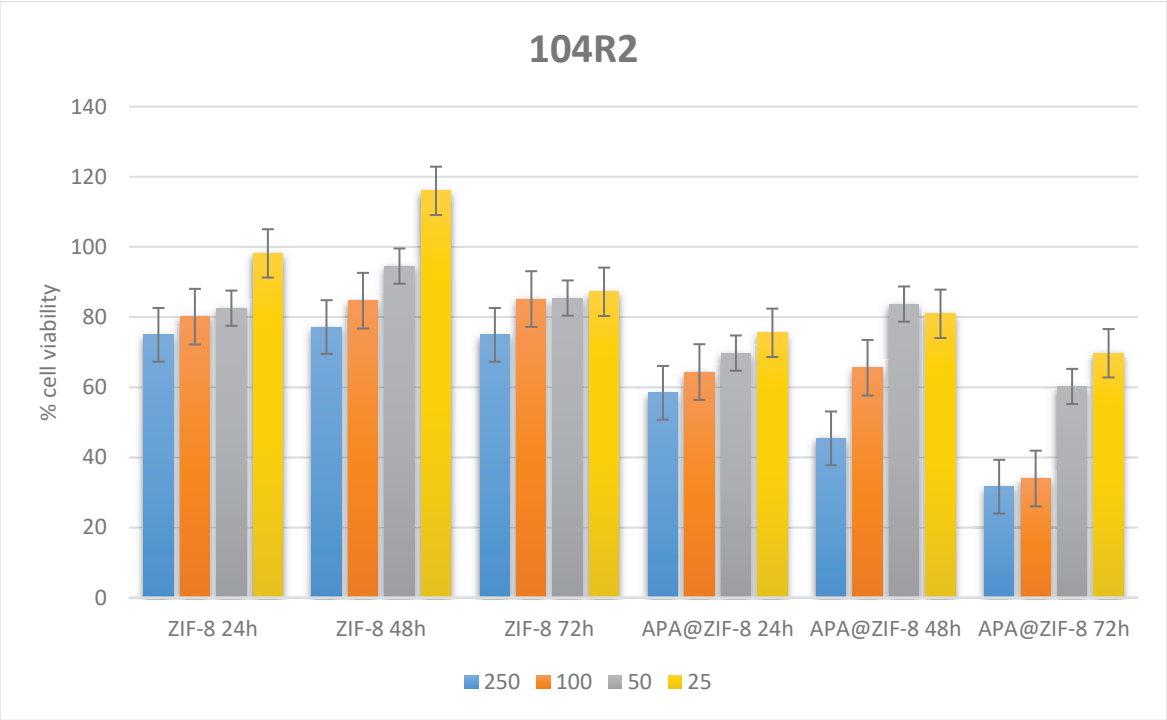

Figure 4.13c shows the cytotoxic activity profiles of ZIF-8 and APA@ZIF-8 on PC3 cell lines at 24, 48, and 72 hours respectively. The PC3 cell line has expressed viability response to both ZIF-8 and APA@ZIF-8. The response was correlated with dosage as the lowest noted viabilities for ZIF-8 recorded at 250 µg/ml in each time point. Viability data presents that the above concentrations of 25 µg/ml of APA@ZIF-8 are effective on PC3 and cause a significant proliferation decline.

Fig. 4.13 suggests that the cytotoxic efficacy of the APA@ZIF-8 is accumulative over time. The reason is that the APA release, even the burst-release mentioned above, is relatively slow, supported by our XRD findings of approximately 48 hours of dissociation. The progressive anti-proliferative effect is effective on

LNCaP, 104R2, and PC3 which has characteristics of prostate stages on different stages. These results indicate the application potential of APA@ZIF-8 as bifunctional probes integrating diagnosis.

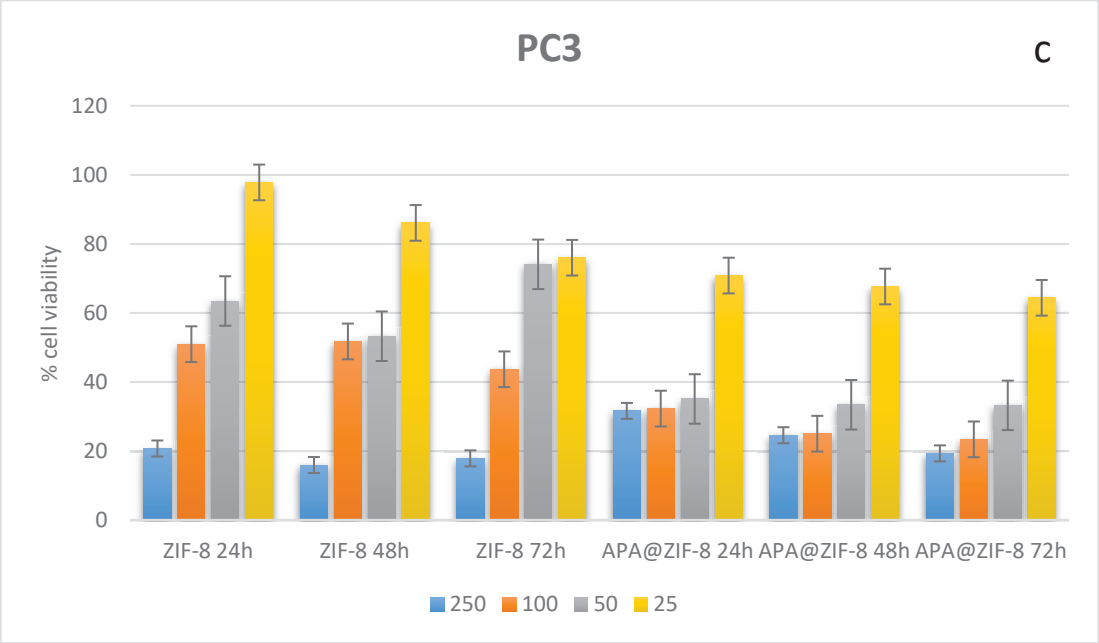

Figure 4.13. Cytotoxic activity profiles of ZIF-8 and APA@ZIF-8 in a)LnCaP, b)104R2, and c)PC3 cell lines at 24, 48, and 72 hours.

Figure 4.14. Cytotoxic activity profiles APA in a)LnCaP, b)104R2, and c)PC3 cell lines at 24, 48, and 72 hours.

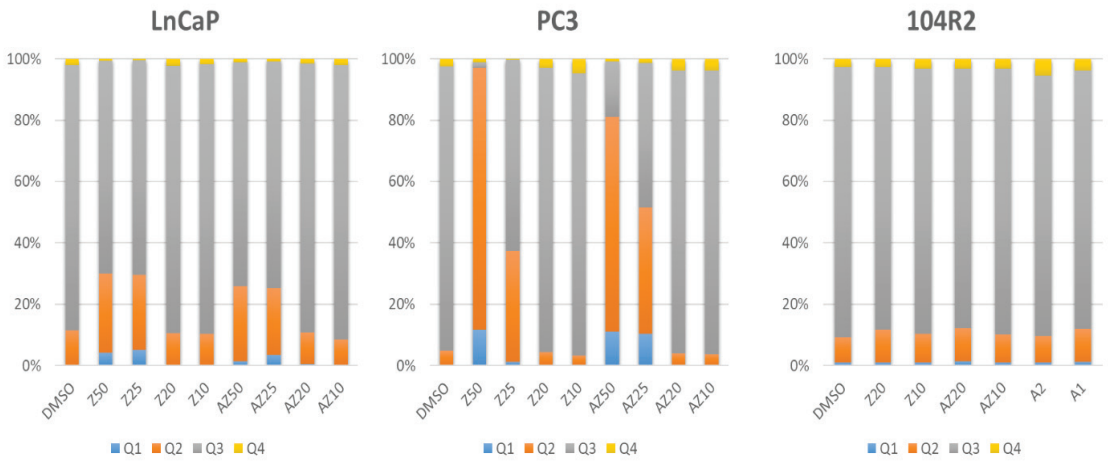

Figure 4.15. Apoptosis analysis of ZIF-8 and APA@ZIF-8 at 24 hours in LnCaP, PC3, and 104R2 cell lines (necrosis (Q1), late apoptosis (Q2), viability (Q3), and early apoptosis (Q4) rates)

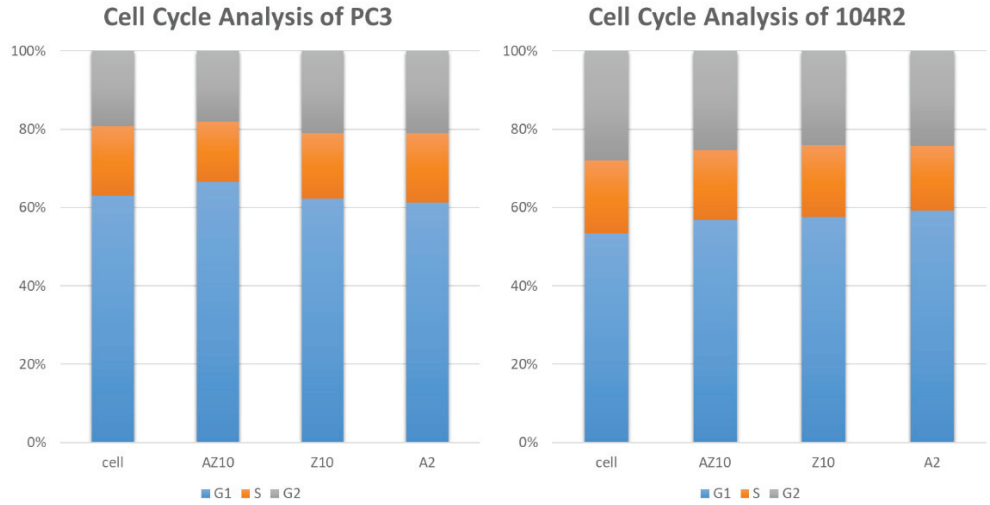

Figure 4.16. Cell cycle analysis of ZIF-8 and APA@ZIF-8 at 24 hours in PC3 and 104R2 cell lines

Reactive oxygen species (ROS) detection was performed using DCFH-DA, which can be hydrolyzed by esterase in the cell to produce DCFH. Then, DCFH is oxidized to DCF, which remains trapped within the cells by low molecular weight peroxides generated by the cells, emitting green fluorescence representing cellular ROS levels. ROS are frequently observed in tumor cells. Because of the hypoxia in tumor tissues, the ROS levels (such as hydrogen peroxide, H_2O_2) are significantly higher than those in normal tissues. Oxidative stress is one of the significant indicators for induced cellular toxicity,

and its regulation helps alter the biological response to materials. 2′, 7′-dichlorofluorescein diacetate (DCFH-DA) fluorescence is a commonly used marker for oxidative stress in cells. Thus, the reduction in DCF fluorescent intensity, in other words, is indicative of the reduction in ROS generation, which confirmed the better antioxidative property of nanoparticles. According to our ROS detection results (Fig 23), it has been observed that the drug induces the lowest presence while APA@ZIF-8 provides a higher value. The possible action path is presented as high zinc accumulation in ZIF-8 incubated cells leads to high ROS levels and cellular inflammation. This phenomenon occurs because ZIF-8 releases the drug in a slow yet stable fashion combined with the regenerative properties of the Zn^{+2} ions released upon ZIF-8 degradation, concluding in more oxidative stress and, thereby, ROS generation.

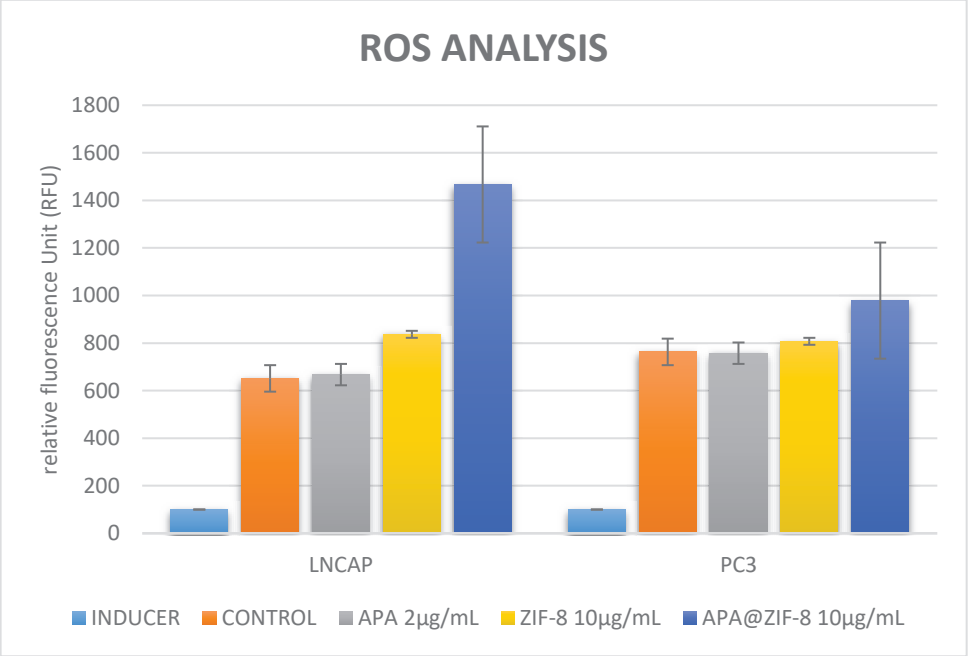

Figure 4.17. ROS levels of ZIF-8 and APA@ZIF-8 in LnCaP and PC3 cell lines at 24 hours.

Increased intracellular Zn2+concentrations have been shown to inhibit the Krebs cycle associated with enzymes (e.g., glycerol-3-phosphate dehydrogenase), induce permeability transition of the mitochondrial membrane, and inhibit the mitochondrial bc1cytochrome complex, leading to an augmented production and accumulation of reactive oxygen species(ROS) [47–50]. Increased ROS generation by MOFs containing

other metallic nodes (i.e., Fe, Cr, and Al ions) has previously been reported by Yu et al. as well as Horcajada et al.. Consequently, we expected that increasing ZIF-8 crystals in the cell culture would increase Zn^{2+} concentration, causing an increment of intracellular ROS species due to the aforementioned effects. Hence, we measured the ROS generation in two cell lines upon exposure to ZIF-8, APA@ZIF-8, and APA shown in Fig.4.17. An increase in ZIF-8 resulted in increased ROS in the cells compared to the untreated cell culture. In order to illustrate the dependency of ZIF-8 concentration and ROS production, we used the cell line with the lowest ROS generation. We observed a significant increase in fluorescence signal, illustrating elevated ROS levels (Fig. 4.17). ROS species are well-known genotoxic agents causing DNA damage via the oxidation of DNA base pairs(Cooke, Evans, Dizdaroglu, & Lunec, 2003; Thorn, Gniadecki, Petersen, Vicanova, & Wulf, 2001). Augmented intracellular ROS levels cause the cell cycle arrest at the G2/M checkpoint, a necessary step for the DNA repair mechanism(Cadet & Wagner, 2013). DNA repair is no longer possible if ROS levels are above a certain threshold and cellular apoptosis pathways are eventually induced(Hua et al., 2013). Next, we tested if the enhanced ROS concentrations influenced the cell cycle in each cell line. The nuclear PI stain binds to the DNA and allows for DNA quantification. Here, cells in the S-phase are expected to have a higher DNA content than the G1 phase, and, subsequently, cells in the G2 phase have approximately double the amount of DNA than in G1. Results in Fig.; provide an overview of cells exposed to ZIF-8 in the respective cell cycle stage. No significant differences in cell cycle distribution between the control and 10 μg mL−1 ZIF-8 concentrations were observed in all cases. Hence, at this concentration, ZIF-8 appears to have a negligible effect on the cell cycle.

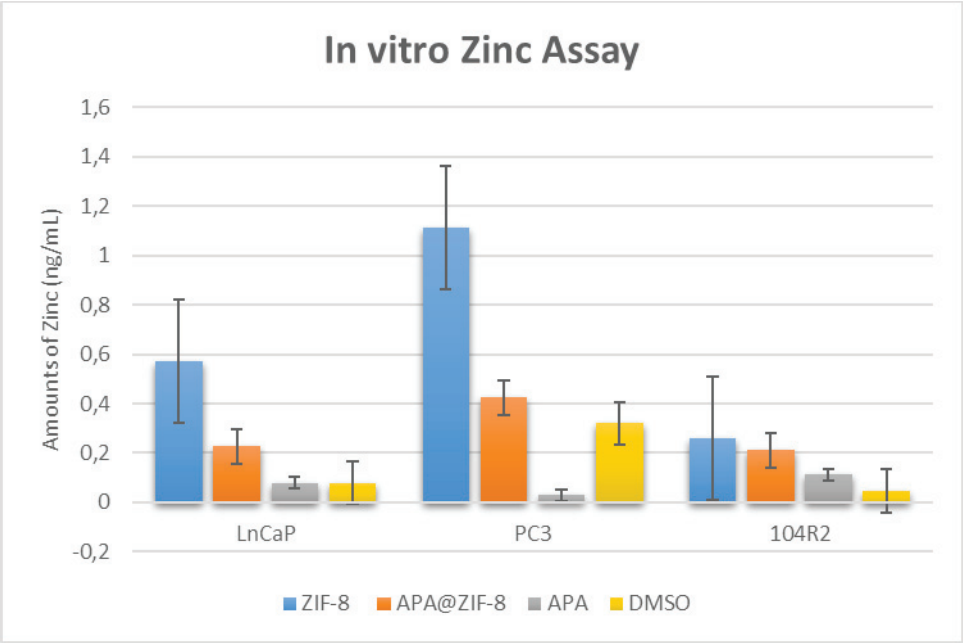

Figure 4.18. Amounts of Zn in ZIF-8 and APA@ZIF-8 in LnCaP, 104R2, and PC3 cell lines at 24 hours

Figure 4.18 depicts the intracellular zinc levels of LNCaP, PC3, and 104R2 prostate cancer cell lines 24 hours after adding 10 µg/mL ZIF-8 and APA@ZIF-8, 2 µg/mL APA and DMSO, respectively. Regardless of the amount of diameter increase due to drug loading, and since the diameter does not exceed 200 nanometers, particles and drugs are expected to be taken into cancer cells by clathrin-driven endocytosis (Syed & Chan, 2015). Low intracellular zinc concentration is one of the characteristic features of carcinoma in prostate cancer. (P. K. To, Do, Cho, & Jung, 2020). This makes it possible to observe a possible increase in the low intracellular zinc level more precisely. Although it varied between cell lines, the highest amounts of zinc were observed in 10 µg/mL ZIF-8 and APA@ZIF-8 applications, respectively. Apalutamide and DMSO do not contain zinc, and their activity mechanisms that will increase the amount of zinc in the cell after being taken into the cell are unknown. An increase of zinc amounts; shows that zinc-containing nanoparticles might be taken up into LNCaP, PC3, and 104R2 cells via endocytosis. Considering the unchanged dose and duration, different observation of intracellular zinc amounts between cell lines depends on the lines' characteristics.

It is observed that the addition of DMSO and Apalutamide does not alter the intracellular zinc level of the LNCaP cell line. It is observed that the amount of zinc increased approximately 6 times when ZIF-8 was added to LNCaP cells. In APA@ZIF-

8, the amount of zinc in the cell increased approximately 3 times. The reason why ZIF-8 application reveals the highest amount of zinc in LNCaP cells may be due to its smaller size than the APA@ZIF-8, which may be due to its higher uptake by the cell or a more favorable cell membrane protein composition of LNCaP characteristically for ZIF-8 uptake. Since the APA@ZIF-8 is taken into PC3, the amount of zinc increase appears to be small. It can also be explained that the PC3 cell line characteristically works with much higher efficiency and selectivity for the zinc removal mechanisms compared to the LNCaP and 104R2 cell lines. It can be said that the PC3 cell membrane proteins have a composition that does not accept APA@ZIF-8 nanoparticles. Zinc assay results for the 104R2 cell line; exhibits a less sensitive profile than LNCaP and PC3 cell lines. Based on DMSO, it is due to the lack of an increase in the zinc level in the cell in the application of ZIF-8 and APA@ZIF-8. Our results show that the zinc levels of 104R2 and LNCaP cells without the addition of a drug had a similar amount. The amount of zinc increased approximately six times with the addition of ZIF-8. In the 104R2 cell line, a nearly five-fold increase in the addition of APA@ZIF-8, similar to the addition of ZIF-8, is observed. There is a possibility that the 104R2 cell line may characteristically be susceptible to endocytosis of larger nanoparticles, whereas 104R2 may incorporate a fast-acting mechanism for zinc removal, such as PC3.

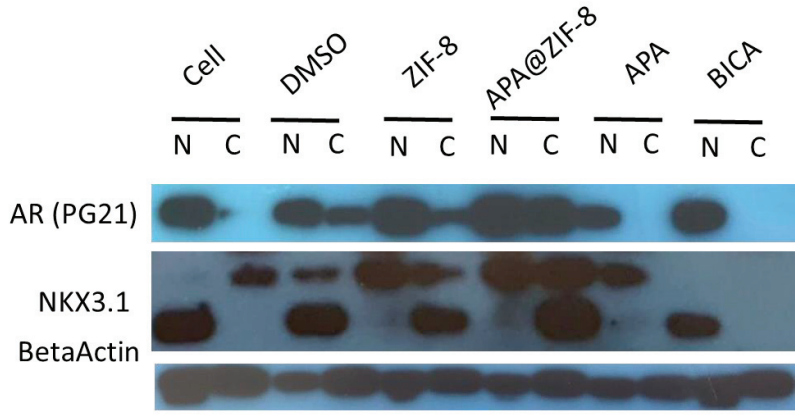

LNCaP R1881

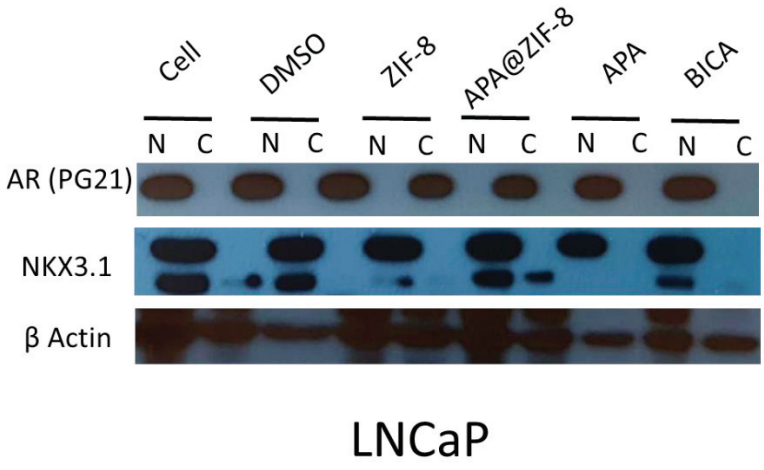

Figure 4.19. Western blot analysis was done for LNCaP and LNCaP R1881+ cells treated with 10 µg/mL ZIF-8, 10 µg/mL APA@ZIF-8, 2 µg/mL APA, 4µM Bica, and DMSO for 24 hours.

Beta-actin is ubiquitously expressed in eukaryotic cells and is considered a housekeeping gene that is frequently used as a loading control for assays involving protein detection. β-actin has been applied to gain insight into parameters such as system quality, protein isolation efficiency, tidal performance, and protein transfer. Since apalutamide is an inhibitor that prevents the translocation of the androgen receptor, an experimental setup has been designed to reveal the androgen receptor amount and androgen receptor position in the cells indicated in Figure 4.19. The literature mentions that the androgen receptor in prostate cells is present in the cytoplasm in the absence of Androgen, and the receptor is translocated to the nucleus by the binding of Androgen to the ligand region of the receptor. (Tan, Li, Xu, Melcher, & Yong, 2015). To prove that the inhibition of androgen translocation is due to Apalutamide, the androgen antagonist drug Bicalutamide was used as a positive control (Osguthorpe & Hagler, 2011). LNCaP cells require Androgen to grow, and although it is present in the medium provided for this growth, it is thought that androgen receptor translocation will not occur in the specified samples since sufficient androgen ligand levels cannot be reached for signaling pathway activation in cells that do not receive androgen deprivation therapy (ADT) and are not given additional Androgen. (Song & Khera, 2014)

In Figure 4.19, the addition of synthetic androgen R1881 allows us to be sure of translocation of AR to the core in the absence of ADT. It is seen with the protein band that all androgen receptors of LNCaP cells without nanoparticle addition are translocated

from the cytoplasm to the nucleus during the 24-hour R1881 administration. In treating LNCaP cells with DMSO, DMSO induces a reduction in R1881-promoted AR translocation; in the cytoplasm (less dense) and nucleus (denser), but the translocation appears to occur at a certain level. In ZIF-8 bands, an increase is observed in the level of androgen receptor, and the level of androgen receptor translocation thought to be related to it, compared to the control. A certain amount of non-translocated androgen receptors present in LNCaP cells treated with ZIF-8; despite the increased amount of AR, it is similar to DMSO application in the amount of cytoplasmic AR. In APA@ZIF-8 bands, it has been demonstrated that LNCaP cells achieve a considerable increase in AR protein expression levels. This increase corresponds to both the highest intra-nuclear androgen receptor and the highest intra-cytoplasmic androgen receptor compared to other R1881 addition results. APA@ZIF-8 appears to perform an inhibition that allows the AR protein to remain in the cytoplasm compared to ZIF-8. When compared to apalutamide and bicalutamide, it is observed that apalutamide allows less translocation of androgen receptors than bicalutamide. This finding can be explained by the fact that apalutamide has a higher affinity for AR than bicalutamide, reported in the literature(Rice, Malhotra, & Stoyanova, 2019).

According to Figure 4.19b, in the absence of synthetic Androgen, all androgen receptors of LNCaP cells are localized in the cytoplasm. Since the expression of the β-actin protein is more specific than ideal in all cells, androgen receptor protein expression is likely to exhibit a similar extreme profile. In DMSO bands, it is seen that AR is found only in the cytoplasm and does not pass into the nucleus. Nuclear translocation is observed, although the ZIF-8 addition was low in LNCaP cells compared to the control group and DMSO. However, it does not change that most AR remains in the cytoplasm despite the addition of ZIF-8. In samples without R1881, the effect of APA and APA@ZIF-8 has been displayed in the cytoplasm as dense protein expression whose translocation is blocked. It is understood from the density of the western blot band that the androgen receptor in the APA@ZIF-8 treated LNCaP cell line has risen above normal levels. In addition, it was observed that most of them were blocked in the cytoplasm, except for the presence of deficient protein levels in the nucleus. The androgen receptor concentration in the cytoplasm in the administration of apalutamide without R1881 also proves the drug efficacy. This suggests the possibility that APA@ZIF-8 induced

androgen receptor synthesis. In addition, the androgen receptor inducing agent may be the APA@ZIF-8 administered to the cell.

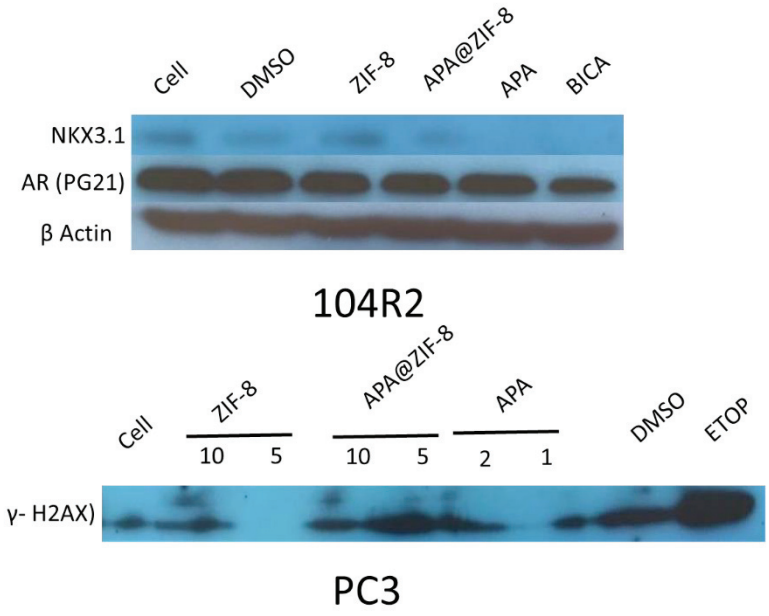

Figure 4.20. Western blot analysis was done for LNCaP104R2, and PC3 cells treated with 10 µg/mL ZIF-8, 10 µg/mL APA@ZIF-8, 2 µg/mL APA, 4µM Bica, and DMSO for 24 hours.

Figure 4.20 shows the protein determinations of the 104R2 cell line for NKX3.1 and AR (PG21) antibodies. NKX3.1 is a prostate-specific gene encoding a transcription factor vital in prostate development and carcinogenesis. Expression of mammalian NKX3.1 is androgen-dependent and is often reduced or lost in prostate cancer (Bowen & Gelmann, 2010). Since most prostate cancer cells have NKX3.1 suppressed expression, there are weak protein bands in drug-free, and ZIF-8 treated cells. It can be inferred that none of the apalutamide, APA@ZIF-8, and bicalutamide administered to 104R2 cells triggered NKX3.1 expression and thus were not involved in any NKX3.1 related signaling pathway (Bowen et al., 2000). It is determined in the literature that apalutamide and bicalutamide do not cause DNA damage. Therefore, the possibility of androgen antagonists causing possible DNA damage identified by different indicators and activated by pathways is considered. AR western blot results of 104R2, which are androgen-independent LNCaP cells, were positive in all applications, with the highest band density available for drug-free and DMSO-treated samples. The reason why androgen translocation inhibitors, apalutamide, and bicalutamide, showed lower levels of androgen

protein expression than the control group is that these drugs have a low level of androgen receptor degradation roles in addition to their inhibitory function. In addition, possible androgen receptor degradation due to low levels of androgen receptors was observed more in bicalutamide than apalutamide. On the other hand, when apalutamide was administered to lower 104R2 cells in ZIF-8, no significant dose-related decrease or increase in AR was observed.

γ-H2AX is a fast and effective double-stranded DNA damage (DSB), and repair marker (Sharma, Singh, & Almasan, 2012) used to determine whether ZIF-8 or apalutamide causes possible DNA damage. PC3 cells not expressing the androgen receptor and PSA show double-stranded DNA damage indicated by the presence of the γ-H2AX protein. This may reveal whether apalutamide is driven by the ZIF-8 transport complex, drug-loaded transport system other than its androgen receptor antagonist effect, or a pathway in which apalutamide plays a role other than the androgen antagonist not previously reported. (Tai et al., 2011). Etoposide is an FDA-approved double-stranded DNA-breaker anticancer agent. (Montecucco, Zanetta, & Biamonti, 2015). Therefore, if any of the agents caused double-stranded DNA damage, it was used as a positive control to compare the presence and extent of this damage. Etoposide appears to have a low level of γ-H2AX expression in PC3 cells, hence the presence of double-stranded DNA damage. It is seen that 5 μg/mL ZIF-8 eliminates the existing DNA damage in PC3 cells, but at 10 μg/mL concentrations, DNA damage is more significant than the negative control. This result shows that zinc, which is released by the degradation of ZIF-8 in the cell, repairs DNA damage in a certain amount at low doses, but this effect causes double-stranded DNA damage at high doses. On the other hand, DMSO appears to cause double-stranded DNA damage due to the highest γ-H2AX expression after etoposide. When the results of γ-H2AX at 1 and 2 μg/mL concentrations of apalutamide were examined, the drug did not cause DNA damage of the PC3 cell line at 1 μg/mL concentration. However, DNA damage increased slightly at 2 μg/mL concentration. The expression of γ-H2AX exhibited by apalutamide at 2 μg/mL concentration is considerably lower in the DMSO and etoposide bands. APA@ZIF-8 at 5 and 10 μg/mL concentrations causes more γ-H2AX-labeled DNA damage at lower concentrations, and this DSB tends to decrease when the dose is increased. This was due to DNA damage thought to have been caused by 48% encapsulated apalutamide per unit ZIF-8; It can be explained by the fact that the contribution of ZIF-8 released zinc to DNA repair outweighs the DNA damage effect

within the concentration of apalutamide, which degrades in the system as the total concentration of the complex increases.

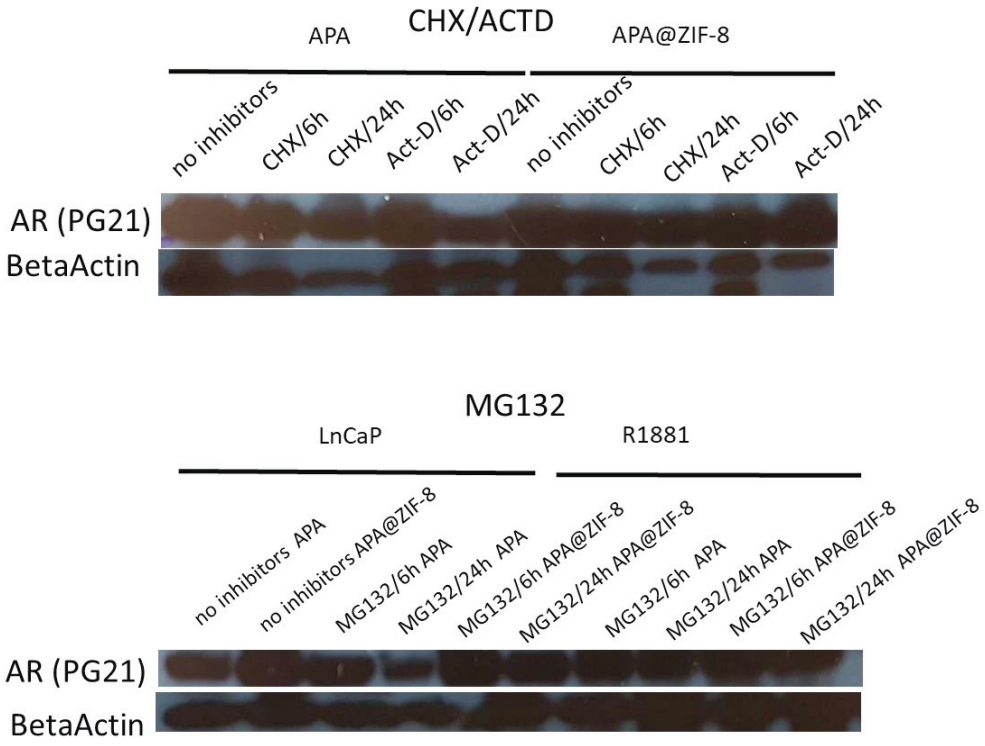

Figure 4.21. Western blot analysis was done for LNCaP and LNCaP R1881+ cells CHX, ACTD and MG132 treated with 10 µg/mL APA@ZIF-8, 2 µg/mL APA, and DMSO for 6 and 24 hours

The reason to focus solely on AR is that it has significant importance for Androgen and its receptors on the progression, prevention, and treatment of PCa in the form of androgen deprivation therapy(Huang et al., 2018). The androgen receptor is a transcription factor, so its translocation is crucial for its role. AR is present in the cytosol in the absence of AR in androgen-sensitive cells, and the Androgen triggers AR to migrate towards the nucleus.

AR protein stability also affects AR activity. Overexpression of the androgen receptor has been found to stimulate androgen-sensitive cells to become castration-resistant prostate cancer cells (CRPC), and the disease continues to progress despite androgen deprivation therapy(Egerdie & Saad, 2010; Zhenlang Guo et al., 2018).

Cycloheximide (CHX) "inhibits de novo protein synthesis" (Zhenlang Guo et al., 2018), blocks protein synthesis(Huang et al., 2018). The use aims to determine the effect of Apalutamide/APA@ZIF-8 on AR stability. The effect of triptolide on AR protein stability by blocking protein synthesis with cycloheximide (CHX) was investigated by western blot assay(Huang et al., 2018). As a known inhibitor of protein synthesis, CHX gradually decreased the amount of total protein, as can be seen from the CHX/beta-actin western result of both APA and APA@ZIF-8 treatments. AR appears to be less affected by CHX synthesis inhibition in both APA and APA@ZIF-8 treatments. In the presence of Androgen, APA@ZIF-8 produced a slightly higher reduction compared to the addition of APA. The decrease in the presence of AR protein is gradually increased over incubation times from 6 hours to 24 hours. This western result concluded that apalutamide adversely affects AR stability, and our delivery system enhances this detrimental effect.

MG132 is a proteasome inhibitor. The ubiquitin-proteasome system is responsible for protein degradation and thus maintains protein balance regulation. MG132 is reported to increase endogenous AR and poly-ubiquitin AR levels in LNCaP and HepG2 cells(Santo et al., 2012).

The intended use of MG132 is to check the effect of APA@ZIF-8 on AR protein level after inhibiting the ubiquitin-proteasome system, whether APA@ZIF-8 causes AR degradation. If AR protein levels remained the same, this would mean that AR degradation in previous results would mean that APA@ZIF-8 was acting as a ubiquitination agent; if protein degradation were observed, this would indicate that APA@ZIF-8 was impaired. AR, through another mechanism, knowing that MG132 is a proteasome inhibitor, the expected result is to observe an increase in AR availability throughout the incubation period with the inhibitor. Two duplicate results are available for the effect of both APA and APA@ZIF-8 on AR in the presence of MG132. The first group (left) shows that AR presence remains unchanged despite suppression of ubiquity. The second group (right) is associated with the literature where the presence of AR is increased in response to inhibition of protein ubiquitination, and thus more AR is present. In this latter result, the presence of AR gradually increases throughout the incubation period; APA@ZIF-8 and APA do not inhibit the protein ubiquitination inhibition mechanism with MG132.

As androgen antagonists, both enzalutamide and bicalutamide induce telomere damage, unlike etoposide, which causes genome-wide DNA damage(Ghandi et al., 2019). Therefore, apalutamide is suspected of causing DNA damage at telomeres.

Telomere targeting AR antagonists is promising for CRPC variants(Ghandi et al., 2019). This study suggests that the AR antagonist can kill PCa by destroying telomeres other than transcriptional inhibition. Actinomycin D is known to intercalate with DNA to inhibit transcription (mRNA synthesis)(Liu & Cao, 2016). The purpose of using Act D is to investigate whether the effect of the APA@ZIF-8 complex on AR is transcriptional inhibition. APA treatment, 6 h and 24 h addition of Act D inhibitor appear to reduce the presence of AR, thus supporting AR degradation as independent inhibition of AR transcription. Where APA is delivered via the ZIF-8 delivery system, AR levels remain unchanged regardless of the incubation period with the Act D inhibitor. The APA and APA@ZIF-8 Act D western did not provide a consistent result.

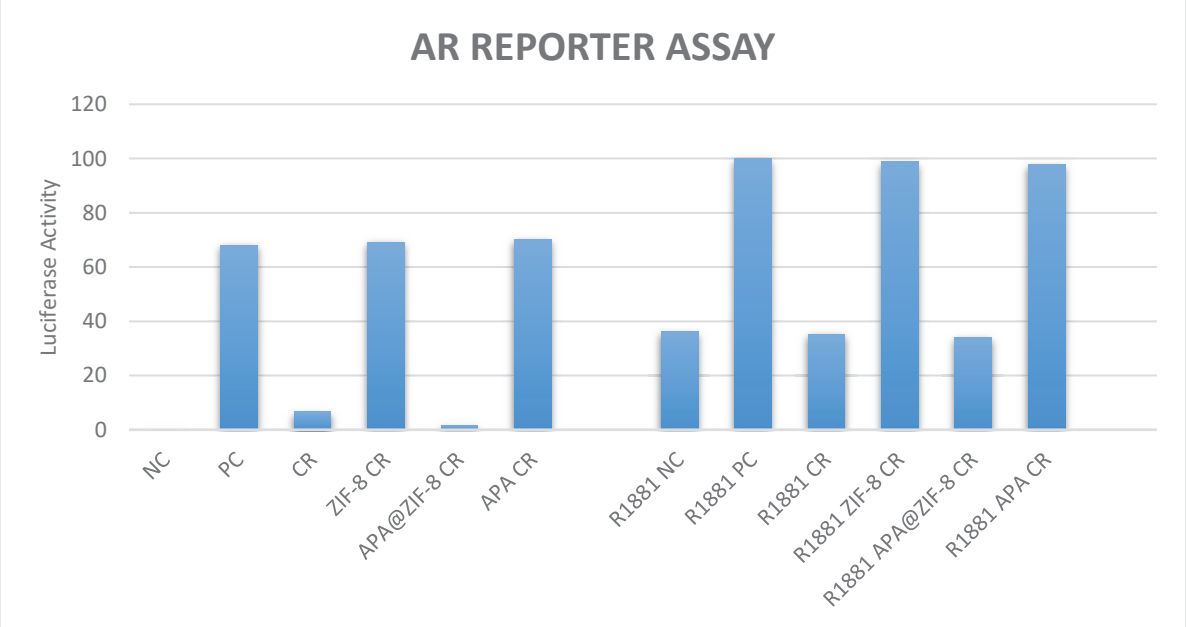

Figure 4.22. Transcriptional activity of AR as assessed by luciferase reporter gene assays.

The luciferase assay is an analysis that investigates whether a protein of interest increases or decreases transcription(Smale, 2010). With the application of the luciferase assay, we aim to check whether androgen receptor transcription is affected by apalutamide or there is APA@ZIF-8 entry into LNCaP cells with or without R1881.

The luciferase activity seen in the graph indicates the transcriptional activity of the androgen receptor within the gene construct. In the absence of R1881, neither ZIF-8

nor apalutamide seems to mediate the reduction of AR transcription, as can be seen from their relative values in the PC environment. In contrast, once apalutamide was administered to cells encapsulated with ZIF-8, APA@ZIF-8, luciferase activity and associated AR transcription appear to be reduced near negative control/signal reporter levels.

The addition of synthetic Androgen appears to significantly increase luciferase activity and androgen receptor transcription compared with non-R1881 variants. This can be seen with the concomitant increase of negative control(NC), positive control (PC), and experimental values in luciferase activity. Similar to previous non-R1881 examples, the addition of R1881 did not significantly change AR transcription in the apalutamide and ZIF-8 applications. Regardless, APA@ZIF-8 was able to reduce AR transcription when R1881 was present with relative values.

Our findings show that R1881 increases AR transcription. ZIF-8 and apalutamide have no individual effect on AR transcription. APA@ZIF-8 has significant AR transcription reduction with or without R1881, according to our luciferase assay findings. This phenomenon is hypothesized to occur by endocytosis of the ZIF-8 nanoparticle to the nuclear envelope and degradation in the nucleus rather than the cytosol. Disruption of ZIF-8 would have released apalutamide into the nucleus. As an AR antagonist, apalutamide invades the AR within the nucleus to prevent it from joining the AR transcription machinery. In conclusion, this finding suggests that apalutamide may have an intranuclear AR transcription reduction activity in addition to the already known androgen receptor translocation inhibition in the cytosol.

CHAPTER 5

CONCLUSION

With this thesis, a new generation smart, biocompatible, biodegradable, and multifunctional nanocarrier system has been developed to treat hepatocellular carcinoma (HCC) and prostate cancer. This system has been characterized, and its cytotoxic effect has been investigated. In this direction, sorafenib used in HSC treatment and apalutamide in prostate treatment were encapsulated in ZIF-8 smart material formed with zinc and 2-methylimidazole. After the material obtained has been characterized structurally and functionally in detail, the effects of the new molecule on cancer cell lines have been investigated.

Biocompatible ZIF-8 smart material, a member of the metal-organic skeleton family, is biodegradable in an acidic environment due to its weak coordination bonds. Since cancer cells are more acidic than healthy cells, sorafenib encapsulated in ZIF-8 was released in our studies by targeting cancerous cells sensitive to pH. However, it has been determined that the drug delivery system created releases the drug faster at acidic pH, which belongs to the tumor microenvironment and is lower than physiological pH. In this case, the system will release the drug very little in the bloodstream, but more in this area when it reaches the cancer tissue. In this way, toxicity to normal tissue can be reduced.

Besides, ZIF-8 was chosen as a delivery system and for its therapeutic and treatment-supporting effect. Because ZIF-8 material is divided into zinc and 2-methylimidazole components in cancer cells with its biodegradable structure, studies show that the decrease in the amount of zinc is vital in forming cancerous cells. It is known that the accumulation of zinc in cancerous areas in HCC and prostate stop cancer progression. Thanks to the ZIF-8 metal-organic skeleton selected within the project, it was aimed to create a dual cytotoxic effect by combining the effects of zinc and drug on a single platform.

The ZIF-8 nanocarrier system was synthesized with the one-pot method. Characterization studies were carried out after all necessary optimizations were made. SEM images showed that the particles were homogeneously distributed, and the structure was rhombic dodecahedral; the zeta potential results were negatively charged and thus

suitable for targeting. The crystallinity and impurity of nanoparticles were determined by XRD measurement. In addition, FTIR results confirmed the structure. Subsequent in vitro release and cytotoxicity studies demonstrated the potential of the nanoparticle system.

As a result of this study, the findings showed that a formulation combining zinc and drugs was more effective on cancer treatment. With the in vivo studies planned to be carried out in the continuation of the project, it is aimed to show that this formulation has a targeted transport.

REFERENCES

Abdelhamid, H. N., Huang, Z., El-Zohry, A. M., Zheng, H., & Zou, X. (2017). A fast and scalable approach for synthesis of hierarchical porous zeolitic imidazolate frameworks and one-pot encapsulation of target molecules. Inorganic chemistry, 56(15), 9139-9146.

Adhikari, C., Das, A., & Chakraborty, A. (2015). Zeolitic imidazole framework (ZIF) nanospheres for easy encapsulation and controlled release of an anticancer drug doxorubicin under different external stimuli: a way toward smart drug delivery system. Molecular pharmaceutics, 12(9), 3158-3166.

Al-Salama, Z. T. (2018). Apalutamide: First Global Approval. Drugs, 78(6), 699-705. doi:10.1007/s40265-018-0900-z

Alavi, M., & Hamidi, M. (2019). Passive and active targeting in cancer therapy by liposomes and lipid nanoparticles. Drug metabolism and personalized therapy, 34(1).

Altekruse, S. F., McGlynn, K. A., Dickie, L. A., & Kleiner, D. E. (2012). Hepatocellular carcinoma confirmation, treatment, and survival in surveillance, epidemiology, and end results registries, 1992-2008. Hepatology, 55(2), 476-482. doi:10.1002/hep.24710

Apostolova, N., & Victor, V. M. (2015). Molecular strategies for targeting antioxidants to mitochondria: therapeutic implications. Antioxid Redox Signal, 22(8), 686-729. doi:10.1089/ars.2014.5952

Arcamone, F., Cassinelli, G., Fantini, G., Grein, A., Orezzi, P., Pol, C., & Spalla, C. (1969). Adriamycin, 14-hydroxydaunomycin, a new antitumor antibiotic from S. peucetius var. caesius. Biotechnol Bioeng, 11(6), 1101-1110. doi:10.1002/bit.260110607

Arora, C., Soni, S., Sahu, S., Mittal, J., Kumar, P., & Bajpai, P. (2019). Iron based metal organic framework for efficient removal of methylene blue dye from industrial waste. Journal of Molecular Liquids, 284, 343-352.

Awan, F. M., Naz, A., Obaid, A., Ikram, A., Ali, A., Ahmad, J., . . . Janjua, H. A. (2017). MicroRNA pharmacogenomics based integrated model of miR-17-92 cluster in sorafenib resistant HCC cells reveals a strategy to forestall drug resistance. Scientific Reports, 7(1), 1-21.

Banerjee, D., Wang, H., Deibert, B. J., & Li, J. (2016). Alkaline Earth Metal-Based Metal–Organic Frameworks: Synthesis, Properties, and Applications. The Chemistry of Metal–Organic Frameworks: Synthesis, Characterization, and Applications, 1, 73-103.

Banerjee, R., Furukawa, H., Britt, D., Knobler, C., O'Keeffe, M., & Yaghi, O. M. (2009). Control of pore size and functionality in isoreticular zeolitic imidazolate frameworks and their carbon dioxide selective capture properties. Journal of the American Chemical Society, 131(11), 3875-3877.

Banudevi, S., Senthilkumar, K., Sharmila, G., Arunkumar, R., Vijayababu, M. R., & Arunakaran, J. (2010). Effect of zinc on regulation of insulin-like growth factor signaling in human androgen-independent prostate cancer cells. Clinica Chimica Acta, 411(3-4), 172-178.

Bennett, T. D., & Cheetham, A. K. (2014). Amorphous metal–organic frameworks. Accounts of chemical research, 47(5), 1555-1562.

Bieniek, A., Terzyk, A. P., Wiśniewski, M., Roszek, K., Kowalczyk, P., Sarkisov, L., . . . Kaneko, K. (2021). MOF materials as therapeutic agents, drug carriers, imaging agents and biosensors in cancer biomedicine: Recent advances and perspectives. Progress in Materials Science, 117, 100743.

Blanchet, B., Billemont, B., Cramard, J., Benichou, A., Chhun, S., Harcouet, L., . . . Tod, M. (2009). Validation of an HPLC-UV method for sorafenib determination in human plasma and application to cancer patients in routine clinical practice. Journal of pharmaceutical and biomedical analysis, 49(4), 1109-1114.

Bowen, C., Bubendorf, L., Voeller, H. J., Slack, R., Willi, N., Sauter, G., . . . Gelmann, E. P. (2000). Loss of NKX3.1 Expression in Human Prostate Cancers Correlates with Tumor Progression^{1,2}. Cancer Research, 60(21), 6111-6115. Retrieved from https://cancerres.aacrjournals.org/content/canres/60/21/6111.full.pdf

Bowen, C., & Gelmann, E. P. (2010). NKX3.1 Activates Cellular Response to DNA Damage. Cancer Research, 70(8), 3089-3097. doi:10.1158/0008-5472.Can-09-3138

Bradford, M. M. (1976). A rapid and sensitive method for the quantitation of microgram quantities of protein utilizing the principle of protein-dye binding. Anal Biochem, 72, 248-254. doi:10.1006/abio.1976.9999

Brockmann, H. (1963). [ANTHRACYCLINONES AND ANTHRACYCLINES. (RHODOMYCINONE, PYRROMYCINONE AND THEIR GLYCOSIDES)]. Fortschr Chem Org Naturst, 21, 121-182.

Buxaderas, S. C., & Farré-Rovira, R. (1985). Whole blood and serum zinc levels in relation to sex and age. Rev Esp Fisiol, 41(4), 463-470.

Cadet, J., & Wagner, J. R. (2013). DNA base damage by reactive oxygen species, oxidizing agents, and UV radiation. Cold Spring Harbor perspectives in biology, 5(2), a012559.

Cai, W., Wang, J., Chu, C., Chen, W., Wu, C., & Liu, G. (2019a). Metal–Organic Framework-Based Stimuli-Responsive Systems for Drug Delivery. Advanced Science, 6(1), 1801526. doi:https://doi.org/10.1002/advs.201801526

Cai, W., Wang, J., Chu, C., Chen, W., Wu, C., & Liu, G. (2019b). Metal–organic framework-based stimuli-responsive systems for drug delivery. Advanced Science, 6(1), 1801526.

CANEFE, K., & DUMAN, G. (1994). Selective Drug Delivery and Targeting. Journal of Faculty of Pharmacy of Ankara University, 23(1), 53-63.

Carné, A., Carbonell, C., Imaz, I., & Maspoch, D. (2011). Nanoscale metal–organic materials. Chemical Society Reviews, 40(1), 291-305.

Caskey, S. R., Wong-Foy, A. G., & Matzger, A. J. (2008). Dramatic tuning of carbon dioxide uptake via metal substitution in a coordination polymer with cylindrical pores. Journal of the American Chemical Society, 130(33), 10870-10871.

Cavka, J. H., Jakobsen, S., Olsbye, U., Guillou, N., Lamberti, C., Bordiga, S., & Lillerud, K. P. (2008). A new zirconium inorganic building brick forming metal organic frameworks with exceptional stability. Journal of the American Chemical Society, 130(42), 13850-13851.

Chen, B., Yang, Z., Zhu, Y., & Xia, Y. (2014). Zeolitic imidazolate framework materials: recent progress in synthesis and applications. Journal of Materials Chemistry A, 2(40), 16811-16831.

Chen, F., Drake, H. F., Feng, L., Powell, J. A., Wang, K.-Y., Yan, T.-H., & Zhou, H.-C. (2021). Metal–Organic Frameworks as Versatile Platforms for Organometallic Chemistry. Inorganics, 9(4), 27. Retrieved from https://www.mdpi.com/2304-6740/9/4/27

Chen, W. H., Luo, G. F., Vázquez-González, M., Cazelles, R., Sohn, Y. S., Nechushtai, R., . . . Willner, I. (2018). Glucose-Responsive Metal-Organic-Framework Nanoparticles Act as "Smart" Sense-and-Treat Carriers. ACS nano, 12(8), 7538-7545. doi:10.1021/acsnano.8b03417

Cheng, A.-L., Kang, Y.-K., Chen, Z., Tsao, C.-J., Qin, S., Kim, J. S., . . . Yang, T.-S. (2009). Efficacy and safety of sorafenib in patients in the Asia-Pacific region with advanced hepatocellular carcinoma: a phase III randomised, double-blind, placebo-controlled trial. The lancet oncology, 10(1), 25-34.

Cheng, Y., Kondo, A., Noguchi, H., Kajiro, H., Urita, K., Ohba, T., . . . Kanoh, H. (2009). Reversible structural change of Cu-MOF on exposure to water and its CO2 adsorptivity. Langmuir, 25(8), 4510-4513.

Cho, H.-Y., Kim, J., Kim, S.-N., & Ahn, W.-S. (2013). High yield 1-L scale synthesis of

ZIF-8 via a sonochemical route. Microporous and Mesoporous Materials, 169, 180-184.

Choueiri, T. K., Duh, M. S., Clement, J., Brick, A. J., Rogers, M. J., Kwabi, C., . . . Jayawant, S. S. (2010). Angiogenesis inhibitor therapies for metastatic renal cell carcinoma: effectiveness, safety and treatment patterns in clinical practice-based on medical chart review. BJU international, 105(9), 1247-1254.

Chouhan, R., & Bajpai, A. (2009). Real time in vitro studies of doxorubicin release from PHEMA nanoparticles. Journal of nanobiotechnology, 7(1), 5.

Chu, Y., Hou, J., Boyer, C., Richardson, J. J., Liang, K., & Xu, J. (2018). Biomimetic synthesis of coordination network materials: Recent advances in MOFs and MPNs. Applied Materials Today, 10, 93-105. doi:https://doi.org/10.1016/j.apmt.2017.12.009

Chui, S. S.-Y., Lo, S. M.-F., Charmant, J. P., Orpen, A. G., & Williams, I. D. (1999). A chemically functionalizable nanoporous material [Cu3 (TMA) 2 (H2O) 3] n. Science, 283(5405), 1148-1150.

Clegg, N. J., Wongvipat, J., Joseph, J. D., Tran, C., Ouk, S., Dilhas, A., . . . Cai, L. (2012). ARN-509: a novel antiandrogen for prostate cancer treatment. Cancer research, 72(6), 1494-1503.

Cooke, M. S., Evans, M. D., Dizdaroglu, M., & Lunec, J. (2003). Oxidative DNA damage: mechanisms, mutation, and disease. The FASEB Journal, 17(10), 1195-1214.

Costello, L. C., & Franklin, R. B. (2006). The clinical relevance of the metabolism of prostate cancer; zinc and tumor suppression: connecting the dots. Molecular cancer, 5(1), 1-13.

Costello, L. C., & Franklin, R. B. (2012). Cytotoxic/tumor suppressor role of zinc for the treatment of cancer: an enigma and an opportunity. Expert review of anticancer therapy, 12(1), 121-128.

Costello, L. C., & Franklin, R. B. (2017). Decreased zinc in the development and progression of malignancy: an important common relationship and potential for prevention and treatment of carcinomas. Expert opinion on therapeutic targets, 21(1), 51-66.

Cravillon, J., Münzer, S., Lohmeier, S.-J., Feldhoff, A., Huber, K., & Wiebcke, M. (2009). Rapid room-temperature synthesis and characterization of nanocrystals of a prototypical zeolitic imidazolate framework. Chemistry of Materials, 21(8), 1410-1412.

Cui, W., Li, X., Zhu, X., Yu, G., Zhou, S., & Weng, J. (2006). Investigation of Drug

Release and Matrix Degradation of Electrospun Poly(dl-lactide) Fibers with Paracetanol Inoculation. Biomacromolecules, 7(5), 1623-1629. doi:10.1021/bm060057z

Devlin, H.-L., & Mudryj, M. (2009). Progression of prostate cancer: multiple pathways to androgen independence. Cancer letters, 274(2), 177-186.

Dey, C., Kundu, T., Biswal, B. P., Mallick, A., & Banerjee, R. (2014). Crystalline metal-organic frameworks (MOFs): synthesis, structure and function. Acta Crystallographica Section B: Structural Science, Crystal Engineering and Materials, 70(1), 3-10.

Dimitroulis, D., Damaskos, C., Valsami, S., Davakis, S., Garmpis, N., Spartalis, E., . . . Kykalos, S. (2017). From diagnosis to treatment of hepatocellular carcinoma: An epidemic problem for both developed and developing world. World journal of gastroenterology, 23(29), 5282.

Dong, K., Wang, Z., Zhang, Y., Ren, J., & Qu, X. (2018). Metal-Organic Framework-Based Nanoplatform for Intracellular Environment-Responsive Endo/Lysosomal Escape and Enhanced Cancer Therapy. ACS Appl Mater Interfaces, 10(38), 31998-32005. doi:10.1021/acsami.8b11972

Dong, X., & Mumper, R. J. (2010). Nanomedicinal strategies to treat multidrug-resistant tumors: current progress. Nanomedicine, 5(4), 597-615.

Duan, Y., Ye, F., Huang, Y., Qin, Y., He, C., & Zhao, S. (2018). One-pot synthesis of a metal–organic framework-based drug carrier for intelligent glucose-responsive insulin delivery. Chemical Communications, 54(42), 5377-5380.

Egerdie, B., & Saad, F. (2010). Bone health in the prostate cancer patient receiving androgen deprivation therapy: a review of present and future management options. Canadian Urological Association Journal, 4(2), 129.

Ekin, R. G., & Zorlu, F. (2013). Türkiye verilerine göre prostat kanseri taranmalı mı? Üroonkoloji Bülteni, 12, 71-75.

Fagin, J. A., & Wells Jr, S. A. (2016). Biologic and clinical perspectives on thyroid cancer. New England journal of medicine, 375(11), 1054-1067.

Fang, J., Nakamura, H., & Maeda, H. (2011). The EPR effect: unique features of tumor blood vessels for drug delivery, factors involved, and limitations and augmentation of the effect. Advanced drug delivery reviews, 63(3), 136-151.

Feng, P., Liang, J., Li, T., Guan, Z., Zou, J., Franklin, R., and, & Costello, L. C. (2000). Zinc induces mitochondria apoptogenesis in prostate cells. Molecular urology, 4(1).

Feng, Y., Li, Y., Xu, M., Liu, S., & Yao, J. (2016). Fast adsorption of methyl blue on

zeolitic imidazolate framework-8 and its adsorption mechanism. RSC Advances, 6(111), 109608-109612. doi:10.1039/C6RA23870J

Ferdous, Z., & Nemmar, A. (2020). Health Impact of Silver Nanoparticles: A Review of the Biodistribution and Toxicity Following Various Routes of Exposure. International journal of molecular sciences, 21(7), 2375. doi:10.3390/ijms21072375

Ferlay, J., Shin, H. R., Bray, F., Forman, D., Mathers, C., & Parkin, D. M. (2010). Estimates of worldwide burden of cancer in 2008: GLOBOCAN 2008. Int J Cancer, 127(12), 2893-2917. doi:10.1002/ijc.25516

Florczak, P., Janiszewska, E., Kędzierska, K., & Kowalak, S. (2011). Materiały MOF, nowa rodzina sit molekularnych o niezwykłych właściwościach i możliwościach zastosowań. Wiadomości Chemiczne, 427-460.

Fong, Z. V., & Tanabe, K. K. (2014). The clinical management of hepatocellular carcinoma in the United States, Europe, and Asia: a comprehensive and evidence-based comparison and review. Cancer, 120(18), 2824-2838. doi:10.1002/cncr.28730

Fornari, F. A., Randolph, J. K., Yalowich, J. C., Ritke, M. K., & Gewirtz, D. A. (1994). Interference by doxorubicin with DNA unwinding in MCF-7 breast tumor cells. Mol Pharmacol, 45(4), 649-656.

Freshney, N. W., Rawlinson, L., Guesdon, F., Jones, E., Cowley, S., Hsuan, J., & Saklatvala, J. (1994). Interleukin-1 activates a novel protein kinase cascade that results in the phosphorylation of Hsp27. cell, 78(6), 1039-1049.

Furukawa, H., Cordova, K. E., O'Keeffe, M., & Yaghi, O. M. (2013). The chemistry and applications of metal-organic frameworks. Science, 341(6149).

Gai, S., Yang, G., Yang, P., He, F., Lin, J., Jin, D., & Xing, B. (2018). Recent advances in functional nanomaterials for light–triggered cancer therapy. Nano Today, 19, 146-187. doi:https://doi.org/10.1016/j.nantod.2018.02.010

Gao, D.-Y., Lin, T.-T., Sung, Y.-C., Liu, Y. C., Chiang, W.-H., Chang, C.-C., . . . Chen, Y. (2015). CXCR4-targeted lipid-coated PLGA nanoparticles deliver sorafenib and overcome acquired drug resistance in liver cancer. Biomaterials, 67, 194-203.

Gao, L., Chen, Q., Gong, T., Liu, J., & Li, C. (2019). Recent advancement of imidazolate framework (ZIF-8) based nanoformulations for synergistic tumor therapy. Nanoscale, 11(44), 21030-21045.

Ghandi, M., Huang, F. W., Jané-Valbuena, J., Kryukov, G. V., Lo, C. C., McDonald, E. R., . . . Li, H. (2019). Next-generation characterization of the cancer cell line encyclopedia. nature, 569(7757), 503-508.

Gleiter, H. (2000). Nanostructured materials: basic concepts and microstructure. Acta

materialia, 48(1), 1-29.

Gonzalez, A., Peters, U., Lampe, J. W., & White, E. (2009). Zinc intake from supplements and diet and prostate cancer. Nutrition and cancer, 61(2), 206-215.

Gu, M., Wang, X., Toh, T. B., Hooi, L., Tenen, D. G., & Chow, E. K. H. (2018). Nanodiamond-Based Platform for Intracellular-Specific Delivery of Therapeutic Peptides against Hepatocellular Carcinoma. Advanced Therapeutics, 1(8), 1800110.

Guo, Z., Huang, Y., Gong, L., Gan, S., Chan, F. L., Gu, C., . . . Wang, S. (2018). Association of androgen deprivation therapy with thromboembolic events in patients with prostate cancer: a systematic review and meta-analysis. Prostate cancer and prostatic diseases, 21(4), 451-460.

Guo, Z., Yang, X., Sun, F., Jiang, R., Linn, D. E., Chen, H., . . . Tepper, C. G. (2009). A novel androgen receptor splice variant is up-regulated during prostate cancer progression and promotes androgen depletion–resistant growth. Cancer research, 69(6), 2305-2313.

Hanahan, D., & Weinberg, R. A. (2011). Hallmarks of cancer: the next generation. cell, 144(5), 646-674.

Harshman, L. C., Xie, W., Bjarnason, G. A., Knox, J. J., MacKenzie, M., Wood, L., . . . Rha, S.-Y. (2012). Conditional survival of patients with metastatic renal-cell carcinoma treated with VEGF-targeted therapy: a population-based study. The lancet oncology, 13(9), 927-935.

He, C., Liu, D., & Lin, W. (2015). Nanomedicine applications of hybrid nanomaterials built from metal–ligand coordination bonds: nanoscale metal–organic frameworks and nanoscale coordination polymers. Chemical reviews, 115(19), 11079-11108.

Hoop, M., Walde, C. F., Riccò, R., Mushtaq, F., Terzopoulou, A., Chen, X.-Z., . . . Nelson, B. J. (2018). Biocompatibility characteristics of the metal organic framework ZIF-8 for therapeutical applications. Applied Materials Today, 11, 13-21.

Horcajada, P., Chalati, T., Serre, C., Gillet, B., Sebrie, C., Baati, T., . . . Kreuz, C. (2010). Porous metal–organic-framework nanoscale carriers as a potential platform for drug delivery and imaging. Nature materials, 9(2), 172-178.

Horcajada, P., Gref, R., Baati, T., Allan, P. K., Maurin, G., Couvreur, P., . . . Serre, C. (2012). Metal–organic frameworks in biomedicine. Chemical reviews, 112(2), 1232-1268.

Horcajada, P., Serre, C., Maurin, G., Ramsahye, N. A., Balas, F., Vallet-Regi, M., . . . Férey, G. (2008). Flexible porous metal-organic frameworks for a controlled drug delivery. Journal of the American Chemical Society, 130(21), 6774-6780.

Horcajada, P., Serre, C., Vallet-Regí, M., Sebban, M., Taulelle, F., & Férey, G. (2006). Metal–organic frameworks as efficient materials for drug delivery. Angewandte chemie, 118(36), 6120-6124.

Horcajada, P., Surblé, S., Serre, C., Hong, D.-Y., Seo, Y.-K., Chang, J.-S., . . . Férey, G. (2007). Synthesis and catalytic properties of MIL-100 (Fe), an iron (III) carboxylate with large pores. Chemical Communications(27), 2820-2822.

Hourdequin, K., Schpero, W., McKenna, D., Piazik, B., & Larson, R. (2013). Toxic effect of chemotherapy dosing using actual body weight in obese versus normal-weight patients: a systematic review and meta-analysis. Annals of Oncology, 24(12), 2952-2962.

Howarth, A. J., Peters, A. W., Vermeulen, N. A., Wang, T. C., Hupp, J. T., & Farha, O. K. (2017). Best practices for the synthesis, activation, and characterization of metal–organic frameworks. Chemistry of Materials, 29(1), 26-39.

Hu, L., Zhang, P., Chen, Q., Zhong, H., Hu, X., Zheng, X., . . . Yan, N. (2012). Morphology-Controllable Synthesis of Metal Organic Framework Cd3[Co(CN)6]2·nH2O Nanostructures for Hydrogen Storage Applications. Crystal Growth & Design, 12(5), 2257-2264. doi:10.1021/cg2014896

Hua, K.-F., Liao, P.-C., Fang, Z., Yang, F.-L., Yang, Y.-L., Chen, Y.-L., . . . Wu, S.-H. (2013). Generation of reactive oxygen species by polyenylpyrroles derivatives causes DNA damage leading to G2/M arrest and apoptosis in human oral squamous cell carcinoma cells. PloS one, 8(6), e67603.

Huang, H., Wang, C., Liu, F., Li, H.-Z., Peng, G., Gao, X., . . . Qu, M. (2018). Reciprocal network between cancer stem-like cells and macrophages facilitates the progression and androgen deprivation therapy resistance of prostate cancer. Clinical cancer research, 24(18), 4612-4626.

Huxford, R. C., Della Rocca, J., & Lin, W. (2010). Metal–organic frameworks as potential drug carriers. Current opinion in chemical biology, 14(2), 262-268.

Jemal, A., Bray, F., Center, M. M., Ferlay, J., Ward, E., & Forman, D. (2011). Global cancer statistics. CA Cancer J Clin, 61(2), 69-90. doi:10.3322/caac.20107

Joseph, E., & Singhvi, G. (2019). Chapter 4 - Multifunctional nanocrystals for cancer therapy: a potential nanocarrier. In A. M. Grumezescu (Ed.), Nanomaterials for Drug Delivery and Therapy (pp. 91-116): William Andrew Publishing.

Kanoh, H., Kondo, A., Noguchi, H., Kajiro, H., Tohdoh, A., Hattori, Y., . . . Morita, K. (2009). Elastic layer-structured metal organic frameworks (ELMs). Journal of colloid and interface science, 334(1), 1-7.

Karagiaridi, O., Lalonde, M. B., Bury, W., Sarjeant, A. A., Farha, O. K., & Hupp, J. T.

(2012). Opening ZIF-8: a catalytically active zeolitic imidazolate framework of sodalite topology with unsubstituted linkers. Journal of the American Chemical Society, 134(45), 18790-18796.

Kaskel, S. (2016). The Chemistry of Metal-Organic Frameworks, 2 Volume Set: Synthesis, Characterization, and Applications (Vol. 1): John Wiley & Sons.

Kaur, H., Mohanta, G. C., Gupta, V., Kukkar, D., & Tyagi, S. (2017). Synthesis and characterization of ZIF-8 nanoparticles for controlled release of 6-mercaptopurine drug. Journal of Drug Delivery Science and Technology, 41, 106-112.

Kayser, O., Lemke, A., & Hernandez-Trejo, N. (2005). The impact of nanobiotechnology on the development of new drug delivery systems. Current pharmaceutical biotechnology, 6(1), 3-5.

Khan, I., Joshi, G., Nakhate, K. T., Kumar, R., & Gupta, U. (2019). Nano-co-delivery of berberine and anticancer drug using PLGA nanoparticles: Exploration of better anticancer activity and in vivo Kinetics. Pharmaceutical research, 36(10), 1-17.

Khan, M. A., Raza, A., Ovais, M., Sohail, M. F., & Ali, S. (2018). Current state and prospects of nano-delivery systems for sorafenib. International Journal of Polymeric Materials and Polymeric Biomaterials, 67(18), 1105-1115.

Kondo, A., Chinen, A., Kajiro, H., Nakagawa, T., Kato, K., Takata, M., . . . Kaneko, K. (2009). Metal-Ion-Dependent Gas Sorptivity of Elastic Layer-Structured MOFs. Chemistry–A European Journal, 15(31), 7549-7553.

Kondo, A., Kajiro, H., Noguchi, H., Carlucci, L., Proserpio, D. M., Ciani, G., . . . Sakamoto, M. (2011). Super flexibility of a 2D Cu-based porous coordination framework on gas adsorption in comparison with a 3D framework of identical composition: framework dimensionality-dependent gas adsorptivities. Journal of the American Chemical Society, 133(27), 10512-10522.

Kong, F.-H., Ye, Q.-F., Miao, X.-Y., Liu, X., Huang, S.-Q., Xiong, L., . . . Zhang, Z.-J. (2021). Current status of sorafenib nanoparticle delivery systems in the treatment of hepatocellular carcinoma. Theranostics, 11(11), 5464.

Koukourakis, M. I., Kakouratos, C., Kalamida, D., Mitrakas, A., Pouliliou, S., Xanthopoulou, E., . . . Giatromanolaki, A. (2018). Comparison of the effect of the antiandrogen apalutamide (ARN-509) versus bicalutamide on the androgen receptor pathway in prostate cancer cell lines. Anti-cancer drugs, 29(4), 323-333.

Kreno, L. E., Leong, K., Farha, O. K., Allendorf, M., Van Duyne, R. P., & Hupp, J. T. (2012). Metal–organic framework materials as chemical sensors. Chemical reviews, 112(2), 1105-1125.

Kuppler, R. J., Timmons, D. J., Fang, Q.-R., Li, J.-R., Makal, T. A., Young, M. D., . . .

Zhou, H.-C. (2009). Potential applications of metal-organic frameworks. Coordination Chemistry Reviews, 253(23), 3042-3066. doi:https://doi.org/10.1016/j.ccr.2009.05.019

Lee, D.-E., Koo, H., Sun, I.-C., Ryu, J. H., Kim, K., & Kwon, I. C. (2012). Multifunctional nanoparticles for multimodal imaging and theragnosis. Chemical Society Reviews, 41(7), 2656-2672.

Lee, Y.-R., Jang, M.-S., Cho, H.-Y., Kwon, H.-J., Kim, S., & Ahn, W.-S. (2015). ZIF-8: A comparison of synthesis methods. Chemical Engineering Journal, 271, 276-280.

Leitzmann, M. F., Stampfer, M. J., Wu, K., Colditz, G. A., Willett, W. C., & Giovannucci, E. L. (2003). Zinc supplement use and risk of prostate cancer. Journal of the National Cancer Institute, 95(13), 1004-1007.

Li, D., & Kaneko, K. (2001). Hydrogen bond-regulated microporous nature of copper complex-assembled microcrystals. Chemical physics letters, 335(1-2), 50-56.

Li, H., Eddaoudi, M., O'Keeffe, M., & Yaghi, O. M. (1999). Design and synthesis of an exceptionally stable and highly porous metal-organic framework. nature, 402(6759), 276-279.

Li, M., Su, Y., Zhang, F., Chen, K., Xu, X., Xu, L., . . . Wang, W. (2018). A dual-targeting reconstituted high density lipoprotein leveraging the synergy of sorafenib and antimiRNA21 for enhanced hepatocellular carcinoma therapy. Acta biomaterialia, 75, 413-426.

Li, S., Wang, K., Shi, Y., Cui, Y., Chen, B., He, B., . . . Zhong, C. (2016). Novel Biological Functions of ZIF-NP as a Delivery Vehicle: High Pulmonary Accumulation, Favorable Biocompatibility, and Improved Therapeutic Outcome. Advanced Functional Materials, 26(16), 2715-2727.

Li, T., Chen, D.-L., Sullivan, J. E., Kozlowski, M. T., Johnson, J. K., & Rosi, N. L. (2013). Systematic modulation and enhancement of CO 2: N 2 selectivity and water stability in an isoreticular series of bio-MOF-11 analogues. Chemical Science, 4(4), 1746-1755.

Li, Y. S., Liang, F. Y., Bux, H., Feldhoff, A., Yang, W. S., & Caro, J. (2010). Inside cover: Molecular sieve membrane: Supported metal–organic framework with high hydrogen selectivity (Angew. Chem. Int. Ed. 3/2010). Angewandte Chemie International Edition, 49(3), 464-464.

Lian, X., Fang, Y., Joseph, E., Wang, Q., Li, J., Banerjee, S., . . . Zhou, H.-C. (2017). Enzyme–MOF (metal–organic framework) composites. Chemical Society Reviews, 46(11), 3386-3401. doi:10.1039/C7CS00058H

Liang, J. Y., Liu, Y. Y., Zou, J., Franklin, R. B., Costello, L. C., & Feng, P. (1999).

Inhibitory effect of zinc on human prostatic carcinoma cell growth. The Prostate, 40(3), 200-207.

Liédana, N., Galve, A., Rubio, C., Tellez, C., & Coronas, J. (2012). CAF@ ZIF-8: one-step encapsulation of caffeine in MOF. ACS Applied Materials & Interfaces, 4(9), 5016-5021.

Limeres, M. J., Moretton, M. A., Bernabeu, E., Chiappetta, D. A., & Cuestas, M. L. (2019). Thinking small, doing big: Current success and future trends in drug delivery systems for improving cancer therapy with special focus on liver cancer. Materials Science and Engineering: C, 95, 328-341.

Lin, X., Telepeni, I., Blake, A. J., Dailly, A., Brown, C. M., Simmons, J. M., . . . Mays, T. J. (2009). High capacity hydrogen adsorption in Cu (II) tetracarboxylate framework materials: the role of pore size, ligand functionalization, and exposed metal sites. Journal of the American Chemical Society, 131(6), 2159-2171.

Liu, Y., & Cao, X. (2016). Characteristics and significance of the pre-metastatic niche. Cancer cell, 30(5), 668-681.

Llovet, J. M., & Hernandez-Gea, V. (2014). Hepatocellular carcinoma: reasons for phase III failure and novel perspectives on trial design. Clinical cancer research, 20(8), 2072-2079.

Llovet, J. M., Ricci, S., Mazzaferro, V., Hilgard, P., Gane, E., Blanc, J.-F., . . . Forner, A. (2008). Sorafenib in advanced hepatocellular carcinoma. New England journal of medicine, 359(4), 378-390.

Llovet, J. M., Ricci, S., Mazzaferro, V., Hilgard, P., Gane, E., Blanc, J. F., . . . Bruix, J. (2008). Sorafenib in advanced hepatocellular carcinoma. N Engl J Med, 359(4), 378-390. doi:10.1056/NEJMoa0708857

Llovet, J. M., Schwartz, M., & Mazzaferro, V. (2005). Resection and liver transplantation for hepatocellular carcinoma. Semin Liver Dis, 25(2), 181-200. doi:10.1055/s-2005-871198

Lu, G., & Hupp, J. T. (2010). Metal− organic frameworks as sensors: a ZIF-8 based Fabry− Pérot device as a selective sensor for chemical vapors and gases. Journal of the American Chemical Society, 132(23), 7832-7833.

Lu, K., Aung, T., Guo, N., Weichselbaum, R., & Lin, W. (2018). Nanoscale Metal-Organic Frameworks for Therapeutic, Imaging, and Sensing Applications. Adv Mater, 30(37), e1707634. doi:10.1002/adma.201707634

Maleki, A., Shahbazi, M.-A., Alinezhad, V., & Santos, H. A. (2020). The Progress and Prospect of Zeolitic Imidazolate Frameworks in Cancer Therapy, Antibacterial Activity, and Biomineralization. Advanced Healthcare Materials, 9(12), 2000248.

doi:https://doi.org/10.1002/adhm.202000248

Mancuso, A., Airoldi, A., Vigano, R., & Pinzello, G. (2011). Fatal gastric bleeding during sorafenib treatment for hepatocellular carcinoma recurrence after liver transplantation. Digestive and Liver Disease, 43(9), 754.

Massie, C. E., Lynch, A., Ramos-Montoya, A., Boren, J., Stark, R., Fazli, L., . . . Sharma, N. (2011). The androgen receptor fuels prostate cancer by regulating central metabolism and biosynthesis. The EMBO journal, 30(13), 2719-2733.

Mayer, A., Vadon, M., Rinner, B., Novak, A., Wintersteiger, R., & Fröhlich, E. (2009). The role of nanoparticle size in hemocompatibility. Toxicology, 258(2-3), 139-147.

McCance, K. L., & Huether, S. E. (2018). Pathophysiology-E-book: the biologic basis for disease in adults and children: Elsevier Health Sciences.

Mengran, X. (2020). Rationally designed rapamycin-encapsulated ZIF-8 nanosystem for overcoming chemotherapy resistance. Biomaterials, v. 258, pp. 120308--122020 v.120258. doi:10.1016/j.biomaterials.2020.120308

Miyahara, T., Sueoka-Aragane, N., Iwanaga, K., Ureshino, N., Komiya, K., Nakamura, T., . . . Kimura, S. (2017). Severity and predictive factors of adverse events in pemetrexed-containing chemotherapy for non-small cell lung cancer. Medical Oncology, 34(12), 1-9.

Mo, R., & Gu, Z. (2016). Tumor microenvironment and intracellular signal-activated nanomaterials for anticancer drug delivery. Materials Today, 19(5), 274-283. doi:https://doi.org/10.1016/j.mattod.2015.11.025

Mochalova, A., & Koroleva, I. (2013). Clinical and economic analysis of the feasibility of using Dicarbamine for the prevention of the toxic effects of antineoplastic chemotherapy. Voprosy onkologii, 59(5), 637-641.

Modi, A., Verma, S. K., & Bellare, J. (2018). Hydrophilic ZIF-8 decorated GO nanosheets improve biocompatibility and separation performance of polyethersulfone hollow fiber membranes: A potential membrane material for bioartificial liver application. Materials Science and Engineering: C, 91, 524-540. doi:https://doi.org/10.1016/j.msec.2018.05.051

Modrow, A., Zargarani, D., Herges, R., & Stock, N. (2011). The first porous MOF with photoswitchable linker molecules. Dalton transactions, 40(16), 4217-4222.

Momparler, R. L., Karon, M., Siegel, S. E., & Avila, F. (1976). Effect of adriamycin on DNA, RNA, and protein synthesis in cell-free systems and intact cells. Cancer Res, 36(8), 2891-2895.

Morozan, A., & Jaouen, F. (2012). Metal organic frameworks for electrochemical

applications. Energy & environmental science, 5(11), 9269-9290.

Mosmann, T. (1983). Rapid colorimetric assay for cellular growth and survival: application to proliferation and cytotoxicity assays. Journal of immunological methods, 65(1-2), 55-63.

Mueller, U., Schubert, M., Teich, F., Puetter, H., Schierle-Arndt, K., & Pastre, J. (2006). Metal–organic frameworks—prospective industrial applications. Journal of Materials Chemistry, 16(7), 626-636.

Osguthorpe, D. J., & Hagler, A. T. (2011). Mechanism of androgen receptor antagonism by bicalutamide in the treatment of prostate cancer. Biochemistry, 50(19), 4105-4113. doi:10.1021/bi102059z

Palazzo, A., Iacovelli, R., & Cortesi, E. (2010). Past, present and future of targeted therapy in solid tumors. Current cancer drug targets, 10(5), 433-461.

Paliwal, S. R., Paliwal, R., & Vyas, S. P. (2015). A review of mechanistic insight and application of pH-sensitive liposomes in drug delivery. Drug delivery, 22(3), 231-242.

Pan, Y., Liu, Y., Zeng, G., Zhao, L., & Lai, Z. (2011). Rapid synthesis of zeolitic imidazolate framework-8 (ZIF-8) nanocrystals in an aqueous system. Chemical Communications, 47(7), 2071-2073.

Pang, R., & Poon, R. T. (2006). Angiogenesis and antiangiogenic therapy in hepatocellular carcinoma. Cancer letters, 242(2), 151-167.

Pang, X., Wang, Y., & Chen, Y. (2017). Design, synthesis, and biological evaluation of deuterated apalutamide with improved pharmacokinetic profiles. Bioorganic & medicinal chemistry letters, 27(12), 2803-2806.

Park, K. S., Ni, Z., Côté, A. P., Choi, J. Y., Huang, R., Uribe-Romo, F. J., . . . Yaghi, O. M. (2006). Exceptional chemical and thermal stability of zeolitic imidazolate frameworks. Proceedings of the National Academy of Sciences of the United States of America, 103(27), 10186-10191. doi:10.1073/pnas.0602439103

Park, K. S., Ni, Z., Côté, A. P., Choi, J. Y., Huang, R., Uribe-Romo, F. J., . . . Yaghi, O. M. (2006). Exceptional chemical and thermal stability of zeolitic imidazolate frameworks. Proceedings of the National Academy of Sciences, 103(27), 10186-10191.

Parveen, S., Misra, R., & Sahoo, S. K. (2012). Nanoparticles: a boon to drug delivery, therapeutics, diagnostics and imaging. Nanomedicine: Nanotechnology, Biology and Medicine, 8(2), 147-166.

Pasut, G., & Veronese, F. (2007). Polymer–drug conjugation, recent achievements and

general strategies. Progress in polymer science, 32(8-9), 933-961.

Patra, H. K., & Dasgupta, A. K. (2012). Cancer cell response to nanoparticles: criticality and optimality. Nanomedicine: Nanotechnology, Biology and Medicine, 8(6), 842-852.

Pavlova, N. N., & Thompson, C. B. (2016). The Emerging Hallmarks of Cancer Metabolism. Cell metabolism, 23(1), 27-47. doi:10.1016/j.cmet.2015.12.006

Pellosi, D. S., Moret, F., Fraix, A., Marino, N., Maiolino, S., Gaio, E., . . . Quaglia, F. (2016). Pluronic® P123/F127 mixed micelles delivering sorafenib and its combination with verteporfin in cancer cells. International journal of nanomedicine, 11, 4479.

Pergal, M. V., Antic, V. V., Tovilovic, G., Nestorov, J., Vasiljevic-Radovic, D., & Djonlagic, J. (2012). In vitro biocompatibility evaluation of novel urethane–siloxane co-polymers based on poly (ϵ-caprolactone)-block-poly (dimethylsiloxane)-block-poly (ϵ-caprolactone). Journal of Biomaterials Science, Polymer Edition, 23(13), 1629-1657.

Peskin, A. V., & Winterbourn, C. C. (2000). A microtiter plate assay for superoxide dismutase using a water-soluble tetrazolium salt (WST-1). Clinica Chimica Acta, 293(1-2), 157-166.

Petit, K., & Biard, J.-F. (2013). Marine natural products and related compounds as anticancer agents: an overview of their clinical status. Anti-Cancer Agents in Medicinal Chemistry (Formerly Current Medicinal Chemistry-Anti-Cancer Agents), 13(4), 603-631.

Phillips, K. A., Jenkins, M. A., Lindeman, G. J., McLachlan, S. A., McKinley, J. M., Weideman, P. C., . . . Investigators, k. (2006). Risk-reducing surgery, screening and chemoprevention practices of BRCA1 and BRCA2 mutation carriers: a prospective cohort study. Clinical genetics, 70(3), 198-206.

Poon, R. T., Fan, S. T., Lo, C. M., Liu, C. L., & Wong, J. (2002). Long-term survival and pattern of recurrence after resection of small hepatocellular carcinoma in patients with preserved liver function: implications for a strategy of salvage transplantation. Ann Surg, 235(3), 373-382. doi:10.1097/00000658-200203000-00009

Prasad, A. S., Mukhtar, H., Beck, F. W., Adhami, V. M., Siddiqui, I. A., Din, M., . . . Kucuk, O. (2010). Dietary zinc and prostate cancer in the TRAMP mouse model. Journal of medicinal food, 13(1), 70-76.

Qu, R., Zhang, W., Liu, N., Zhang, Q., Liu, Y., Li, X., . . . Feng, L. (2018). Antioil Ag3PO4 nanoparticle/polydopamine/Al2O3 sandwich structure for complex wastewater treatment: dynamic catalysis under natural light. ACS Sustainable Chemistry & Engineering, 6(6), 8019-8028.

Rathkopf, D. E., Smith, M., Ryan, C., Berry, W., Shore, N., Liu, G., . . . Tutrone, R. (2017). Androgen receptor mutations in patients with castration-resistant prostate cancer treated with apalutamide. Annals of Oncology, 28(9), 2264-2271.

Ren, H., Zhang, L., An, J., Wang, T., Li, L., Si, X., . . . Su, Z. (2014). Polyacrylic acid@zeolitic imidazolate framework-8 nanoparticles with ultrahigh drug loading capability for pH-sensitive drug release. Chemical Communications, 50(8), 1000-1002. doi:10.1039/C3CC47666A

Ren, K., Wang, Y.-P., & Liu, S. (2021). The role of solute polarity on methanol–silica interfacial solvation: a molecular dynamics study. Physical Chemistry Chemical Physics, 23(2), 1092-1102. doi:10.1039/D0CP04422A

Rice, M. A., Malhotra, S. V., & Stoyanova, T. (2019). Second-Generation Antiandrogens: From Discovery to Standard of Care in Castration Resistant Prostate Cancer. Frontiers in oncology, 9, 801-801. doi:10.3389/fonc.2019.00801

Rivankar, S. (2014). An overview of doxorubicin formulations in cancer therapy. Journal of cancer research and therapeutics, 10(4), 853.

Rojas, S., Devic, T., & Horcajada, P. (2017). Metal organic frameworks based on bioactive components. Journal of Materials Chemistry B, 5(14), 2560-2573.

Roy, A., & Li, S. D. (2016). Modifying the tumor microenvironment using nanoparticle therapeutics. Wiley Interdisciplinary Reviews: Nanomedicine and Nanobiotechnology, 8(6), 891-908.

Ryder, M. R., & Tan, J.-C. (2014). Nanoporous metal organic framework materials for smart applications. Materials Science and Technology, 30(13), 1598-1612.

Sagnelli, E., Macera, M., Russo, A., Coppola, N., & Sagnelli, C. (2020). Epidemiological and etiological variations in hepatocellular carcinoma. Infection, 48(1), 7-17.

Santo, L., Hideshima, T., Kung, A. L., Tseng, J.-C., Tamang, D., Yang, M., . . . Ogier, W. C. (2012). Preclinical activity, pharmacodynamic, and pharmacokinetic properties of a selective HDAC6 inhibitor, ACY-1215, in combination with bortezomib in multiple myeloma. Blood, The Journal of the American Society of Hematology, 119(11), 2579-2589.

Sapavatu, S. N., Chinthala, R., & Jadi, R. K. (2020). An overview on Pharmacokinetics of Polymeric Nanoparticles Intended for Oral Delivery. Journal of Young Pharmacists, 12(3), Journal of Young Pharmacists.

Sarkisov, L., Martin, R. L., Haranczyk, M., & Smit, B. (2014). On the flexibility of metal–organic frameworks. Journal of the American Chemical Society, 136(6), 2228-2231.

Scardino, P. (1989). Early detection of prostate cancer. The Urologic Clinics of North

America, 16(4), 635-655.

Schejn, A., Balan, L., Falk, V., Aranda, L., Medjahdi, G., & Schneider, R. (2014a). Controlling ZIF-8 nano- and microcrystal formation and reactivity through zinc salt variations (Vol. 16).

Schejn, A., Balan, L., Falk, V., Aranda, L., Medjahdi, G., & Schneider, R. (2014b). Controlling ZIF-8 nano- and microcrystal formation and reactivity through zinc salt variations. CrystEngComm, 16(21), 4493-4500. doi:10.1039/C3CE42485E

Schejn, A., Balan, L., Falk, V., Aranda, L., Medjahdi, G., & Schneider, R. (2014c). Controlling ZIF-8 nano-and microcrystal formation and reactivity through zinc salt variations. CrystEngComm, 16(21), 4493-4500.

Schejn, A. M. (2015). Synthesis and catalytic activity of ZIF-8 and doped-ZIF-8 crystals: stability and cytotoxicity evaluation. Université de Lorraine,

Schröder, F. H. (2008). Progress in understanding androgen-independent prostate cancer (AIPC): a review of potential endocrine-mediated mechanisms. European urology, 53(6), 1129-1137.

Senapati, S., Mahanta, A. K., Kumar, S., & Maiti, P. (2018). Controlled drug delivery vehicles for cancer treatment and their performance. Signal Transduction and Targeted Therapy, 3(1), 7. doi:10.1038/s41392-017-0004-3

Serre, C., Millange, F., Thouvenot, C., Nogues, M., Marsolier, G., Louër, D., & Férey, G. (2002). Very Large Breathing Effect in the First Nanoporous Chromium (III)-Based Solids: MIL-53 or CrIII (OH)⊙{O2C− C6H4− CO2}⊙{HO2C− C6H4− CO2H} x⊙ H2O y. Journal of the American Chemical Society, 124(45), 13519-13526.

Shafi, A. A., Yen, A. E., & Weigel, N. L. (2013). Androgen receptors in hormone-dependent and castration-resistant prostate cancer. Pharmacology & therapeutics, 140(3), 223-238.

Shen, H., Liu, J., Lei, J., & Ju, H. (2018). A core–shell nanoparticle–peptide@ metal–organic framework as pH and enzyme dual-recognition switch for stepwise-responsive imaging in living cells. Chemical Communications, 54(66), 9155-9158.

Shiina, H., Igawa, M., & Ishibe, T. (1996). Clinical study on estramustine binding protein (EMBP) in human prostate. The Prostate, 29(3), 169-176.

Shreya, A., Raut, S. Y., Managuli, R. S., Udupa, N., & Mutalik, S. (2019). Active targeting of drugs and bioactive molecules via oral administration by ligand-conjugated lipidic nanocarriers: recent advances. AAPS PharmSciTech, 20(1), 1-12.

Siegel, R. L., Miller, K. D., & Jemal, A. (2017). Cancer statistics, 2017. CA: a cancer

journal for clinicians, 67(1), 7-30.

Singh, R., & Lillard Jr, J. W. (2009). Nanoparticle-based targeted drug delivery. Experimental and molecular pathology, 86(3), 215-223.

Smale, S. T. (2010). Luciferase assay. Cold Spring Harb Protoc, 2010(5), pdb.prot5421. doi:10.1101/pdb.prot5421

Song, W., & Khera, M. (2014). Physiological normal levels of androgen inhibit proliferation of prostate cancer cells in vitro. Asian J Androl, 16(6), 864-868. doi:10.4103/1008-682x.129132

Sounni, N. E., & Noel, A. (2013). Targeting the tumor microenvironment for cancer therapy. Clinical chemistry, 59(1), 85-93.

Sowa, Y., & Sakai, T. (2015). Development of novel epigenetic molecular-targeting agents. Nihon rinsho. Japanese journal of clinical medicine, 73(8), 1263-1267.

Starkov, A. A. (2010). Measurement of mitochondrial ROS production. In Protein Misfolding and Cellular Stress in Disease and Aging (pp. 245-255): Springer.

Su, Y., Cockerill, I., Wang, Y., Qin, Y.-X., Chang, L., Zheng, Y., & Zhu, D. (2019). Zinc-based biomaterials for regeneration and therapy. Trends in biotechnology, 37(4), 428-441.

Sun, C.-Y., Qin, C., Wang, X.-L., Yang, G.-S., Shao, K.-Z., Lan, Y.-Q., . . . Wang, E.-B. (2012). Zeolitic imidazolate framework-8 as efficient pH-sensitive drug delivery vehicle. Dalton transactions, 41(23), 6906-6909.

Sun, S., Sprenger, C. C., Vessella, R. L., Haugk, K., Soriano, K., Mostaghel, E. A., . . . Sun, H. (2010). Castration resistance in human prostate cancer is conferred by a frequently occurring androgen receptor splice variant. The Journal of clinical investigation, 120(8), 2715-2730.

Swain, S., Sahu, P. K., Beg, S., & Babu, S. M. (2016). Nanoparticles for Cancer Targeting: Current and Future Directions. Curr Drug Deliv, 13(8), 1290-1302. doi:10.2174/1567201813666160713121122

Swarbrick, J. (2013). Encyclopedia of Pharmaceutical Technology: Volume 6: CRC Press.

Syed, A., & Chan, W. C. (2015). How nanoparticles interact with cancer cells. Cancer Treat Res, 166, 227-244. doi:10.1007/978-3-319-16555-4_10

Ta, D. N., Nguyen, H. K., Trinh, B. X., Le, Q. T., Ta, H. N., & Nguyen, H. T. (2018). Preparation of nano-ZIF-8 in methanol with high yield. The Canadian Journal of

Chemical Engineering, 96(7), 1518-1531.

Tai, S., Sun, Y., Squires, J. M., Zhang, H., Oh, W. K., Liang, C. Z., & Huang, J. (2011). PC3 is a cell line characteristic of prostatic small cell carcinoma. Prostate, 71(15), 1668-1679. doi:10.1002/pros.21383

Tamames-Tabar, C., García-Márquez, A., Blanco-Prieto, M., Serre, C., & Horcajada, P. (2014). MOFs in pharmaceutical technology. Bio-and Bioinspired Nanomaterials, 83-112.

Tan, L.-L., Li, H., Qiu, Y.-C., Chen, D.-X., Wang, X., Pan, R.-Y., . . . Yang, Y.-W. (2015). Stimuli-responsive metal–organic frameworks gated by pillar [5] arene supramolecular switches. Chemical Science, 6(3), 1640-1644.

Tan, M. H. E., Li, J., Xu, H. E., Melcher, K., & Yong, E.-l. (2015). Androgen receptor: structure, role in prostate cancer and drug discovery. Acta Pharmacologica Sinica, 36(1), 3-23. doi:10.1038/aps.2014.18

Tanaka, S., Kida, K., Nagaoka, T., Ota, T., & Miyake, Y. (2013). Mechanochemical dry conversion of zinc oxide to zeolitic imidazolate framework. Chemical Communications, 49(72), 7884-7886.

Tang, J., Sui, C.-J., Wang, D.-F., Lu, X.-Y., Luo, G.-J., Zhao, Q., . . . Zhu, Y.-J. (2020). Targeted sequencing reveals the mutational landscape responsible for sorafenib therapy in advanced hepatocellular carcinoma. Theranostics, 10(12), 5384.

Taylor-Pashow, K. M., Della Rocca, J., Xie, Z., Tran, S., & Lin, W. (2009). Postsynthetic modifications of iron-carboxylate nanoscale metal− organic frameworks for imaging and drug delivery. Journal of the American Chemical Society, 131(40), 14261-14263.

Thakkar, S., Sharma, D., Kalia, K., & Tekade, R. K. (2020). Tumor microenvironment targeted nanotherapeutics for cancer therapy and diagnosis: A review. Acta biomaterialia, 101, 43-68.

Thanki, K., Gangwal, R. P., Sangamwar, A. T., & Jain, S. (2013). Oral delivery of anticancer drugs: challenges and opportunities. Journal of controlled release, 170(1), 15-40.

Thorn, T., Gniadecki, R., Petersen, A. B., Vicanova, J., & Wulf, H. C. (2001). Differences in activation of G2/M checkpoint in keratinocytes after genotoxic stress induced by hydrogen peroxide and ultraviolet A radiation. Free radical research, 35(4), 405-416.

To, P. K., Cho, Y.-S., Kwon, S.-Y., Kang, T. W., Kim, K. K., & Jung, C. (2017). Zinc inhibits androgen receptor expression to inhibit prostate cancer cell growth. In: AACR.

To, P. K., Do, M. H., Cho, J. H., & Jung, C. (2020). Growth Modulatory Role of Zinc in Prostate Cancer and Application to Cancer Therapeutics. International journal of molecular sciences, 21(8). doi:10.3390/ijms21082991

Tranchemontagne, D. J., Hunt, J. R., & Yaghi, O. M. (2008). Room temperature synthesis of metal-organic frameworks: MOF-5, MOF-74, MOF-177, MOF-199, and IRMOF-0. Tetrahedron, 64(36), 8553-8557.

Troyano, J., Carné-Sánchez, A., Avci, C., Imaz, I., & Maspoch, D. (2019). Colloidal metal–organic framework particles: the pioneering case of ZIF-8. Chemical Society Reviews, 48(23), 5534-5546.

Tüylek, Z. (2017). İLAÇ TAŞIYICI SİSTEMLER VE NANOTEKNOLOJİK ETKİLEŞİM Drug Delivery Systems and Nanotechnological Interaction. Bozok Tıp Dergisi, 7(3), 89-98.

Uzzo, R. G., Leavis, P., Hatch, W., Gabai, V. L., Dulin, N., Zvartau, N., & Kolenko, V. M. Zinc Inhibits Nuclear Factor-B Activation and Sensitizes Prostate Cancer Cells to Cytotoxic Agents.

Vagin, S., Ott, A. K., & Rieger, B. (2007). Paddle-Wheel Zinc Carboxylate Clusters as Building Units for Metal-Organic Frameworks. Chemie Ingenieur Technik, 79(6), 767-780.

Valter, K., Chen, L., Kruspig, B., Maximchik, P., Cui, H., Zhivotovsky, B., & Gogvadze, V. (2017). Contrasting effects of glutamine deprivation on apoptosis induced by conventionally used anticancer drugs. Biochimica et Biophysica Acta (BBA)-Molecular Cell Research, 1864(3), 498-506.

Vasconcelos, I. B., Silva, T. G. d., Militão, G. C. G., Soares, T. A., Rodrigues, N. M., Rodrigues, M. O., . . . Junior, S. A. (2012). Cytotoxicity and slow release of the anti-cancer drug doxorubicin from ZIF-8. RSC Advances, 2(25), 9437-9442. doi:10.1039/C2RA21087H

Vasir, J. K., & Labhasetwar, V. (2005). Targeted drug delivery in cancer therapy. Technology in cancer research & treatment, 4(4), 363-374.

Vasir, J. K., Reddy, M. K., & Labhasetwar, V. D. (2005). Nanosystems in drug targeting: opportunities and challenges. Current Nanoscience, 1(1), 47-64.

Velma, V., Dasari, S. R., & Tchounwou, P. B. (2016). Low doses of cisplatin induce gene alterations, cell cycle arrest, and apoptosis in human promyelocytic leukemia cells. Biomarker insights, 11, BMI. S39445.

Verslype, C., Van Cutsem, E., Dicato, M., Arber, N., Berlin, J. D., Cunningham, D., . . . van de Velde, C. (2009). The management of hepatocellular carcinoma. Current expert opinion and recommendations derived from the 10th World Congress on

Gastrointestinal Cancer, Barcelona, 2008. Ann Oncol, 20 Suppl 7, vii1-vii6. doi:10.1093/annonc/mdp281

Wallis, C. J., Chandrasekar, T., Goldberg, H., Klotz, L., Fleshner, N., Satkunasivam, R., & Klaassen, Z. (2018). Advanced Androgen Blockage in Nonmetastatic Castration-resistant Prostate Cancer: An Indirect Comparison of Apalutamide and Enzalutamide. European Urology Oncology.

Wang, H.-T., & Xia, M. (2019). A meta-analysis of efficacy and safety of sorafenib versus other targeted agents for metastatic renal cell carcinoma. Medicine, 98(1).

Wang, Q., Sun, Y., Li, S., Zhang, P., & Yao, Q. (2020). Synthesis and modification of ZIF-8 and its application in drug delivery and tumor therapy. RSC Advances, 10(62), 37600-37620.

Wang, Q., Zhang, P., Li, Z., Feng, X., Lv, C., Zhang, H., . . . Chen, X. (2019). Evaluation of polymer nanoformulations in hepatoma therapy by established rodent models. Theranostics, 9(5), 1426.

Wickham, T. J. (2003). Ligand-directed targeting of genes to the site of disease. Nature medicine, 9(1), 135-139.

Wu, M. X., & Yang, Y. W. (2017). Metal–organic framework (MOF)-based drug/cargo delivery and cancer therapy. Advanced Materials, 29(23), 1606134.

Wu, Q., Niu, M., Chen, X., Tan, L., Fu, C., Ren, X., . . . Zhong, H. (2018). Biocompatible and biodegradable zeolitic imidazolate framework/polydopamine nanocarriers for dual stimulus triggered tumor thermo-chemotherapy. Biomaterials, 162, 132-143.

Xiao, Y., Liu, Y., Yang, S., Zhang, B., Wang, T., Jiang, D., . . . Zhang, N. (2016). Sorafenib and gadolinium co-loaded liposomes for drug delivery and MRI-guided HCC treatment. Colloids and Surfaces B: Biointerfaces, 141, 83-92. doi:https://doi.org/10.1016/j.colsurfb.2016.01.016

Xu, X., Zhang, S., Tang, J., Pan, L., Eguchi, M., Na, J., & Yamauchi, Y. (2020). Nitrogen-Doped Nanostructured Carbons: A New Material Horizon for Water Desalination by Capacitive Deionization. EnergyChem, 100043.

Yallapu, M. M., Chauhan, N., Othman, S. F., Khalilzad-Sharghi, V., Ebeling, M. C., Khan, S., . . . Chauhan, S. C. (2015). Implications of protein corona on physico-chemical and biological properties of magnetic nanoparticles. Biomaterials, 46, 1-12.

Yamamoto, D., Maki, T., Watanabe, S., Tanaka, H., Miyahara, M. T., & Mae, K. (2013). Synthesis and adsorption properties of ZIF-8 nanoparticles using a micromixer. Chemical Engineering Journal, 227, 145-150.

Yang, G., Xu, L., Xu, J., Zhang, R., Song, G., Chao, Y., . . . Li, B. (2018). Smart Nanoreactors for pH-Responsive Tumor Homing, Mitochondria-Targeting, and Enhanced Photodynamic-Immunotherapy of Cancer. Nano letters, 18(4), 2475-2484.

Yang, J.-C., Shang, Y., Li, Y.-H., Cui, Y., & Yin, X.-B. (2018). An "all-in-one" antitumor and anti-recurrence/metastasis nanomedicine with multi-drug co-loading and burst drug release for multi-modality therapy. Chemical Science, 9(36), 7210-7217.

Yang, J., Zhang, Y.-B., Liu, Q., Trickett, C. A., Gutiérrez-Puebla, E., Monge, M. A. n., . . . Yaghi, O. M. (2017). Principles of designing extra-large pore openings and cages in zeolitic imidazolate frameworks. Journal of the American Chemical Society, 139(18), 6448-6455.

Yao, J., He, M., & Wang, H. (2015). Strategies for controlling crystal structure and reducing usage of organic ligand and solvents in the synthesis of zeolitic imidazolate frameworks. CrystEngComm, 17(27), 4970-4976.

Zaichick, V. Y., Sviridova, T., & Zaichick, S. (1997). Zinc in the human prostate gland: normal, hyperplastic and cancerous. International urology and nephrology, 29(5), 565-574.

Zhang, C., Wang, X., Hou, M., Li, X., Wu, X., & Ge, J. (2017). Immobilization on Metal–Organic Framework Engenders High Sensitivity for Enzymatic Electrochemical Detection. ACS Applied Materials & Interfaces, 9(16), 13831-13836. doi:10.1021/acsami.7b02803

Zhang, L., Gu, F., Chan, J., Wang, A., Langer, R., & Farokhzad, O. (2008). Nanoparticles in medicine: therapeutic applications and developments. Clinical pharmacology & therapeutics, 83(5), 761-769.

Zhang, S., Gao, W., Tang, J., Zhang, H., Zhou, Y., Liu, J., . . . To, S. K. (2020). The roles of GSK-3β in regulation of retinoid signaling and sorafenib treatment response in hepatocellular carcinoma. Theranostics, 10(3), 1230.

Zhang, Z., Niu, B., Chen, J., He, X., Bao, X., Zhu, J., . . . Li, Y. (2014). The use of lipid-coated nanodiamond to improve bioavailability and efficacy of sorafenib in resisting metastasis of gastric cancer. Biomaterials, 35(15), 4565-4572.

Zhao, R., Li, T., Zheng, G., Jiang, K., Fan, L., & Shao, J. (2017). Simultaneous inhibition of growth and metastasis of hepatocellular carcinoma by co-delivery of ursolic acid and sorafenib using lactobionic acid modified and pH-sensitive chitosan-conjugated mesoporous silica nanocomplex. Biomaterials, 143, 1-16.

Zhao, Y., Song, Z., Li, X., Sun, Q., Cheng, N., Lawes, S., & Sun, X. (2016). Metal organic frameworks for energy storage and conversion. Energy Storage Materials, 2, 35-62.

Zhao, Z.-B., Long, J., Zhao, Y.-Y., Yang, J.-B., Jiang, W., Liu, Q.-Z., . . . Lian, Z.-X. (2018). Adaptive immune cells are necessary for the enhanced therapeutic effect of sorafenib-loaded nanoparticles. Biomaterials science, 6(4), 893-900.

Zheng, C., Wang, Y., Phua, S. Z. F., Lim, W. Q., & Zhao, Y. (2017). ZnO–DOX@ ZIF-8 Core–Shell Nanoparticles for pH-Responsive Drug Delivery. ACS Biomaterials Science & Engineering, 3(10), 2223-2229.

Zheng, H., Zhang, Y., Liu, L., Wan, W., Guo, P., Nyström, A. M., & Zou, X. (2016). One-pot Synthesis of Metal–Organic Frameworks with Encapsulated Target Molecules and Their Applications for Controlled Drug Delivery. Journal of the American Chemical Society, 138(3), 962-968. doi:10.1021/jacs.5b11720

Zheng, H., Zhang, Y., Liu, L., Wan, W., Guo, P., Nyström, A. M., & Zou, X. (2016). One-pot synthesis of metal–organic frameworks with encapsulated target molecules and their applications for controlled drug delivery. Journal of the American Chemical Society, 138(3), 962-968.

Zheng, M., Liu, S., Guan, X., & Xie, Z. (2015). One-step synthesis of nanoscale zeolitic imidazolate frameworks with high curcumin loading for treatment of cervical cancer. ACS Applied Materials & Interfaces, 7(40), 22181-22187.

Zhou, H.-C. J., & Kitagawa, S. (2014). Metal–Organic Frameworks (MOFs). Chemical Society Reviews, 43(16), 5415-5418. doi:10.1039/C4CS90059F

Zhou, J., Tian, G., Zeng, L., Song, X., & Bian, X.-w. (2018). Nanoscaled Metal-Organic Frameworks for Biosensing, Imaging, and Cancer Therapy. Advanced Healthcare Materials, 7(10), 1800022. doi:https://doi.org/10.1002/adhm.201800022

Zhu, Y.-j., Zheng, B., Wang, H.-y., & Chen, L. (2017). New knowledge of the mechanisms of sorafenib resistance in liver cancer. Acta Pharmacologica Sinica, 38(5), 614-622.

Zhuang, J., Kuo, C.-H., Chou, L.-Y., Liu, D.-Y., Weerapana, E., & Tsung, C.-K. (2014). Optimized metal–organic-framework nanospheres for drug delivery: evaluation of small-molecule encapsulation. ACS nano, 8(3), 2812-2819.

Vita

Derya METE

QUALIFICATION

- **PhD** (CGPA; 3.36 / 4.0)
  Izmir Institute of Technology – Izmir, Turkey

PhD in Chemistry 2014-2021

- **Master Program in Chemistry** (CGPA; 3.21/4)

Izmir Institute of Technology – Izmir, Turkey 2010-2013

- **Bachelor's Degree in Chemistry Education** (CGPA; 2.95/4)

Dokuz Eylül University – Izmir, Turkey 2005-2010

- **High School**

Nevvar Salih İŞGÖREN High School– Izmir, Turkey 2001-2005

WORK EXPERIENCE

- **Research Assistant at Izmir Institute of Technology/** 2012-2022

Projects

- Prostat Kanseri Tedavisi için Apalutamid'in Metalo-kapsüllenmesi In vitro, In vivo ve Ex vivo Etkinliklerinin Araştırması, -Tübitak 1001, Yürütücü:ŞANLI MOHAMED GÜLŞAH,Bursiyer:METE DERYA, , 01/04/2019 (Devam Ediyor) (ULUSAL)

- Bisikloaril substitentli(R)-5.6-Dihidro-2H-pyran-2-on türevlerinin anti tümör özelikleri Laboratuardan klinik öncesi çalışmalara, -Tübitak 1001, Yürütücü:ÇAĞIR ALİ,Bursiyer:METE DERYA, , 15/04/2011 - 15/04/2014 (ULUSAL)

Articles

- D. METE, G. GOKTAS & G. SANLİ-MOHAMED Fabrication and in vitro evaluation of thermally cross-linked gelatin nanofibers for drug delivery applications PREPARATIVE BIOCHEMISTRY & BIOTECHNOLOGY (2021)

- Akcok Ismail,METE DERYA,Sen Ayhan,Kasaplar Pinar,Korkmaz Kemal S.,ÇAĞIR ALİ (2017). Synthesis and Topoisomerase I inhibitory properties

of klavuzon derivatives. BIOORGANIC CHEMISTRY, 71(null), 275-284., Doi: 10.1016/j.bioorg.2017.02.012 (Yayın No: 3876845)

- HORZUM POLAT NESRİN,METE DERYA,KARAKUŞ ERMAN,ÜÇÜNCÜ MUHAMMED,EMRULLAHOĞLU MUSTAFA,DEMİR MUSTAFA MUAMMER (2016). Rhodamine immobilised electrospun chitosan nanofibrous material as a fluorescence turn on Hg2 sensor. Chemistry Select

Conference Papers

- ŞANLI MOHAMED GÜLŞAH,METE DERYA,Almusawi Yasir (2018). Investigation of Cytotoxic Effect of Newly Synthesized Isoindole Derivatives. EURASIANSCIENTECH 2018
- METE DERYA,HORZUM POLAT NESRİN,ŞANLI MOHAMED GÜLŞAH (2016). Controlled Release of Doxorubicin from Electrospun Gelatin Nanofibers. Proceedings of the World Congress on Recent Advances in Nanotechnology (RAN'16)

- METE DERYA,HORZUM POLAT NESRİN,KARAKUŞ ERMAN,ÜÇÜNCÜ MUHAMMED,EMRULLAHOĞLU MUSTAFA,DEMİR MUSTAFA MUAMMER (2015). Fabrication and characterization of electrospun chitosan rhodamine B nanofibrous mat as a fluorescence turn on Hg2 sensor. Green Chemistry and Sustainable Technologies

- AKÇOK İSMAİL,ÇAĞIR ALİ,METE DERYA (2014). 6-Bisikloaril Sübstitüeli 5,6-dihidro-2H-piran-2-on'ların Apoptotik Özelliklerinin İncelenmesi. 2. İlaç Kimyası, Üretimi, Teknolojisi ve Standardizasyonu Kongresi

- METE DERYA,ÇAĞIR ALİ (2013). 6 Bisikloaril Sübstitüeli 5 6 dihidro 2H piran 2 on ların Hücre İçi Etki Mekanizmasının İncelenmesi . I. İlaç Kimyası Üretimi, Teknolojisi, Standardizasyonu Kongresi